UNIVERSITY OF CALIFORNIA
SANTA CRUZ

STRUCTURE AND TOPOLOGY IN NANOSCALE MAGNETIC SYSTEMS

A dissertation submitted in partial satisfaction of the
requirements for the degree of

DOCTOR OF PHILOSOPHY

in

PHYSICS

by

Noah A.A. Kent

June 2020

The Dissertation of Noah A.A. Kent
is approved:

Professor Peter Fischer, Chair

Professor David Lederman

Doctor Stefano Cabrini

Quentin Williams
Acting Vice Provost and Dean of Graduate Studies

Structure and Topology in Nanoscale Magnetic Systems

Contents

List of Figures

Abstract

Structure and Topology in Nanoscale Magnetic Systems

Noah A.A. Kent

Understanding the properties and behavior of spin textures in confined nanomagnetic systems is scientifically challenging, but also highly relevant for future technologies. Recently the aspect of topology, in particular the topological protection of novel spin textures, such as magnetic skyrmions, have garnered much interest In this dissertation the relationship of structure and topology to create and control confined magnetic nanostructures through variation of size, composition, and proximity has been investigated experimentally. Requisite nanomagnetic systems were fabricated with state of the art nanofabrication and thin film deposition techniques. They were characterized by a variety of state-of-the-art techniques including various electron and x-ray spectromicroscopies at large scale facilities.

The effect of stray field interactions on the coupling of arrays of nanodisks that exhibit a vortex state spin configuration, as well as so-called XY macrospins revealed the stabilization of collective states with characteristic topologies, that differ from the properties of the individual nanodisks. The insight obtained from that study was used to investigate the transition from paramagnetic magnetic nanoparticle assemblies into a ferromagnetic liquid droplet when jammed through chemical ligands at a liquid-liquid interface.

The vertical coupling in thin film multilayer stacks introduces new ways to control nanoscale spin textures, and led to the stabilization of magnetic skyrmions by varying the thickness and the composition of the multilayers. These studies led to an understanding of the energetic conditions required to stabilize dipolar skyrmion lattices, and subsequenltly, chiral ferrimagnetism .

Interfacing thin film multilayers with strong PMA with confined vortex textures in nanodisks allowed for an imprinting and modification of the spin textures in the combined system. In particular, this study resolved extended topological spin textures, so called nπ target skyrmions, which theoretical predictions identified as precursor for 3D topological spin textures, specifically magnetic Hopfions.

The characteristic spin textures of Hopfions, which are 3D knot-solitons was verified through a combined surface and bulk sensitive x-ray microscopy study. Investigating the sub-ns dynamics of Hopfions with time-resolved x-ray microscopy studies will open the door to exploit their potential for future application e.g. in spintronic devices.

Acknowledgments

I consider myself very lucky to have had a PhD experience that I enjoyed. There were times that were very difficult (beamtimes, writing this thesis), but I was very happy the vast majority of the time being where I was and performing the science I was pursuing. I attribute this to those around me who supported me scientifically and emotionally.

Scientifically, I get to thank my advisor Peter Fischer. He taught me how to access to the best scientific facilities in the world, encouraged my scientific exploration, and, most importantly, told me when I was wrong. I would like to thank all the members of the Fischer Group and by extension the members of NEMM.

My papers and research would also not have been possible or enjoyable without my collaborators, and I would like to thank all of them. In particular, those who discussed ideas with me and answered my, sometimes endless, lists of questions: Paul, Felix, Xubo, Tom, Charles-Henri, Neal, and Alex.

I received a tremendous amount of help from those at Lawrence Berkeley National Lab. In particular I would also like to thank the entire staff at the ALS, CXRO, and the MF. I would like to thank the MF second floor staff for being so helpful and being accommodating to me and my various mistakes. I would also like to thank the staff at ALBA and the MISTRAL beamline.

I would like to thank Zhiyu, my Grace. I would like to thank my mom and my sisters for supporting me emotionally my entire life. I would like to thank my friends, for distracting me from science.

Everyone mentioned here has brought me great joy (and scientific insight), which I hope to share with others in the future via physics, whatever that may mean.

"Sometimes science is more art than science."

-R. Sanchez

Chapter 1

Introduction

This dissertation addresses the question whether novel magnetic properties and behavior can be generated by exploiting the physics of structural and topological nanomagnetism. To that end, three different types of magnetic systems are studied experimentally through careful design and state-of-the-art characterization techniques: arrays of magnetic nanostructures with lateral dimensions on the order of tens of nanometers interacting through stray fields, vertically stacked magnetic multilayers where interfacial effects dominate, and combinations of laterally confined nanostructures with thin film magnetic multilayers, where topological spin textures are stabilized.

In this chapter a brief overview is provided of the importance of magnetism in science and technology throughout history until today, followed by an introduction into contemporary structural and topological magnetism. The chapter concludes with the problem statement of this dissertation, why a combination of structure and topology in nanoscale magnetic system is worth being investigated, and outlines briefly the experimental challenges in this dissertation and how they were approached.

1.1 Magnetism in Science and Technology

Magnetism is one of the oldest physical phenomena that has attracted the fascination of humans and has been used for technological applications. The first several thousand years of magnetic observation was purely phenomenological. Around 2000 B.C.E, the first magnets

were used in ancient China to navigate the featureless grasslands of the Asiatic Plains [1]. Thales of Miletus is attributed with being the first westerner to write about magnetism, around 600 B.C.E, identifying lodestones, chunks of magnetite, as magnets [2]. He is also credited with being the first scientist; he sought explanations for natural phenomena that did not rely on gods, proposed hypotheses, and was the first person to whom a mathematical discovery can be attributed to.

The first magnet used as a compass outside of China was described in 1190 by Alexander Neckam, who understood that the needle in a magnet could be magnetized by an external lodestone to be used for navigation and that this effect would decrease over time [3]. This is a basic phenomenological understanding of magnetic hysteresis and thermal degradation of a magnetic state.

The French crusader and scholar, Pierre Pelerin de Maricourt in 1269 was the first person to assign the word 'pole' to describe a magnet and was the first person to determine that all magnets were dipoles; all magnets always have a North and South pole with like poles being repulsive and opposite poles being attractive to each other [4]. After the dark ages, in 1600, William Gilbert expounded Pelerin's work in *De Magnete* and showed, via a scale model of a magnetized sphere and multiple experiments, that the reason compasses work to navigate the globe is that the earth itself is a magnet [5].

Whereas the fundamental phenomenological macroscopic properties of static ferromagnetic materials, i.e., magnetic dipoles as fundamental building blocks and a hysteretic behavior as response to external magnetic fields have already been observed at that time, it is surprising that today a fundamental understanding of magnetism is still lacking.

1.1.1 Classical Magnetism

After the basic qualitative properties of magnets were explored, scientists started to develop a systematic, scientific understanding of magnets; Maxwell's equations provide a quantitative understanding of all macroscopic, non-relativistic, magnetic behavior. At this point in time, the history of magnetism becomes the history of electromagnetism, since Maxwell's Equations couple electricity and magnetism. Even though James Clerk Maxwell was not responsible for the original derivation of many of these formulae, his 1861 paper, *On Phys-*

ical Lines of Force, is the first time they were all published jointly and elegantly tied together. Maxwell's Equations combine the following four relationships: Gauss Law, Gauss Law for magnetism, Faraday Law, and Ampère's Law, which was modified by Maxwell to the Maxwell-Ampère Law.

In 1785, Charles-Augustin de Coulomb performed an experiment using a torsion balance and two charged balls to determine that the force exerted between two charged bodies is proportional to the charge, and is inversely proportional to the distance between the two bodies [6]. This is now known as Coulomb's Law:

$$F = k\frac{Q_1 Q_2}{r^2} \tag{1.1}$$

where k is Coulomb's constant, $8.988 \cdot 10^9 \mathrm{Nm}^2\mathrm{C}^{-2}$, Q_1 and Q_2 are the charge on each body, and r is the distance between them. Maxwell's first equation, Gauss's Law, can be derived from Coulomb's Law, given the superposition principle and integrating over an arbitrary charge distribution (in SI units):

$$\nabla \cdot \mathbf{E} = \frac{\rho}{\varepsilon_0} \tag{1.2}$$

where $\varepsilon_0 = \frac{1}{4\pi k}$, $\mathbf{E}$ is the electric field generated by that charge density, and ρ is the electric charge density.

Since there are no magnetic charges, the magnetic version of Gauss's Law is

$$\nabla \cdot \mathbf{B} = 0 \tag{1.3}$$

In 1820 Hans Christian Ørsted published results showing a magnetic compass could be deflected by the current in a wire [7]. Inspired by his work, André Ampère immediately began to try and describe this phenomena mathematically, resulting in Ampère's Law, which states that an electric current traveling through a wire [8] will generate a magnetic field which curls around the wire. Maxwell's greatest original contribution to electromagnetism was the inclusion of a "displacement current", influenced by hydrodynamics, to Ampère's law resulting in the Maxwell-Ampère Law we know of today, with $\mathbf{J}$ being the current density [9]:

$$\nabla \times \mathbf{B} = \mu_0(\mathbf{J} + \varepsilon_0\frac{\partial \mathbf{E}}{\partial t}) \tag{1.4}$$

Michael Faraday discovered in 1821 that, by moving a magnet through a coil of wires, a solenoid, he could produce a current. He made detailed experimental records and described this electromagnetic interaction through "lines of force" [10]. Maxwell diligently studied his work and generated a mathematical description of Faraday's observations, the Maxwell-Faraday Equation:

$$\nabla \times \mathbf{E} = -\frac{\partial \mathbf{B}}{\partial \mathrm{t}} \tag{1.5}$$

Maxwell also mathematically described the force on a charged object in an electromagnetic field, $\mathbf{F} = \mathrm{q}\mathbf{v} \times \mathbf{B}$, which, when combined with Coulomb's Law, is the Lorentz force, a peculiar nomenclature considering that when this was published Hendrik Lorentz was only 9 years old.

Maxwell's equations provide the theoretical underpinnings for electric motors and electricity generation from magnets. In 1822, the first device powered by electromagnetism, Barlow's wheel, was invented by Peter Barlow. In 1934, the first functional electromagnetic motor, used to power a boat, was invented by Moritz von Jacobi [11].

Using electromagnetic motors and devices is one of the factors that allowed humans to industrialize. The fact that a rotating magnet generates an electric current in nearby wires, discovered by Faraday, is used to create approximately 91% of electricity [12]. Advancement in the science of magnetism has a history of leading to advancement in technology.

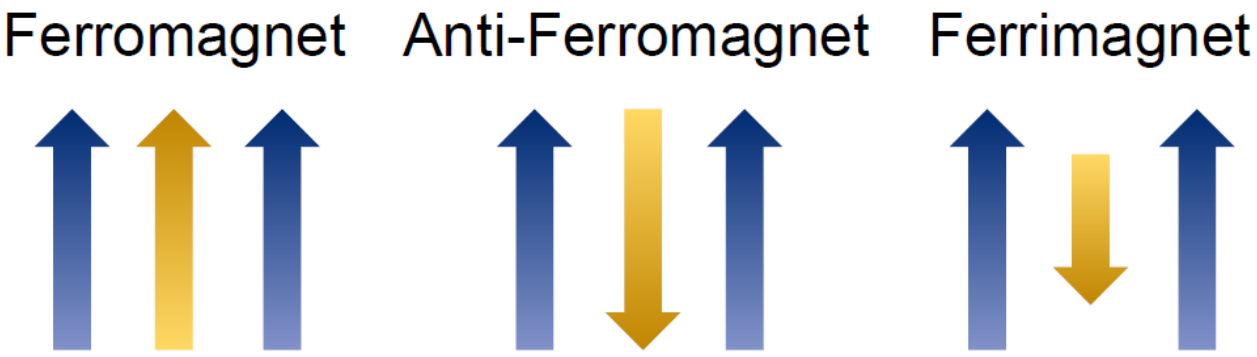

Figure 1.1: The different classes of magnetic materials with the energetically preferred alignment between adjacent spins shown.

1.1.2 Modern Nanomagnetism and Spintronics

Even though the major classes of magnetic materials were not theoretically understood until 1948 [13], a definition of them will aid in this discussion, see Fig.1.1. In a ferromagnetic material, it is energetically favorable for the magnetic moments in that material to align parallel to each other, resulting in a net magnetic moment. Ferromagnetic materials are colloquially denoted as magnets. An antiferromagnetic material is one where adjacent moments prefer an anti-parallel alignment, resulting in no net magnetic moment. A ferrimagnetic material is an antiferromagnet where there is a variation in the magnetic moment of the material, resulting in a small net magnetic moment. A paramagnetic material is one where neighboring magnetic moments in the material do not couple with each other. This results in the material having a net magnetization only in the presence of an external field. A superparamagnet is a material which has a net magnetic moment at every moment in time, but due to thermal fluctuations has no net magnetic moment when averaged over a measurable time period.

At the beginning of the 20th century, the technological application of magnetic materials, (i.e., Fe, Gd, Ni, Co), had already significant and widespread impact, but a fundamental scientific understanding of the origin of magnetism was still completely lacking. The molecular, atomic origins of magnetism were largely ignored until Paul Langevin put forth a theory of paramagnetism in 1905, showing that the paramagnetic response of a material can be explained by independent molecular magnets in an external magnetic field, this is still a very accurate interpretation of how paramagnetic materials actually work [14]. The first attempt to explain ferromagnetism was put forth by Pierre Weiss two years later [15], using a precursor of mean field theory applied to a system of independent magnetic molecules, similar to Langevin's system. Since the magnitude of each molecule's magnetic moments never decrease, but only change direction, Weiss also introduced the concept of magnetic domains: regions of distinct magnetization which, when averaged together give the macroscopic magnetization of the sample. The first domain observation technique, developed by Bitter in 1932, involved taking a fine magnetic powder and dispersing it over the surface of a magnetic material [16]. In Bitter's work on in-plane magnetized films, the powder aggregated on domain walls, the out-of-plane magnetic field was largest over domain walls, and the structure of the in-plane domains was revealed.

Electron Spin

As part of the scientific revolution of quantum mechanics at the beginning of the 20th century, the science of magnetism and magnetic materials received a transformational change. Macroscopic ferromagnetic behavior arises from the alignment of electron's magnetic moments generating a net magnetic moment in a material. An electron's magnetic moment, $\mathbf{m}_e$, is correlated to its intrinsic angular momentum, $\mathbf{S}$, in the following way:

$$\mathbf{m}_e = g\frac{q}{2m}\mathbf{S} \tag{1.6}$$

where q is the elementary charge, m is the mass of an electron, and g is a unit less constant called the g-factor. The g-factor is highly dependent on the fundamental quantum mechanics of the particle, i.e., for an electron g = –2.002, but for a proton g = 5.586. It is therefore enlightening to understand the source of an electron's intrinsic angular momentum: its spin.

Experimentally, a discretization of the angular momentum, and also magnetic moment, of the electron was confirmed in the Stern-Gerlach experiment [17] (Fig.1.2): silver ions were passed through a divergent magnetic field where relative deflection of the ions is proportional to the z component of their magnetic moment. The deflection of the ions was recorded on a phosphorous screen, see Fig.1.2. If electron spin was a classic observable the ion's angular momentum would be uniformly distributed, resulting in an even spread of ions when they hit the target (Fig.1.2(4)). Experimentally, electrons only hit the screen in two regions (Fig.1.2(5)). It was concluded that isolated electrons have two discrete states for their spin when measured: up and down. In the Stern-Gerlach experiment up and down correspond to the energy minima of the magnetic moment of the electrons when in the external field [17].

A derivation of spin from first principles surprisingly occurred when Dirac, in 1928, published a relativistic invariant version of the Schrödinger equation: the Dirac equation (in no external field). The solutions for the Dirac equation reveal a degeneracy in electron states with the same energy and momentum: this is the electron spin, and it couples appropriately with the electromagnetic Lagrangian to behave as spin [19].

With a fundamental understanding of an electron's spin established, it is no coincidence that Heisenberg developed the formalism for exchange interaction in 1928 [20], see theory section for more details. Heisenberg exchange explained macroscopic ferromagnetic behavior

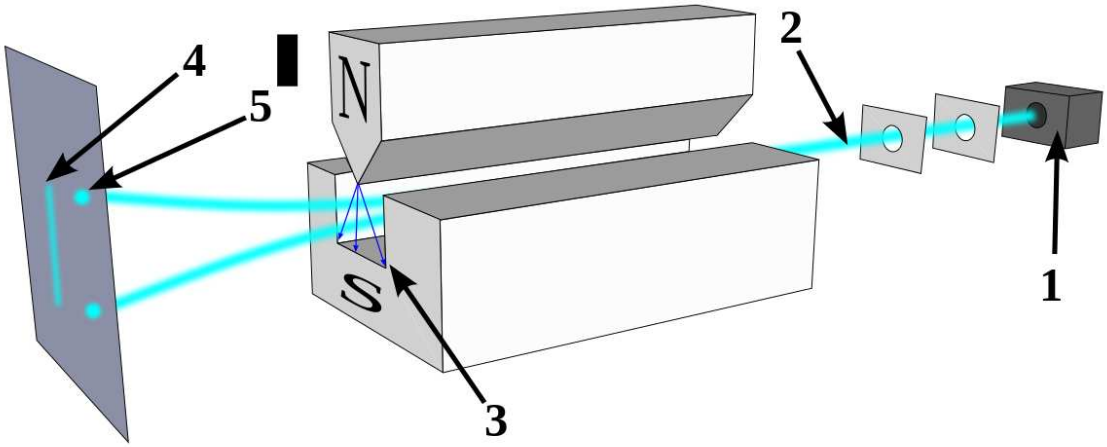

Figure 1.2: Stern–Gerlach experiment: Silver atoms travelling through an inhomogeneous magnetic field, and being deflected up or down depending on their spin; (1) furnace, (2) beam of silver atoms, (3) inhomogeneous magnetic field, (4) classically expected result, (5) observed quantum mechanical result. Reproduced under the creative commons license (https://creativecommons.org/licenses/by/2.0/) from [18].

by having it be energetically favorable for neighboring electron's magnetic moments to align, generating a net magnetic moment, in a macroscopic material. Coupled with the demagnetizing field, which prefers to have a net magnetization of zero, the stabilization of magnetic domains was understood analytically. The addition of structurally induced energies and external fields induces the more complex magnetic phenomena and spin textures detailed in this dissertation.

In the decades since magnetic domains were first theoretically understood, advancements in fabrication and characterization have allowed for creation and manipulation of magnetic structures and phenomena that occur on the nanoscale, which required significant advances

in synthesis, characterization and modeling. Nanofabrication can create structures with lateral dimensions as small as 10nm. X-ray based magnetic microscopy techniques allow for reconstruction of spin textures with resolution on the order of 20-30nm. Lorentz-transmission electron microscopy can reconstruct the magnetic induction field with 2-4nm resolution. This has had significant technological implications resulting in hard drive data storage and spintronics.

1.2 Structural and Topological Nanomagnetism

Structural nanomagnetism is where the structure of a nanomagnetic heterostructure, with critical dimensions on the scale of nanometers, has significant influence on the nature of the magnetic spin texture stabilized. In this dissertation, two types of nanomagnetic heterostructures are fabricated and studied. The first system is magnetic thin film multilayers with thickness of individual multilayers ranging from 1-3nm. The second type of structure are magnetic nanostructures whose shape anisotropy significantly affects the magnetic state, i.e., 30nm thick nanomagnetic disks 1μm diameter FeNi disks in a nanomagnetic vortex state. Additionally both types of structures are combined into systems with multilayers affected by shape anisotropy.

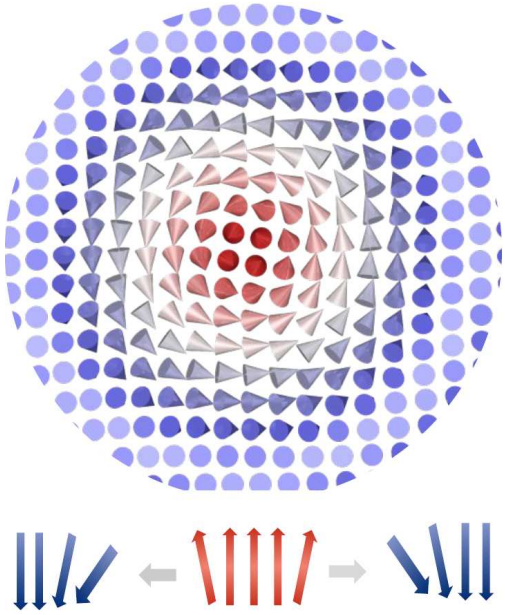

Figure 1.3: Top: vector schematic of a skyrmion. Bottom: spins along the central line of the skyrmion.

Topological magnetism is where the magnetic parameters of a sample lead to topologically nontrivial spin textures. A topologically nontrivial spin texture can not be smoothly permuted into another spin texture with a different topological constant. Most of the time, topological charge conservation physically manifests as the creation of an additional energy barrier, leading to enhanced stability of the topological structure. Magnetic skyrmions are an intensely studied example of topologically protected structures in magnetic systems [21]. Skyrmions (Fig.1.3)

are two dimensional spin textures where there is a smooth, chiral rotation of the magnetization at the center to the anti-parallel magnetization surrounding the skyrmion. They have garnered significant interest due to their size, stability and mobility [21], and have a topological charge that is defined by the winding number, $N_{sk} = 1$.

The combination of structure and topology to nanomagnetic systems is a topic of large current scientific interest. In this dissertation (topologically nontrivial) magnetic structures and phenomena are described in three different heterostructure systems: magnets with shape anisotropy energy generated from nanomagnetic structures with lateral dimensions on the scale of nanometers, magnetic thin film multilayers, and systems that combine thin films with shape anisotropy from nanomagnetic structures.

The shape anisotropy of magnetic structures, with lateral dimensions on the scale of nanometers, has been shown to generate topologically nontrivial spin textures in those structures such as skyrmions [21], target skyrmions [22], magnetic vortices [23], and Bloch point domain walls [24]. Additionally, significant research has gone into nanomagnetic particles, whose magnetic structure and properties are determined by their size and temperature [25].

Interactions between magnetic heterostructures, through the stray field generated by the structures, can lead to fascinating physics. These nanomagnetic structures can interact with each other through their magnetic fields, generating collective topological behavior (such as monopoles and Dirac chains in spin ice [26]). Frustrated magnetic systems, whose energy degeneracy leads to fluctuations and non-zero entropy at low temperatures, can be observed by fabricating mono-domain in-plane magnetic structures next to each other and arranging them such that there is a degenerate lowest energy state. The collective dynamics of stray field coupled nanowires are a function of their structure, being determined by wire spacing, thickness, and magnetization direction (in-plane vs. out-of-plane) [27]. Nanomagnetic particles in close contact next to each other can change the magnetic properties of individual particles, form magnetic domains across nanoparticles, and generate topological magnetic structures [26, 28].

The study of thin films in magnetism is one of the most practical, applicable areas of research in physics. Thin magnetic films have tremendous impact on many technologically important areas, such as magnetic storage and sensor technologies. For example, thin film magnetic systems were key to the Giant magnetoresistance effect, which was discovered in

1988 by Peter Gruenberg [29] and Albert Fert [30] and awarded with the Nobel Prize in 2007. This has enabled an unprecedented increase in storage density of magnetic hard drives in information technology, that led to the penetration of information technology in every day life and will lead to the Internet of Things.

Thin film deposition techniques are able to control thickness on the atomic(Å) scale. From a scientific perspective, thin magnetic films and multilayer heterostructures allow for customization of magnetic properties determined by the materials used and thickness of each individual layer. Layering magnetic materials on strong spin orbit coupling metals, such as Pt, leads to a perpendicular magnetic anisotropy induced by the interface. Since the shape anisotropy of thin films force them to be easy axis, and the induced perpendicular magnetic anisotropy (PMA) is interfacial, increasing the thickness of the magnetic materials reduces the PMA allowing for precise customization of anisotropy. More recently it has been discovered that certain spin orbit coupling elements can induce the inversion symmetry breaking anti-symmetric exchange Dzyaloshinskii–Moriya interaction (DMI) in magnetic materials. Similar to PMA, the strength of the DMI can be tailored by varying the thickness of the elemental layers. DMI gives rise to skyrmions and other topologically nontrivial structures, because it is energetically favorable with regards to DMI for spins to prefer non-colinear configurations [21].

Combing magnetic nanostructures with thin films multilayers has resulted in modification and generation of topological magnetic structures. Depositing multilayers onto Si nanoparticles generates a variety of coupled vortex circulation patterns [31] by inducing shape anisotropy in the multilayers. Nanomagnetic disks can be interlayer exchange coupled to thin films to generate skyrmions with varying topological charge [32]. Magnetic multilayer pillars have found a use in magnetic tunnel junctions, but have not been used to generate topological spin textures, yet [33].

1.3 Motivation and Scope

This dissertation seeks to address the following question: what novel magnetic behavior can be generated by exploiting the physics of structural and topological magnetism? In order to do this, nanomagnetic structures were designed and fabricated, and characterized

via a suite of state-of-the-art characterization techniques. Conceptually, the experimental work in this dissertation focuses on three systems, i.e., magnetic materials, which were structurally confined laterally through patterning, or vertically through stacking of thin layers into multilayers. The third system combines both structuring approaches and leads to novel topological spin textures.

The first scientific focus in this dissertation is the stray field induced interaction in arrays of nanomagnetic topological spin textures, which was investigated in magnetic vortex arrays, XY macrospins, and a new form of ferromagnetic materials created through jamming of paramagnetic nanoparticles at liquid-liquid interfaces.

The second scientific focus is on thin magnetic ferromagnetic and ferrimagnetic film multilayers used to generate magnetic skyrmions.

The last scientific focus in this dissertation is the combination of ferromagnetic nanostructures with magnetic multilayers that exhibit a strong perpendicular magnetic anisotropy or DMI, and lead to novel topological spin textures, such as target skyrmions or Hopfions.

Chapter 2

Theoretical Background

2.1 Magnetic Interactions

This section briefly summarizes the competing magnetic interactions that lead to various topological and structural spin textures. When dealing with static magnetic systems, the competition of magnetic energies leads to magnetic states which are local energy minimum. Those lead to the specific topological and structural magnetic phenomena, which are the main topic of this dissertation.

Symmetric Exchange

The most fundamental interaction of two spins is given by the exchange interaction. It is a local, i,e. a short range interaction coupling two neighboring spins $\mathbf{s}_\mathrm{i}$ and $\mathbf{s}_\mathrm{j}$ in such a way, that the lowest energy state, i.e. the ground state is achieved by either a parallel or antiparallel alignment between $\mathbf{s}_\mathrm{i}$ and $\mathbf{s}_\mathrm{j}$. This interaction can be described by the following Hamiltonian, with the sum over all neighboring spins:

$$\hat{\mathrm{H}} = -\mathrm{J} \sum_{\mathrm{i,j}} \mathbf{s}_\mathrm{i} \cdot \mathbf{s}_\mathrm{j} \tag{2.1}$$

It is symmetric in the exchange of $\mathbf{s}_\mathrm{i}$ and $\mathbf{s}_\mathrm{j}$, and is therefore referred to as symmetric exchange interaction. J is a material specific exchange constant, with $\mathrm{J} > 0$ for ferromagnetic materials, and $\mathrm{J} < 0$ for antiferromagnetic and ferrimagnetic materials, where for the latter ones, the

magnitude of $\mathbf{s}_i$ and $\mathbf{s}_j$ are different. Ferrimagnetic and ferromagnetic materials have a net magnetization, $\mathbf{m}$. For ferromagnetic and ferrimagnetic materials the corresponding energy density is

$$E = A \int (\nabla \mathbf{m})^2 dV \tag{2.2}$$

with A being the exchange stiffness constant, which is material dependent. This energy density reproduces the effects of symmetric exchange: the energy is minimized when all spins are aligned in the same direction and that direction is arbitrary.

Anisotropy Energy

Magnetic materials can have an intrinsic preference for the magnetization to favor pointing in one or more directions: this is anisotropy and is represented by the anisotropy energy. In this section we will discuss anisotropy arising from intrinsic structures of the material, such as the crystalline structure of a material or an interfacial effect in magnetic multilayers. This is different from shape anisotropy, the magnetic anisotropy arising from stray field energy minimization, which is dependent on the shape, size of the material.

The anisotropy energy density is [34]

$$E_{ani}(m_i) = K_0 + K_1 F_1(m_i) + K_2 F_2(m_i) + ... \tag{2.3}$$

where m_i is the magnitude of the magnetization along a unit vector represented in some coordinate basis. F_i is a function determined by the material parameters and symmetries.

A commonly discussed form of crystalline anisotropy is for a cubic crystalline basis where the energy depends on the orientation between magnetization and crystalline axis. Cubic anisotropy has the energy density:

$$E_{cubic} = K_{c1}(m_1^2 m_2^2 + m_1^2 m_3^2 + m_2^2 m_3^2) + K_{c2} m_1^2 m_2^2 m_3^2 \tag{2.4}$$

with K_{ci}, given in J/m^3, being anisotropy constants, and m_i being the components of the magnetization aligned with the crystalline axis. In a cubic system, if a given magnetization direction is preferred by the anisotropy energy then the opposite magnetization direction is also energetically favorable; the anisotropy energy density is an even function in m_i. Let us consider cubic anisotropy in crystalline Fe and Ni, both of which are common magnetic

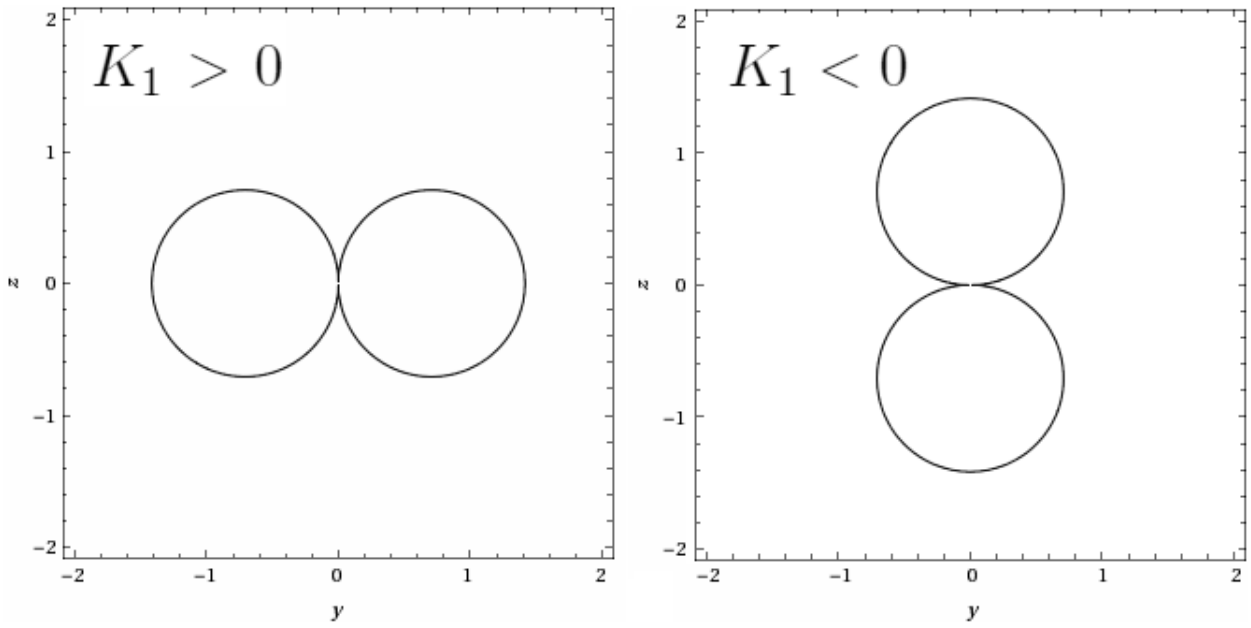

Figure 2.1: A constant energy surface of the anisotropy energy function in the z-y plane, for different values of K_1, $K_2 = 0$. The energy functions are rotationally symmetric about about the z-axis; for $K > 0$ the magnetization prefers to point in either positive or negative z and for $K < 0$ the magnetization prefers to lie in the x-y plane.

materials, and Fe mangetic nanomparticles with cubic anisotropy appears in this dissertation, Section.4.1.3. For crystalline Fe, $K_{c1} > 0$ and $K_{c2} = 0$, there are six degenerate low energy directions for the magnetization: three have the magnetization aligned with the crystalline basis, and three have them anti-aligned with the basis (the faces of the cube defined by the crystalline basis). For crystalline Ni, $K_{c1} < 0$ and $K_{c2} = 0$, there are also six degenerate magnetization directions, except they are the vertices of the cube defined by the crystalline basis. For poly(nano)-crystalline or amorphous materials crystalline anisotropy will average out to be zero.

Another form of anisotropy is uniaxial anisotropy: when a magnetic material has a (un)preferred magnetization axis; the energy is (highest)lowest when the magnetization is aligned or anti-aligned with a given single axis. Therefore uniaxial anisotropy can be expressed as series expansion in $\sin^2(\vartheta)$ where ϑ is the angle between the magnetization and the chosen axis.

$$E_{uniaxial} = K_0 + K_1 \sin^2(\vartheta) + K_2 \sin^4(\vartheta) + ... \tag{2.5}$$

For $K_2 = 0$ and $K_1 > 0$ it is energetically favorable for the magnetization to point along the given axis, the z axis in Fig.2.1 left, this is known as perpendicular magnetic anisotropy (PMA). For $K_2 = 0$ and $K_1 < 0$ the magnetization prefers to lie perpendicular to the given axis (Fig.2.1 right). A large portion of this dissertation focuses on thin films with perpendicular magnetic anisotropy, i.e films with $K_1 > 0$ and $K_2/K_1 << 1$. While hexagonal and tetragonal crystals show uniaxial anisotropy, the source of PMA in the thin films studied in this dissertation is interfacial in nature; specifically Pt, Ir layered next to Co induces a PMA in the Co that is perpendicular to the plane of the interface. This happens because Ir, Pt have elongated orbitals at interfaces with strong spin orbit coupling generating an effective PMA in the heavy metal element. When the magnetic material exchange couples with the heavy metal element it too experiences the induced PMA.

The energetic ground state in a material with only ferromagnetic exchange and an anisotropy energy is given by a uniform magnetization with its magnetization direction set by the anisotropy energy: it will be aligned with one of the minima of the anisotropy energy density function. Spatially varying anisotropy will compete with ferromagnetic exchange in a way that's similar to spatially varying structural anisotropy which will be discussed later.

Antisymmetric Exchange

In addition to the symmetric exchange there is the anti symmetric exchange, which is also called the The Dzyaloshinskii–Moriya interaction (DMI). This interaction describes the interaction of two neighboring spins. DMI is an inversion symmetry breaking exchange which causes a chiral canting of the magnetic moments of adjacent spins. The Hamiltonian for this interaction is

$$\hat{H}_{DMI} = \sum_{i,j} \mathbf{D}_{ij} \cdot (\mathbf{s}_i \times \mathbf{s}_j) \tag{2.6}$$

DMI is anti-symmetric with inversion of the spins: $\mathbf{s}_i \rightarrow \mathbf{s}_j$ implies $\hat{H}_{DMI} \rightarrow -\hat{H}_{DMI}$. It is important to note that $\mathbf{D}_{ij}$ is a vector whose axis is aligned with the symmetry plane for which inversion symmetry is broken. A positive $\mathbf{D}_{ij}$ energetically favors left handed alignment and a negative $\mathbf{D}_{ij}$ favors right handed alignment of adjacent spins.

For DMI with $\mathbf{D}_{ij}$ pointing out of plane, such as that found in the inversion symmetry breaking crystal FeGe, the energy density is, with $D = |\mathbf{D}_{ij}|$ [35]

$$E_{\mathbf{D}_{ij}\text{–OOP}} = D\mathbf{m} \cdot (\nabla \times \mathbf{m}) \tag{2.7}$$

Coupling a thin magnetic film to Ir or Pt causes $\mathbf{D}_{ij}$ to point in the plane of the material since this is the plane for which inversion symmetry is broken. The energy density in this case is [36]

$$E_{\mathbf{D}_{ij}\text{–IP}} = D(m_x \frac{\partial m_z}{\partial x} - m_z \frac{\partial m_x}{\partial x} + m_y \frac{\partial m_z}{\partial y} - m_z \frac{\partial m_y}{\partial y}) \tag{2.8}$$

Since D_{ij} is a vector, physically flipping a sample will cause $\mathbf{D}_{ij} \rightarrow -\mathbf{D}_{ij}$. For example a thin multilayer with Co on top of Pt [Pt/Co] has opposite sign D_{ij} as Pt on top of Co [Co/Pt] due to their physical inversion. Therefore a trilayer of [Pt/Co/Pt] has a reduced DMI since the DMI from the two Pt layers cancel each other out in the Co layer. An inverse effect for creating additive DMI does also exist: [Pt/Co] and [Ir/Co] have opposite sign DMI, therefore [Pt/Co/Ir] has a large DMI created by the effective addition of the DMI of Co with Ir and Pt.

A hypothetical system with only DMI will have neighboring magnetic spins align themselves at right angles to their neighbors, with a constant chirality, this leads to no net magnetic moment for large samples, as every other spin is aligned anti-parallel. DMI favors non-collinear spin structures where there is a constant rotation of the magnetization, such as magnetic skyrmions [37]. Unlike anisotropy energy or symmetric exchange energy, the DMI energy is reduced by domain walls (a domain wall is a non-collinear spin texture). A system with only ferromagnetic exchange and DMI will have spins that lie both in-plane and out-of-plane, and can form into a spin spiral (a constantly rotating magnetization) [37].

Introducing DMI into a thin film PMA system shears the hysteresis loop (Fig.4.19, Fig.4.24) which is characteristic of non-collinear magnetic structures, such as vortices (Fig.4.1). This shearing can be explained by nontrivial higher order terms in the uniaxial anisotropy and physically represents an increased impetus for the spins to lie in-plane; a sheared hysterisis loop can also be reproduced if one introduces small regions of easy plane anisotropy in a PMA system or DMI [38].

Zeeman Energy

Applying an external magnetic fields to a magnetic system add another energy term, the Zeeman energy. It can be described by

$$\hat{\mathrm{H}}_{\mathrm{Zeeman}} = -\frac{2\mu_{\mathrm{b}}}{\hbar}\sum_{\mathrm{i}}\mathbf{B}\cdot\mathbf{s}_{\mathrm{i}} \tag{2.9}$$

where, $\mathbf{B}$ is the externally applied magnetic field and μ_{b} is the Bohr magneton. The integrated energy density of this is

$$\mathrm{E}_{\mathrm{Zeeman}} = -\mathrm{M}_{\mathrm{s}}\int \mathbf{H}_{\mathrm{ex}}\cdot\mathbf{m}\mathrm{dV} \tag{2.10}$$

A material with only a Zeeman interaction (no anisotropy or exchange such as in a paramagnet), will have a uniform magnetization that is always aligned with the external field. A material with a Zeeman energy and ferromagnetic exchange, but no anisotropy (such as an XY spin in Section 4.1.2), will behave the same in an external field, but maintain its magnetization when the field is removed. A material with only Zeeman energy and anisotropy (such as a paramagnet shaped into a bar), will reproduce a magnetic hysterisis with no remanence, whose hard and easy axis are determined by the anisotropy.

Stray Field Energy

A magnetic field in space generated by a magnetic material has an energy density associated with it. The stray field energy is:

$$\mathrm{E}_{\mathrm{field}} = \frac{1}{2}\mu_0\int_{\mathrm{allspace}}\mathbf{H}^2\mathrm{dV} = -\frac{1}{2}\int_{\mathrm{sample}}\mathbf{H}\cdot\mathbf{M}\mathrm{dV} \tag{2.11}$$

From this energy equation we can see that the stray field energy is lowest when the field experienced by the sample is aligned with its own magnetization, a magnetic field in a paramagnetic or ferromagnetic material has lower energy than the same field in vacuum, and the stray field energy is always positive so the system will try and minimize it. A sample with ferromagnetic exchange, easy axis magnetic anisotropy, and stray field energy will seek to reduce the energy of the sample by forming domains of opposite magnetization aligned with the anisotropy axis. For very large exchange energy the demagnetizing field will be over

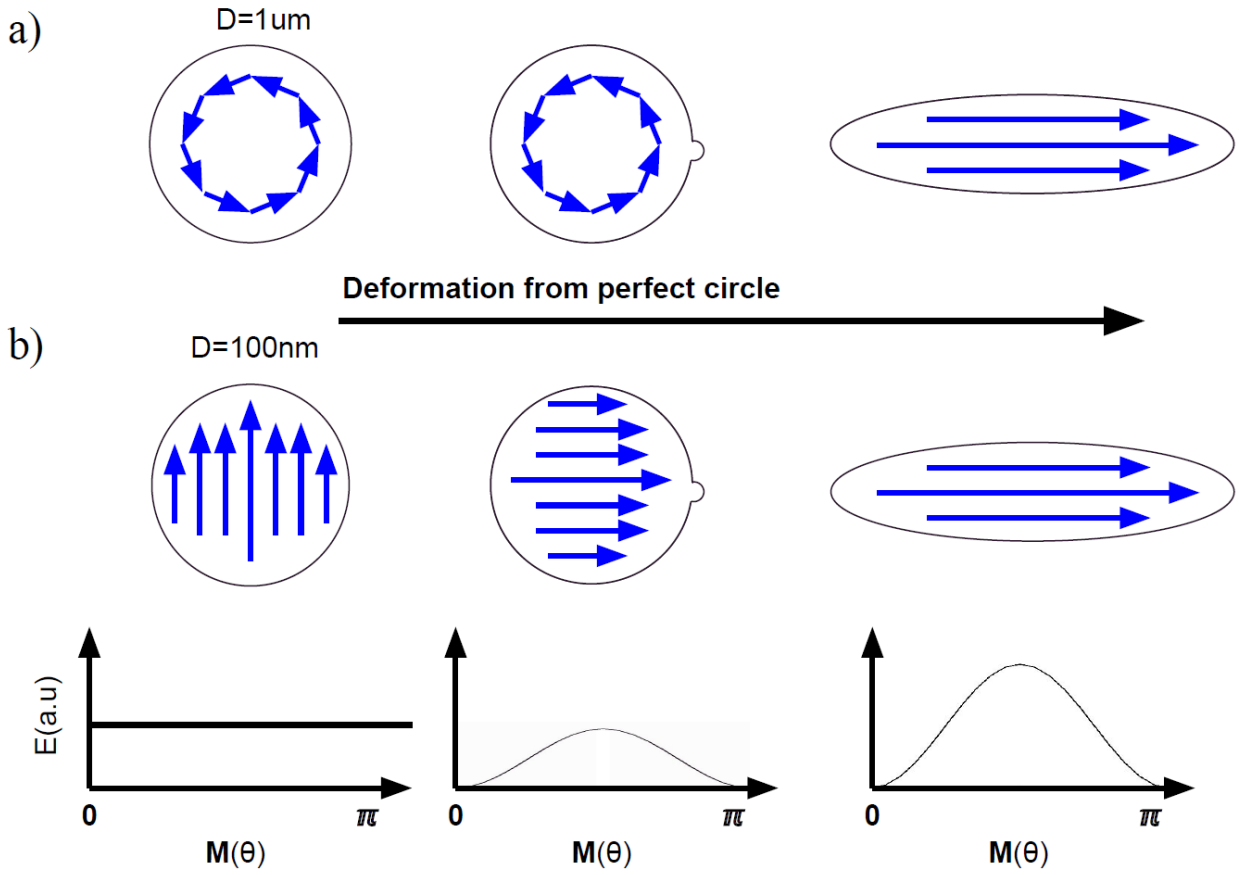

Figure 2.2: Deformation of a perfectly circular nanodisk made of PY with a thickness of 10nm with two different diameters. a) The disk with a 1μ diameter starts of in a vortex state. The vortex state remains until the disk is highly deformed turning into a monodomain state with a preferred anisotropy. b) 100nm diameter disk with its energy as a function of magnetization direction. The disk starts out as an XY macro spin with all in-plane directions equally energetically favorable. A small deformation creates a preferred anisotropy axis and an energy barrier between different states. The larger the deformation, the larger this energy barrier. $\vartheta = 0$ corresponds to alignment of the magnetization with the structural defect.

come and a uniform domain along the anisotropy axis will form. The stray field competing with exchange energy and anisotropy is the reason magnetic domains and domain walls form.

To see the effects of shape anisotropy on the magnetization of a finite sample consider the following from Maxwell's Equations:

$$\nabla \cdot \mathbf{B} = \nabla \cdot (\mu_0 \mathbf{H} + \mathbf{m}) \rightarrow \nabla \cdot \mathbf{H} = -\nabla(\mathbf{m}/\mu_0) \tag{2.12}$$

Since $\nabla \cdot \mathbf{B} = 0$and if

$$\nabla\varphi(\mathbf{r}) = \mathbf{H} \tag{2.13}$$

then the stray field energy is

$$\mathrm{E_{field}} = \frac{1}{2}\left[\int -(\nabla \cdot \mathbf{m})\varphi(\mathbf{r})\mathrm{dV} + \int (\mathbf{m} \cdot \mathbf{n})\varphi(\mathbf{r})\mathrm{dS}\right] \tag{2.14}$$

where $\mathbf{n}$ is the outwardly pointing surface normal vector of the sample. The first term is an integral over the volume of the sample, and the second term is an integral over the surface of the magnetic structure. To understand the effect on the local energy landscape of a given magnetization due to shape anisotropy in a finite sample, consider a very small region at the edge of the sample. This region is small enough to have uniform magnetization, and therefore $\nabla \cdot \mathbf{m} = 0$. The first term, the integral over the volume, is then zero. In this circumstance $\varphi(\mathbf{r})$ is an odd function of $\mathbf{m} \cdot \mathbf{n}$ which is a requirement for the total energy to remain positive. The total energy is therefore reduced in the second, and only remaining, term when the magnetization of the sample is orthogonal to the surface normal, $|\mathbf{m} \cdot \mathbf{n}|$ is reduced. Shape anisotropy can be thought of as an additional uniaxial easy plane anisotropy near the surface, where the easy plane is orthogonal to the surface normal [34]. The larger the magnetic moment per atom, larger the field generated by the magnet, the larger $\mathbf{m}$ is, and the stronger this effect is.

It is instructive to discuss concrete examples of how shape anisotropy effects the behavior of thin (10nm) ermalloy disks as their shape is modified; permalloy ($Fe_{20}Ni_{80}$) has a small coercivity, as low as 100A/m, with no innate anisotropy and is used as a prototype magnetic material found throughout this dissertation. For a large diameter, $> 2\mu$m, [39] disk the stray field energy exceeds the exchange energy and multiple magnetic domains are formed. In order to minimize the stray field energy these domains lie in the plane of the disk. A

slightly ellipsoidal disk will have an in-plane easy axis determined by the shape anisotropy such that $|\mathbf{m} \cdot \mathbf{n}|$ is small and domains will align with this easy axis. Permalloy disks with a diameter between 1.5μm and 250nm will be in an in-plane vortex state [39] (Fig.2.2a). This state is a balance between the energetic contributions of exchange energy and shape anisotropy. Exchange energy is low because there are no regions where there's an abrupt change in magnetization between adjacent spins, but very few spins are parallel with each other. Stray field energy is minimized in a vortex disk with only a small stray field coming from the out-of-plane core. For a disk that is in a vortex state, small deviations from a perfect circle will not modify the spin texture that much, this is because there are no stray fields generated at the edge of the disk (Fig.2.2a).

As the diameter of the disk gets reduced, the magnitude of the surface and volume integrals associated with the stray field energy get lowered, and therefore, the stray field energy is lowered relative to the exchange energy. For small diameter disks, e.g. with diameter of 100nm, ferromagnetic exchange overwhelms the stray field energy, and a uniform in-plane domain is formed that can point in any in-plane direction (Fig.2.2b). Shape anisotropy is more important for this monodomain state because for any small deviation from a perfect disk, there will be a preferred axis for the magnetization to align with (Fig.2.2a-right, b-right).

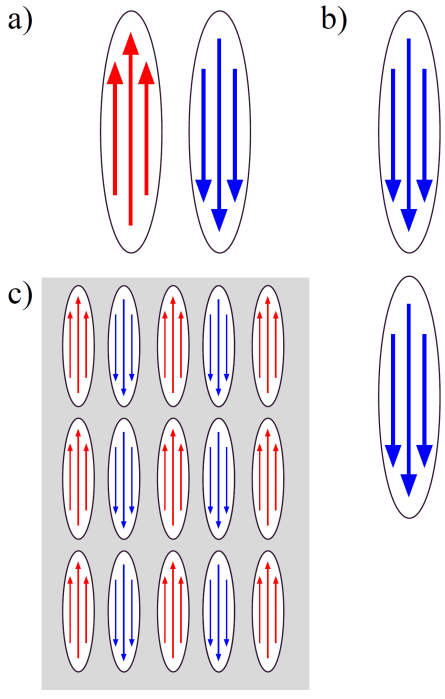

Figure 2.3: Unixial ferromagnetic islands interacting via their stray field. (a) Lowest energy configuration for nanomagnets a) aligned perpendicular to their anisotropy axis, b) along their anisotropy axis, and c) in a square lattice.

The stray field energy is also responsible for how magnetic structures interact with each other. This interaction is determined by the strength of the magnetic field generated by one heterostructure acting on another heterostructure. As an example, consider small fixed monodomain easy axis magnets interacting with each other to understand how the stray field energy is minimized (Fig.2.3). These magnets, which are used as model systems, e.g. in spin ice studies [40], can only point in one of two directions, along their major axis, and

will always remain in a single domain state. For two nanomagnets that are aligned along their major axis, the stray field will align the magnetization of the two magnets (Fig.2.3b). For magnets that are aligned along a hard axis the stray field will cause them to point in opposite directions (Fig.2.3a). In both cases the stray field energy is minimized when the field generated by one magnet aligns with the magnetization of the other magnets. If a square array of these magnets is formed, alternating magnetic domains will form similar to domains in a magnetic material (Fig.2.3c).

The example system described above is a two state magnetic system; each bar can only be in one of two distinct magnetic states. This is something that occurs throughout this dissertation and has been used to generate interesting topologically nontrivial magnetic textures, for example in artificial spin ice [40][41]. In order to quantitatively analyse the coupling between structures in a two state system as a function of distance, the spatial correlation function, g(r), can be calculated.

$$g(r) = \left\langle c_i c_j \right\rangle - \left\langle c_i \right\rangle \left\langle c_j \right\rangle \tag{2.15}$$

where $\langle ... \rangle$ denotes the spatial average over all nanomagnetic structures (i,j) separated by distance r with possible magnetic states for $c_i = (\pm 1)$ and $c_j = (\pm 1)$. Positive (negative) correlations occurs between structures with the same (opposite) state.

Interlayer Exchange Coupling

The last interaction, that is relevant for this dissertation, is interlayer exchange coupling (IEC). Two magnetic materials in close contact with each other, with a non-magnetic spacer layer in between, can have IEC: the total energy of the system is a function of the angle of the magnetization found in one layer relative to the magnetization in the other layer. IEC has many uses in fundamental magnetism and for application, most notably spin valves relying on giant magneto resistance and IEC to function. IEC typically arises from the Ruderman–Kittel–Kasuya–Yosida interaction[42], and as such it's sign and magnitude can change depending on the thickness of the spacer layer.

The most general energy density for interlayer exchange coupling is

$$E_{IEC} = C_1(1 - \hat{\mathbf{m}}_1 \cdot \hat{\mathbf{m}}_2) + C_2(1 - (\hat{\mathbf{m}}_1 \cdot \hat{\mathbf{m}}_2)^2) \tag{2.16}$$

where $\hat{\mathbf{m}}_1, \hat{\mathbf{m}}_2$ are the unit vectors aligned with the magnetization in each layer. C_1, C_2 are coupling constants that determine whether or not the coupling is ferromagnetic ($C_1 > 0, C_2 = 0$), antiferromagnetic coupling ($C_1 < 0, C_2 = 0$), or orthogonal coupling ($C_1 = 0, |C_2| > 0$).

With $C_2 = 0$ IEC energy density has the same form as surface anisotropy, and due to its depth dependence, can be thought of as a form of surface anisotropy [34]. IEC does not include contributions from the stray field energy: when there is IEC between magnetic materials whose magnetism is parallel to the vector separating the materials, there is an additional impetus for the magnetic moments to align. Conversely, when the magnetic moments are orthogonal to the vector separating the material there is an effective antiferromagnetic coupling so as to reduce the stray field energy.

In this dissertation IEC is important within the context of Ir and/or Pt, used to form multilayers with Co, and PY heterostructures weakly coupled with Co through Pt. In all cases $C_1 > 0, C_2 = 0$.

Varying the relative strengths of the stray field energy, DMI, anisotropy (both shape and intrinsic) allows for creation of a wide variety of spin textures and observable dynamics. In this dissertation systems were investigated, where through variation of the relative strengths of DMI, anisotropy, IEC, and stray fields energies novel topological spin textures occur.

2.2 Micromagnetic Simulations

To support experimental observation and to predict properties and behavior of magnetic materials in the energetic ground state, micromagnetic simulations are powerful tools and were also applied in this dissertation. In general, those simulations solve the LLG equation based on variable input parameters, such as structure of the system and materials parameters of the relevant materials. In this dissertation, two software packages were used: Nmag v.2.0 [43] and OOMMF [44]. They are open source and offer the flexibility to customize with individual modules [35, 45]. A custom finite difference simulation [46] was also used to simulate target skyrmions and Hopfions (Fig.4.31). The following paragraphs briefly summarize the major elements that were essential for the micromagnetic simulations performed in the context of this dissertation.

These finite difference, finite element simulations work in the following way: the magnetic material is divided into very small sections, finite elements, that have a uniform magnetization, $\mathbf{m}_\mathrm{i}$. Each of these elements can have different magnetic properties, coupling strength with adjacent sections. The simulation evolves in small, $<$ 1ns, timesteps where each finite element experiences an effective magnetic field, $\mathbf{H}_\mathrm{eff}$, which produces a torque on $\mathbf{m}_\mathrm{i}$ such that $\frac{\mathrm{d}\mathbf{m}_\mathrm{i}}{\mathrm{dt}} = -\gamma \mathbf{m}_\mathrm{i} \times \mathbf{H}_\mathrm{eff}$. $\mathbf{H}_\mathrm{eff}$ is a way of incorporating all the micromagnetic energies into a single effective field acting on each $\mathbf{m}_\mathrm{i}$, with [34]

$$\mathbf{H}_\mathrm{eff} = \frac{\partial \hat{\mathrm{H}}}{\partial \mathbf{m}_\mathrm{i}} \tag{2.17}$$

where $\hat{\mathrm{H}}$ is the Hamiltonian, which is the sum of all micromagnetic energies.

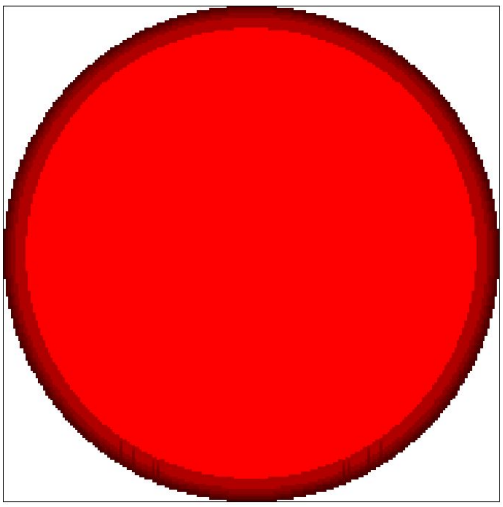

Figure 2.4: Simulation of $\mathrm{dm_z/dt}$ 30nm thick 1µm diameter permalloy disk initialized in a PMA domain state. Larger $\mathrm{dm_z/dt}$ corresponds to a darker color, hence the impetus to go in-plane is strongest at the edges of the disk.

These methods also account for the angular momentum, damping, associated with an individual spin if it was previously moving. Resulting in the Landau-Lifshitz-Gilbert (LLG) equation [47]:

$$\frac{\partial \mathbf{m}_\mathrm{i}}{\partial \mathrm{t}} = -\frac{\gamma \mathbf{m}_\mathrm{i}}{1+\alpha^2} \times \mathbf{H}_\mathrm{eff} + \frac{\alpha\gamma}{1+\alpha^2} \mathbf{m}_\mathrm{i} \times (\mathbf{m}_\mathrm{i} \times \mathrm{H}_\mathrm{eff}) \tag{2.18}$$

where γ is the gyromagnetic ratio and α is the Gilbert damping constant. The second term is proportional to $\mathbf{m}_\mathrm{i} \times \frac{\partial \mathbf{m}_\mathrm{i}}{\partial \mathrm{t}}$ so the magnitude of this term is often used as a conditional for stopping the simulation. Since $|\mathbf{m}_\mathrm{i}|$ is constant, when $\mathbf{m}_\mathrm{i} \times \frac{\partial \mathbf{m}_\mathrm{i}}{\partial \mathrm{t}}$ becomes small there is a negligible time evolution, even if this term never goes to zero.

In this dissertation, simulations were used as a way of developing physical intuition about a system, or as a way of identifying how a particular magnetic energy interacts with a system. For example identifying where the spatially resolved in-plane shape anisotropy is strongest in a nanomagnetic structure is difficult to experimentally measure, but by simulating a structure that matches our real systems and looking at $\frac{\mathrm{dm_z}}{\mathrm{dt}}$ it is possible to identify where the in-plane impetus is strongest (Fig.2.4).

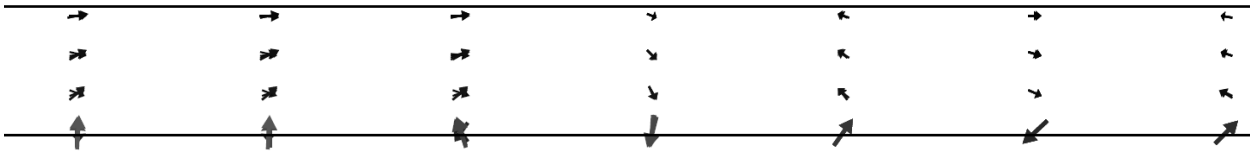

Figure 2.5: OOMMF simulation showing a cross sectional cut of a 30nm thick 1μm diameter Permalloy disk on top of 10nm of [Pt/Co/Ir] multilayers. The disk is canted out of plane by the multilayers below.

Fig.2.4 shows another example of an important simulation performed in this dissertation. There, a PY disk is coupled to a thin film with the properties of [Ir 1nm/Co 1.5nm/Pt 1nm] x 7 multilayer, found in section 4.3. The out-of-plane canting of the PY disk by the film underneath in Fig.2.4 is reproduced in experiment (Fig.4.26). In this system there are discrepancies between simulation and experiment; mainly, domain wall pinning in the DMI film is never reproduced and in experiment an anomalous in-plane magnetic structure is observed in the disks (Fig.4.26).

2.3 Topology and Magnetism

The impact of topology on magnetic structures is the focus of this dissertation. Therefore, in this section, a short mathematical description of topological mappings, examples of topologically nontrivial systems in physics, and why topological structures in magnetism are important and interesting is presented.

Mathematically, a topological property or structure is a vector field configuration of a parameter, i.e. magnetic spins, which can be assigned a topological constant. All vector field configurations of that parameter with the same topological constant can be smoothly permuted into each other. In this dissertation two different topological constants, and their topological structures, are considered: winding numbers, N_{sk}, and Hopf charges, Q_h, equivalently called the linking number. Both of these topological constants are used to classify different magnetic structures in this dissertation: Skyrmions and Hopfions, respectively. Sec.4.3.

When discussing topological mappings in physical systems, it is important to first identify the order parameter and its dimensionality because this dictates the types of structures that

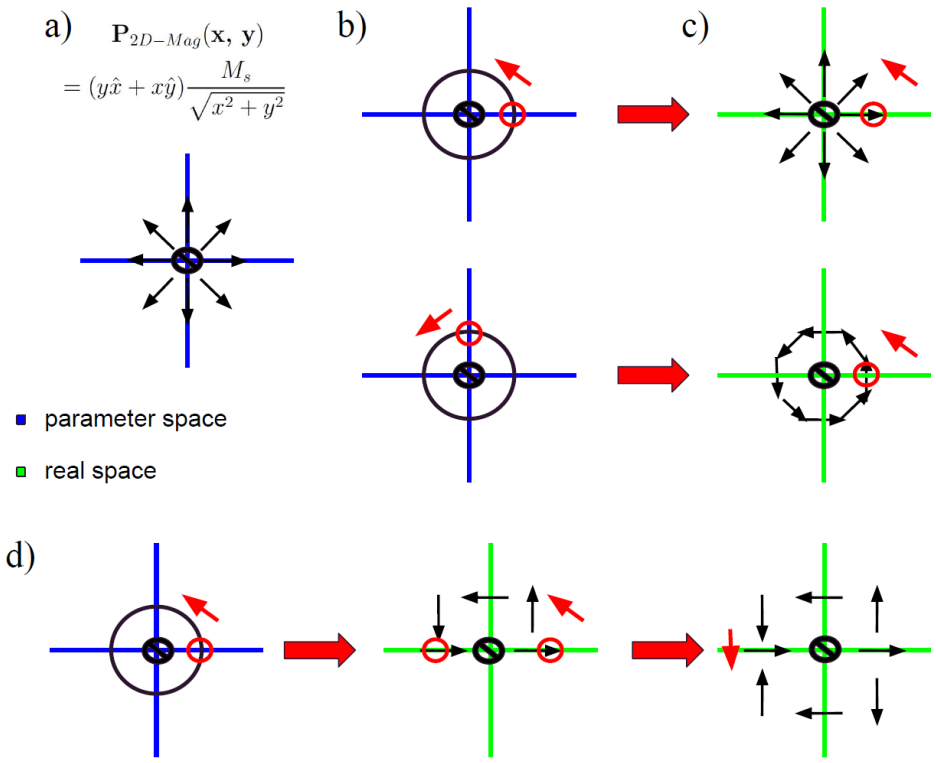

Figure 2.6: Mapping from a 2D parameter space to a 2D real space. In the following, red circles and red arrow indicate where the mapping starts in parameter (real) space and the direction of the mapping. Parameter space is noted with a blue axis, real space with a green axis. a) Parameter space with its parameterization defined and vectors shown for a fixed radius. b) Closed 1D membrane in parameter space surrounding the defect at the center. Red circles and red arrow indicate where the mapping starts in parameter space and the direction of the mapping. c) Resultant real space configuration of the parameter with winding number 1. d) Mapping of a structure with winding number 2. The first (second) real space image represents a mapping of the first (second) wrapping around the defect in parameter space.

can be topologically nontrivial based on the physical parameters of the system. The order parameter is the vector field which contains the topological structure, e.g. in magnetism, it is the spin as a function of position, in a topological insulator it is the electron spin as a function of momentum, in a hydrodynamic system it is the water velocity vector as a function of position. When the order parameter is a function of position, the term soliton is used to label the topological structure.

The dimensionality of the order parameter, N, is defined by the number of independent orthogonal axes, that the order parameter can point along. Magnetic spins can typically point in all three spatial dimensions, so they have a dimension of 3. However, spins confined to point in a plane, such as in spine ice or with XY macro spins, section 4.1.2, have a

dimensionality of two. Scalars, have a dimensionality of 1, but this is also the case with spins that are restricted to only point along one axis, ie up or down.

With the order parameter identified, the order parameter space can be defined by a smooth, almost everywhere, N-dimensional function that maps all possible states of the order parameter. For example, magnetic spins can typically point in any direction in three dimensional space, but always have the magnitude M_s/n_a, the magnetic moment per atom. As such the parameter space can be written as

$$\mathbf{P}_{\text{3D–Mag}}(\mathbf{x,\ y,\ z}) = (x\hat{x} + y\hat{y} + z\hat{z})\frac{M_s}{n_a\sqrt{x^2 + y^2 + z^2}} \tag{2.19}$$

or equivalently

$$\mathbf{P}_{\text{3D–Mag}}(\mathbf{x,\ y,\ z}) = (y\hat{x} + x\hat{y} + z\hat{z})\frac{M_s}{n_a\sqrt{x^2 + y^2 + z^2}} \tag{2.20}$$

Both are equivalent for topological mappings, note that both have a defect located at the origin of the space; a defect is a place where the order parameter vanishes and can occur in both parameter and real space. There is an arbitrarily large number of ways to parameterize this parameter space, but they will all have a defect at the origin. Having a defect located at the origin of the space is not a requirement for a parameter which can go to zero, for example the velocity of hydrodynamic systems can go to zero, so they can be parameterized by

$$\mathbf{P}_{\text{Hydro}}(\mathbf{x,\ y,\ z}) = (x\hat{x} + y\hat{y} + z\hat{z})C \tag{2.21}$$

where C is a scaling constant. In order for topological structures to exist in a hydrodynamic system, the condition that the water velocity remains constant, or non zero, would result in a defect in the origin of the parameter space. The fact that magnetic systems always have a defect in parameter space allows for topologically stable structures to exist in magnetic systems, unlike most condensed matter systems.

All smoothly varying vector fields in real space can be generated by mapping a membrane, which is defined as a closed set that is locally Euclidean, from parameter space to real space. This membrane is of dimension M where $M \leq N$. This type of mapping is called a directed mapping since it requires a start point and direction in parameter and real space. The most simple example of this type of mapping, a directed mapping, is a line (membrane with dimension 1) starting at (x=0, y=0, z=1) and extending to (x=0, y=0, z=∞) in

either parameterization of P_{3D-Mag}. All spins in parameter space that are on this line have $\mathbf{m} = M_s/n_a\hat{\mathbf{z}}$. This line when mapped to real space by a directed mapping represents a uniform magnetization: a 1 Dimensional line of uniform magnetization, when (R=1), a plane of uniform magnetization (R=2), or a uniformly magnetized magnetic particle (R=3). If this line is rotated about the origin, while pointing radially outward, this corresponds to a smooth rotation of the uniform magnetization of the real space systems. This is the most basic example of topological equivalency; since all uniform magnetization directions can be smoothly permuted into each other by moving this 1 dimensional membrane around in parameter space, they are all *topologically equivalent*. This line can be moved anywhere in parameter space as long as no part of it touches the origin, where there is a defect.

When a membrane in parameter space can completely enclose a defect it can not be smoothly permuted to any other state that does not enclose the defect, since the membrane cannot move though the defect. This is dependent on the dimension of the defect, parameter space, and membrane; For example a 2D-circle (a 1-sphere) can enclose a point defect when N=2 (Fig.2.6b), but cannot enclose a point defect when N=3; this is why a vortex structure (Fig.4.1) has a topological charge of 1 in an in-plane magnetic system (N=2), but has a topological charge of 1/2 when in a typical magnetic system (N=3). An example of a 2D parameter space is magnetic spins confined to point in a plane, such as found in XY spins, is (Fig.2.6a):

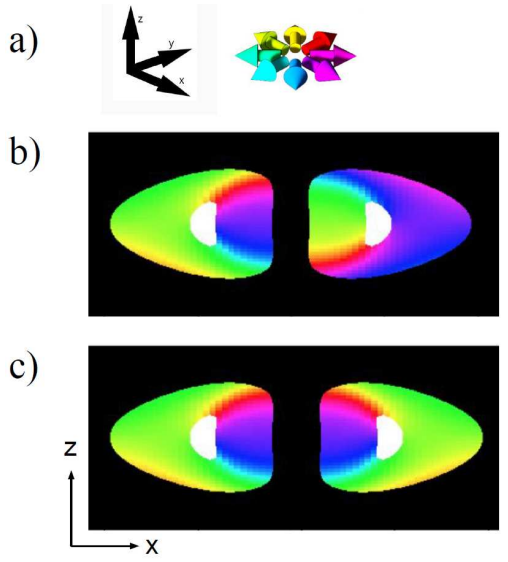

Figure 2.7: (a) X-y-z axis aligned with the x-y plane color wheel. Cross sections of a b) Q_h=1 Hopfion, and a c) Q_h = 2 Hopfion. In this case the Q = 1 Hopfion is rotationally symmetric, but the Q=2 Hopfion is not.

$$\mathbf{P}_{2D-Mag}(\mathbf{x},\,\mathbf{y}) = (x\hat{x} + y\hat{y})\frac{M_S}{n_a\sqrt{x^2+y^2}} \tag{2.22}$$

Fig.2.6 is instructive to understand what a directed mapping is with an example of a mapping from an N=2 parameter space to a R=2 real space, with a closed M=1 membrane. Fig.2.6 also explains why topologically equivalent structures can look differently depending

on how the mapping is done.

To map, one picks a starting point in parameter space and real space, the red circles in Fig.2.6b,c, then maps the parameter from parameter space to real space in a smooth manner. In Fig.2.6b,c the mapping of the function is continuous and covers the entire real space, except for the origin where the magnetization vanishes. Note that in both parameter and real space, the magnetization does not vary as one moves radially out from the origin.

Depending on where this mapping starts, in both parameter and real space, one can end up with different real space structures such as in Fig.2.6b,c. Both of these structures are topologically equivalent! A choice of different parameter space does not change the topological class of the real space configuration, but requires different mappings to end up with the same real space configuration. Another key element of the directed mapping, is that the membrane in parameter space can wrap the defect *more* than once, as seen in Fig.2.6d, the number of times the defect gets wrapped is the winding number. In a parameter space with at least one defect, membranes of a particular winding number can not be smoothly deformed into another configuration with a different winding number; hence the winding number is the topological constant used to distinguish different topological classes for skyrmions.

Explicitly calculating the winding number of a particular configuration depends on the dimension of the real space, R, the dimension of the membrane, M, and the dimension of the parameter space N. In this dissertation the vector field is always the magnetization, $\mathbf{m}$, and only two types of winding number calculations are relevant one for a parameter space of dimension two, and a real space of dimension two (spins confined to a plane, such as XY spins Sec.4.1.2):

$$\mathrm{N_{sk-2D}} = \frac{1}{2\pi}\int_0^{2\pi} \mathrm{d}\Phi \partial_\Phi \tan^{-1}(\mathrm{m_y}/\mathrm{m_x}) \tag{2.23}$$

and for spins with a 3D parameter space confined to a 2D plane.

$$\mathrm{N_{sk-3D}} = \frac{1}{4\pi}\int\int \mathbf{m}\cdot(\partial_\mathrm{x}\mathbf{m}\times\partial_\mathrm{y}\mathbf{m})\mathrm{dxdy}. \tag{2.24}$$

This is the winding number that one calculates for the bulk of this dissertation: thin film magnetic systems which host skyrmions. There is the assumption in these systems that the magnetization is uniform through the thickness of the film, and as such it can

be approximated as 3D spins confined to a 2D plane. Since all skyrmions with the same winding number are topologically equivalent, it is convenient to consider the magnetization of a rotationally symmetric skyrmion with a constant chirality whose center is located at the origin of the coordinate system:

$$\mathbf{m}(\mathrm{r},\varphi) = \mathrm{M_s}(\mathrm{Cos}\Phi(\varphi)\mathrm{Sin}\Theta(\mathrm{r})\hat{\mathrm{x}} + \mathrm{Sin}\Phi(\varphi)\mathrm{Sin}\Theta(\mathrm{r}), \mathrm{cos}\Theta(\mathrm{r})) \tag{2.25}$$

with Φ being the angle the magnetization makes with the x axis, and Θ the angle the magnetization makes with the Z axis. The magnitude of the in-plane component, out-of-plane component only depends on r (a requirement of being rotationally invariant). With this magnetization

$$\mathrm{N_{sk-3D}} = \frac{1}{4\pi}[\mathrm{Cos}\Theta]|_{\mathrm{r}=0}^{\mathrm{r}=\infty}[\Phi(\varphi)]|_{\varphi=0}^{\varphi=2\pi} \tag{2.26}$$

which is a useful way of calculating the topological charge of vortices, skyrmions, target skyrmions (skyrmions with more then a π rotation of the z component of magnetization), and $\mathrm{N_{sk}} > 1$ skyrmions.

Skyrmions have garnered much attention due to their perceived stability, however topological structures are essentially just a vector field configuration and whether or not they are stable in a system depends on the energetics of that system. For magnetics the requirement $\mathbf{m} \times \frac{\partial \mathrm{E}}{\partial \mathbf{m}} = 0$ [48], with E being the energy, must be met for a given magnetic configuration to be stable. For example skyrmions are not often stabilized in systems without DMI, and Bloch points, 3D solitons, are never favorable for systems with symmetric exchange. Additionally the topological mappings defined above make the assumption that the magnetization extends to infinite and that the vector field is continuous. In real magnetic systems neither of these conditions are truly met which allows for topological transitions to occur in real systems with finite energy.

In real magnetic systems topological stability is an additional energy barrier imposed by the geometric configuration of the spins requiring the transition through a highly energetically unfavorable state. In skyrmions this is the nucleation of a Bloch point required to unwind the skyrmion's core [49]. Since Bloch points require the magnetization at the center to vanish, the only reason a Bloch point can form in magnetic systems is due to the discreteness of the lattice. If the spin configuration was truly continuous it would take an

infinite amount of energy to nucleate a Bloch point, but in real systems it only requires a finite amount of energy.

Topologically non-trivial structures defined by a winding number can have a defect in real space, a place where the order parameter vanishes. The relationship between the dimension of the real space, R, the dimension of the membrane in parameter space, M, and the order of the defect, d, in real space [48]:

$$R = d + M + 1 \tag{2.27}$$

It follows that all 3D solitons in magnetic systems defined by a winding number, R=3, M=2, require a point defect, d=0. In magnetic systems this manifests itself as a Bloch point, so it follows that 3D winding number solitons are never stable in systems with ferromagnetic exchange because they require the magnetization to vanish at a given point, which is very energetically unfavorable.

However, 3D knot-solitons, known as Hopfions, can be stabilized in magnetic systems. In general Hopfions are vector field configurations containing a uniform field direction. The inside of the Hopfion is smoothly connected through the Hopfion structure to the outisde of the Hopfion which is uniformly antiparallel to the inside of the Hopfion. Every other field direction forms a closed loop with any given field direction Q_h number of times. Q_h is the Hopf charge and is the topological constant in Hopfion mappings. Hopfions with the same Q_h can be smoothly permuted into each other, but not structures with a different Q_h. In magnetic systems [50]:

$$Q_h = -\int \mathbf{B} \cdot \mathbf{A} dxdydz \tag{2.28}$$

where B is the emergent magnetic field and $\nabla \times \mathbf{A} = \mathbf{B}$.

For a given Q_h there are many different types of Hopfions which can be stabilized in magnetic systems with multiple coupling constants [46, 51]. In this dissertation we focus on a subclass of Hopfions: skyrmion tube Hopfions. These Hopfions are torus-like structures where each cross section of the tube is a skyrmion (Fig.2.7b,c, and Fig.4.32). These Hopfions can be built by extending the two dimensional structure of a skyrmion along its central axis (this central axis has to be perpendicular to the magnetization at the center of the skyrmion) and then closing the tube back on itself. The Hopf charge of these Hopfions is simply the

magnitude of the skyrmion number of a cross sectional cut times the number of "twists" in the tube. The number of "twists" in the tube is how many times the closed skyrmion loop is mapped to the torus (Fig.2.7).

2π target skyrmions (TSk) have been theorized to be a Hopfion's precursor: increasing the PMA at the top and the bottom of the TSk transforms it into a Q=1 Hopfion due to the shared symmetries between the two structures [46]. Q=1 Hopfions (Fig.2.7b, Fig.4.32) of this type are rotationlly symmetric, as opposed to Q=2 Hopfions (Fig.2.7). In this dissertation, Hopfions with $Q_h = 1$ are able to be stabilized in systems using target skyrmions as their precursor.

2.4 X-ray Magnetic Circular Dichroism

X-ray magnetic circular dichroism (XMCD) describes the difference in x-ray absorption for circularly polarized x-rays with magnetic elements depending on the alignment of the spin state relative to the the angular momentum of the circularly polarized x-rays. When circularly polarized x-rays interact with a magnetic material there is a difference in the transition probability for left versus right circularly polarized light to be absorbed.

X-ray magnetic circular dichroism (XMCD) is the propensity for circularly polarized x-rays to have a different scattering cross section with magnetic elements depending on the alignment of the spin state relative to the the angular momentum of the circularly polarized x-rays. When circularly polarized x-rays interact with a magnetic material there is a difference in the transition probability for left versus right circularly polarized light to be absorbed. If the incoming x-rays are of an energy which corresponds to an energy band. XMCD also requires that the energy of the incoming x-rays match the energy of a band gap in the material being measured. In this dissertation particular attention is paid to the Co, Fe, and Ni $L_{2,3}$ edge, but XMCD can also be measured at the K, M edges. We define the XMCD intensity as the difference in absorption between left and right circularly polarized light, for a given energy ($\Delta I_E = |A_{L+} - A_{L-}|$).

XMCD can be described as a two step process: first there is a dichroic absorption determined by the total magnetic moment of the material (orbital and spin moment). Angular momentum conservation dictates that when the circularly polarized x-rays are absorbed their

angular momentum must be transferred to the electrons they excite. In a magnetic material there is an energy difference between states with different total magnetic moment which is in effect a spin- split energy band [52]; for a magnetic material at saturation the majority spin band is totally full so no transitions are allowed into this state with electrons who have angular momentum anti-parallel to the magnetic moment. Therefore, in a material with partially full spin-split energy bands the transition probability is higher for electrons which the x-rays can excite to have angular momentum opposite the direction of the magnetization. Since $\mathbf{k} \parallel \mathbf{L}_{\mathrm{ph}}$ (the angular momentum of the photon) only the component of magnetization parallel to the x-rays propagation vector gets measured; components of the x-ray's angular momentum perpendicular to the magnetization don't see a spin split valence band (the number of spin ups and spin downs are equal so there is no dichroic absorption). The XMCD intensity is proportional to $|\mathbf{m}|$ since the magnitude of $\mathbf{m}$ is proportional to the difference in the number of states for the spin split valence band.

The second step is as follows: for states which can conserve angular momentum in their transition, the probability of the x-ray exciting an electron with parrallel or anti-parrallel angular momentum is dependent on the specific orbital, spin states involved in the exictation. For $\mathrm{L}_3, \mathrm{L}_2$ transitions, Assuming a saturated magnetic material in the $\downarrow$ (the $\downarrow$ majority spin band is totally full) only circularly polarized x-rays which can excite electrons to the $\uparrow$ minority spin band can be absorbed ($\mathrm{m_j} = -\frac{3}{2}$ states can't be excited to a spin up state and are excluded). The transition intensity for the L edge from orbital $\mathrm{p_j}$ to orbital $\mathrm{d_n}$ due to circularly polarized light with angular momentum ± 1 parallel or anti-parallel to the magnetization of the sample is [52]

$$|\langle \mathrm{d_n}, \mathrm{m_l}, \mathrm{S}_{+\frac{1}{2}} | \sqrt{\frac{4\pi}{3}} \mathrm{Y}_{1,\pm 1} | \mathrm{p_j}, \mathrm{m_k} \mathrm{m} \mathrm{S}_{\frac{1}{2}} \rangle|^2 \tag{2.29}$$

with $\mathrm{Y_{l,m}}$ being a spherical harmonic. For the $\mathrm{L}_3(\mathrm{p}_{3/2} \rightarrow \mathrm{d_n})$ there is a 62.5% chance to excite an electron who's angular momentum is parallel with the incoming x-ray, and only a 37.5% chance when they are anti-parallel. For the $\mathrm{L}_2(\mathrm{p}_{1/2} \rightarrow \mathrm{d_n})$ edge these probabilities are 25% and 75% respectively; there is a greater chance to excite an electron whose angular momentum is anti-parrallel to the incoming x-ray. The sign difference in XMCD intensities at the different edges is due to the difference in spin orbit coupling, at the L_3 (L_2) edge the positive (negative) spin orbit coupling generates a photo electron with angular momentum

(anti-) parallel to that of the incoming x-ray. The difference in number of states in the p and s shell lead a difference in magnitude of XMCD at the L_3 edge, ΔI_{L3}, compared to the L_2, ΔI_{L2}, edge; this combined with the fact the angular momentum couples differently between the L_2, L_3 edges lead to the XMCD sum rules for the $L_{2,3}$ edge:

$$m_s = \mu_b \frac{\langle -\Delta I_{L3} + 2\Delta I_{L2} \rangle}{C}, m_0 = -2\mu_b \frac{\langle \Delta I_{L3} + \Delta I_{L2} \rangle}{3C} \tag{2.30}$$

where C is the absorption for linearly polarized light normalized by the number of holes in the valence band [53].

It has been assumed that the angular momentum of the circularly polarized light is parallel (or anti-parallel) to the magnetization of the sample, the light is perfectly circularly polarized, and the incoming x-rays have energy exactly equal to the energy of the $L_{2,3}$. In general the XMCD contrast (for a given energy) is proportional to

$$\Delta I_E \propto \Delta E_z P_{circ}\ \mathbf{m} \cdot \mathbf{L}_{ph} \tag{2.31}$$

with P_{circ} being the degree of circular polarization, and $\mathbf{L}_{ph}$ the angular momentum of the photon. It is important to see from this that XMCD picks up magnetic contrast that is parallel to the beam direction and that the strength of this contrast is proportional to the magnetization of the sample. ΔE_z is a scaling factor associated with the energy difference between the x-rays and the absorption edge; the larger the difference between the average energy of the x-rays and the energy of the absorption peak the smaller the XMCD effect is. The change in XMCD as function of energy also allows for element specific measurements.

Chapter 3

Experimental Details

In this chapter, various synthesis and characterization techniques, which were applied in this dissertation are briefly described. The synthesis of magnetic materials in this dissertation can be broken down into two independent processes; thin film deposition and lithographically fabricating (magnetic) nanostrcutures. On the nano or micrometer length scales, magnetic properties are controlled by the structure of the magnetic materials, so with both processes emphasis is given to making fabricated samples as close to ideally structured materials as possible: films and nanostructures with sharp well defined edges and minimal roughness. Additional attention was given to fabricating on silicon nitride (SiN) membranes, which enable transmission microscopy techniques.

Figure 3.1: An optical image of a Si wafer with an array of 2mm x 2mm a-SiNx membranes. Scale bar is 1cm.

The structural characterization of fabricated materials in this dissertation was accomplished using scanning electron microscopy and atomic force microscopy. Macroscopic magnetic properties of materials were measured using vibrating sample magnetometery. Nanomagnetic structures and properties were observed using quantitative electron yield XMCD magnetic transmission x-ray microscopy (MTXM), Lorentz transmission electron microscopy (LTEM), x-ray photoemission electron microscopy (XPEEM), and XMCD scattering.

3.1 Synthesis

3.1.1 Lithographic Methods

Lithography, an established technique to fabricate well-defined nanostructures, was used in this dissertation. Two lithography techniques were used to address various length scales: optical photolithography, for the fabrication of structures down to 5μm, and e-beam lithography allows for length scales down to 10nm. In this section a detailed overview of how microstructures and nanostructure were fabricated using photo or electron lithography and liftoff is given.

In lithography a chemical which changes composition upon exposure to light or electrons, a resist, is spread out over a substrate. The resist is then chemically changed in a spatially controlled way by exposure to photons or electrons. The areas where the resist is exposed can become either soluble or insoluble with respect towards a solvent known as the developer; if the exposed area becomes soluble this is called a positive resist, and if the exposed area becomes insoluble this is known as negative resist. After the exposed resist is submerged in a solvent, only select areas of resist are left forming the "resist image". In liftoff a thin film is deposited on top of the resist image and the sample is then submerged in a solvent which removes the remaining resist leaving the thin film where there was no resist. This

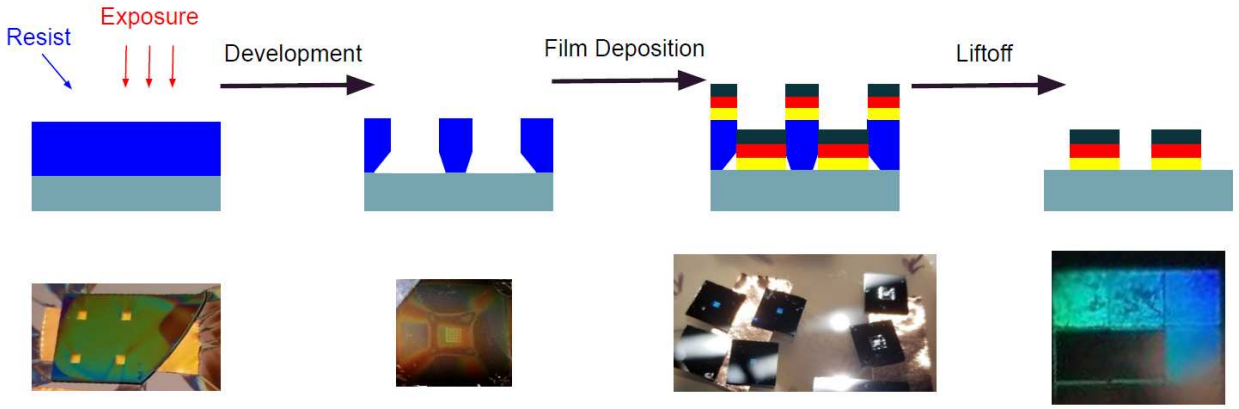

Figure 3.2: Liftoff workflow, with accompanying real space image of the process on a membrane taken with a cellphone camera. Note that for high quality ebl of periodic structures that have a length scale comparable to visible light iridescence should be observed post development. This is exemplified in the last figure which shows a dose variation of 500x500um arrays; at higher doses, no iridescence is observed.

process is schematically depicted in Fig.3.2. Near the edge of the lithographic pattern, there is a Gaussian decay in the number of photons, electrons interacting with the sample, and hence there is a change in composition that also has a Gaussian fall off near the edge of the exposed region which increases with a longer exposure time. During development, the amount of resist per unit time etched away is determined by the change in chemical composition, and hence the amount of resist etched per unit time has a Gaussian fall off as well which increases as a function of both the development time and exposure time. This means an increase in exposure time, can be compensated by a decrease in development time locally (or vice-versa). This can result in an undercut: resist near the bottom of a resist image is slightly etched away ensuring the deposited metal does not stick to the resist.

Spin Coating

The first step in resist based lithographic processes is to uniformly coat a substrate with the desired resist; resists of different thicknesses require different exposure, development times, so having flat, uniform resist every time is important for optimizing lithography. This is achieved via **spin coating**.

Spin coating a sample consists of taking a substrate with a liquid on it, spinning it around at thousands of revolutions per minute in order to uniformly coat the substrate with the liquid through a combination of centrifugal force, cohesion, and adhesion. In general, the liquid is a viscous solvent that contains some compound which is needed to be spread on the substrate, i.e., a resist. After spin coating, heating is then used to remove the solvent leaving a uniform layer of the compound on the substrate. In order to achieve a uniform coating of the resist, it is important to use clean substrates with a surface that whatever resist being used can adhere to. Substrates were cleaned by sonication first in acetone, then in isopropyl alcohol and then baked at 180C for 5 minutes to remove any excess liquid. An O_2 reactive ion etch or ozone clean is then performed, activating oxygen vacancies.

The spin coaters used in this dissertation were a Laurell WS-650Mz-23NPPB and a Cee Model 100CB spincoater. Both spin coaters can use a vacuum to keep a substrate adhered to the central pole which rotates and the Cee coater has various attachments to mechanically prevent larger substrates from spinning off the holder.

Photolithography

In **photolithography** a photoresist, a photactive compound, is exposed to light whose wave length causes a chemical change in the photoresist. A photolithography mask, composed of a transparent quartz holder and opaque titanium, determines where the light is able to interact with the sample, and sets the pattern to be developed (Fig.3.3). After exposure the sample is submerged in the developer and the resist image is formed. Next, a a thin film is deposited, usually in an anisotropic way, on top of the resist image. The sample is then submerged in a solvent which removes the remaining resist leaving the thin film where the was no resist. In this dissertation photolithography was used to fabricate large ($> 1\mu m$) non-magnetic structures that were required to excite, or study magnetic structures i.e.: grounding bars and co-planar wave guides with liftoff. The photolithography exposure tool used in this dissertation was a ABM Manual Mask Aligner System With Split-Field Dual CCD Camera Alignment with an exposure dose of $14mJ/cm^2$.

The following process was used in this dissertation for photolithography on Si substrates. A pre-coat of hexamethyldisilazane (HMDS), spun at 2k RPM for 45s and baked at 100°C for 60s, helps with resist adhesion and the uniformity of the coating. MA-N 1420 Photoresist, which is sensitive to UV light, is then spin coated onto the substrate at 3k RPM, and 2 minute bake at 100°C removes any solvent leaving the photoactive component. Two development, exposure time combinations were optimized: one for small features with an anisotropic thin film deposition method, and the other method was optimized for a large undercut to allow for liftoff with isotropic thin film deposition techniques. The two times used were an exposure time of 6.5s with a development time of 55s and an exposure time of 45s with an 80s development time. Ma-d 533/S was used as the developer and an N_2 blower was used to quickly remove the developer after the desired

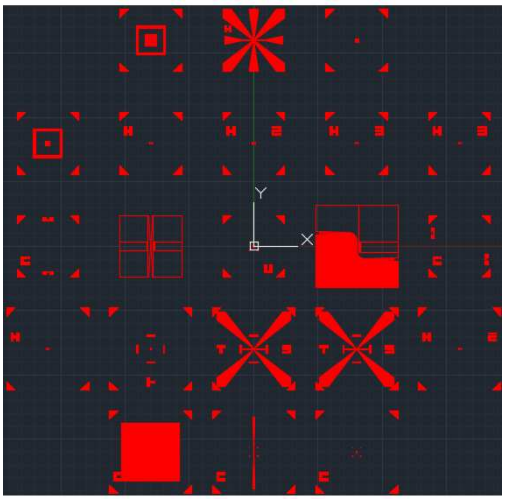

Figure 3.3: Example of a photolithography mask used in this dissertation with a variety of electric contatcts designed for SiN membranes.

development time is reached. After development the thin film is deposited. The substrate is then sonicated in acetone for 20 minutes, to remove the resist and excess metal, sprayed with IPA, and N_2 dried.

Photolithography was performed on SiN membranes with Si frames edge length 5-10mm, but required modification because SiN membranes can break under pressure. SiN membranes can never be sonicated because they will break. For the pre-cleaning, acetone and IPA spray bottles are used. spraying at a high angle relative to the surface normal prevents windows from breaking. SiN membranes cannot be adhered to the spin coater via vacuum, as this will break the window. Therefore membranes are taped to a Si carrier wafer with double sided copper tape, and removed safely afterwards by heating the tape/ substrate to weaken the adhesion of the tape. The SiN membrane has to be centered manually on the spin coater to maximize the area of uniform resist thickness. Up to four SiN membranes have been spun at the same time while still coating the membranes in uniform resist. HMDS can not be used on SiN membranes with windows larger than 1mm x 1mm as the windows will break during the HMDS bake.

Several adjustments had to be made during the UV exposure for SiN membranes. The reflectivity of the SiN is lower than Si, as a result SiN membranes a need increase of 10% in the exposure time. This difference in exposure time can be very problematic for structures that extend from the frame to the membrane. After development and film deposition, an extended lift off is performed because sonication can not be used on membranes. The lift off can last for several hours to 24h depending on the feature size: the smaller the features the longer the lift off time. During liftoff, the SiN membrane is held upside down in the solvent, using either self closing tweezers or a transverse SEM holder, to reduce the stress on the membrane and to prevent metallic particulates that have come off during lift-off from landing back on the substrate.

Electron Beam Lithography

Electron beam lithography (EBL) is fundamentally the same process as photolithography: a resist which changes composition during exposure, is developed leaving patterned areas which don't have the resist. This is then used for lift-off, removing excess metal and

resist (Fig.3.2). The biggest difference between the two types of lithography is that the resist used in EBL requires interaction with high energy electrons to change its composition, instead of ultraviolet photons like in photolithography. In EBL a physical mask which blocks the substrate from being exposed is not used, instead a focused beam of electrons is rastered over the sample in the desired pattern, changing the resist where the beam is rastered. As such, the resolution of structures made in EBL can be on the order of 10nm and EBL resist is much thinner when spun (100s of nanometers thick instead of micro-meters), so it can't be used for thick structures or with isotropic deposition methods. In EBL it is important to consider how the sample and substrate interacts with electric charge; if the sample and substrate aren't electrically conductive electrons can be deposited during exposure and repel other electrons or otherwise effect the exposure. Si, $\rho = 6.4 \cdot 10^2 \Omega$m, is conductive enough where this is not an issue, but SiN, $\rho = \cdot 10^1 0 \Omega$m, is not. Using electrons also results in much larger lateral scattering and exposure, when compared to photolithography, on the order of 10um. High quality array fabrication of closely packed structures require EBL mask files with structures 10 percent smaller than desired and an intentional over exposure to ensure a large undercut (see both XY macrospins, and coupled vortices). Due to lateral electron scattering during EBL, dose per unit area was reduced as edge to edge spacing in an array was decreased or total lattice size was increased.

In this dissertation a Vistec VB300 Electron Beam Lithography System was used with a spot size less than 3nm allowing sub-10 nm features to be patterned. The resist used was polymethyl methacrylate (PMMA) C2, which is a positive EBL resist. The standard EBL process used for Si substrates in this dissertation is to clean the substrate, spin and bake HMDS, spin PMMA C2 resist at 2k and bake for 5 minutes. The exposure time is varied depending on the size and density of the structures to be fabricated; optimizing exposure dose is relatively easy to do in EBL as the pattern can be repeated multiple times on the same chip with different exposure dosages. A cold development is performed at $0 - 5°$C in isopropyl alcohol:water, 7:3, while sonicating. After development, to perform liftoff, the sample is sonicated in the solvent dichloralmethane (DCM) for 20 minutes, followed by an acetone spray, IPA spray, and a N_2 dry.

For EBL on SiN membranes the same modifications that allow for cleaning and spin coating the resist on SiN membranes for photolithography are applied. Since SiN membranes are

not conductive, after PMMA is on the membrane, aquasave TM, a conductive polymer, is spun at 2k and baked at 100°C for 1 minute, alleviating charging problems during exposure. Before development, aquasave TM is removed via a 5 minute water bath. The cold development process using sonication is not possible on membranes, so they are developed in 3:1 isopropyl alcohol:methyl isobutyl ketone for 60s. After thin film deposition, an extended lift off for 24hours with the membrane held upside down in DCM is performed. Afterwards, an acetone and IPA, rinse remove any remaining resist and undesired metal. For liftoff with no sonication of extremely small, densely packed structures or for films deposited using conformal deposition methods, a double layer resist technique was used for an enhanced undercut: before PMMA is spun onto the membrane, methyl methacrylate (MMA) is spun onto the membrane. MMA has a lower exposure dose than PMMA so for exposed areas more of the MMA is removed during development leaving an improved undercut.

Additional modifications are required for lift off done on TEM membranes. When spin coating TEM membranes, due to their small size, the centrifugal force can overwhelm the adhesion of the resist to the TEM membrane flinging off all the resist from the TEM membrane. To alleviate this problem, an HMDS layer is spun on TEM grids before PMMA to increase adhesion. When both the PMMA and aquasave are spuncoat on the TEM membranes, they are spun off 0.25cm off center. Spinning off center reduces the centrifigal force the membrane feels, but decreases the area of uniform resist coating.

3.1.2 Thin Film Deposition Techniques

Thin film deposition techniques allow for deposition of various materials with nanometer to atomic control over material thickness. The two methods used in this dissertation were magnetron sputtering and electron beam evaporation.

Electron Beam Evaporation

In **electron beam evaporation** electrons are accelerated off a heated thermionic element due to a voltage difference between the element and two accelerating voltage pads. A magnetic field bends the electrons such that they hit a "target" which is the material to be deposited. As the electrons hit the target the material heats up and evaporates slowly al-

lowing for deposition of films substrates suspended above the target. The reason e-beam evaporation is so much more controlled than thermionic evaporation is because when electrons hit the target a small number of high energy (high frequency) phonons are generated, as opposed to a large number of low frequency phonons generated due to resistive heating. Since attenuation depth is proportional to wavelength, e-beam evaporation sublimates a small part of the target very accurately allowing for film deposition with Å- scale control over thickness.

In this dissertation a custom built Semicore SC600 with an accelerating voltage of 8keV was used for all e-beam evaporations, requiring a vacuum of 10^{-5}Torr. E-beam evaporation was primarily used to deposit films that were to be nanopatterned by lithography, since it is a highly anisotropic deposition method. All of the closely packed nanostructures in this dissertation were made with permalloy ($Ni_{80}Fe_{20}$). Permalloy requires additional considerations when used in e-beam evaporation because the thermal expansion coefficient of permalloy is much larger than crucible which holds it. A half hour warm up (and cool down) period to reach the desired electron current on the permalloy target prevents the crucible from breaking. All permalloy structures were deposited at a rate of 0.1-0.3Å/s and in a very low pressure vacuum ($< 10^{-7}$Torr) to ensure minimal roughness. Up to six different targets can be loaded at once in the e-beam, but deposition of multilayers with a large number of repeats in e-beam evaporators can take hours, since there is a ten minute cool down period when switching targets in-situ. Loading different targets in the e-beam is easy when compared to sputtering, so it was also used to test the composition, magnetic properties of small multilayers, or deposit one off materials (such as a Pt overlayer).

Magnetron Sputtering

Magnetron Sputtering also has targets of the desired material which are slowly evaporated onto substrates suspended above the targets. These targets are first mounted into a crucible that is negatively charged. Right above the targets argon gas is positively charged by electrons accelerated in cyclotron orbits by a magnetron. The positively charged gas is accelerated to the negatively charged targets, knocking loose the target material which eventually deposits on the substrate. This process is semi-anisotropic, so deposition of sput-

tered materials on a closely packed ebl resist image results in a uniform film, making liftoff impossible.

In this dissertation the primary sputtering system used was a five gun AJA confocal magnetron sputtering system with LN2 cryojacket, base pressure < 8x10⁻8 torr. An argon pressure of 1.3mtorr, and an approximate rate of 0.4Å/s was used during deposition. In the sputtering system used, all targets are equipped with their own shutter, so the material being deposited can be changed in situ very quickly with sputtering. Sputtering was used to create all the multilayers detailed in this dissertation. Additionally sputtering can be used to evaporate multiple materials at at the same time resulting in an alloy (this is used to create the GdCo ferrimagnets).

3.2 Characterization Techniques

This section focuses on the characterization techniques used in this dissertation. Several microscopies were used to characterize the structures and magnetic properties of the samples in this dissertation. They include electron and x-ray based techniques with a spatial resolution as small as 2nm.

3.2.1 Macroscopic Magnetic Characterization

A **vibrating sample magnetometer (VSM)** was used to measure the macroscopic magnetic properties (M(H), M_s, M_r, H_c) of the magnetic materials in this dissertation. A VSM exploits the physical phenomenon that a temporally varying magnetic field produces an electric field. VSM relies upon the physical principle mathematically depicted in the integral version of the Maxwell-Faraday Law:

$$\oint \mathbf{E} \cdot \mathrm{d}\mathbf{l} = -\int \frac{\mathrm{d}\mathbf{B}}{\mathrm{dt}} \mathrm{dS} \tag{3.1}$$

In a VSM an electrical coil is placed next to the magnetic sample under investigation which is vibrated using a piezoelectric ossilator. As the sample is vibrated, the magnetic flux through the wire coil changes and an induced voltage is produced in the detector coils. The amplitude of this induced voltage is linearly proportional to the magnetization of the sample

[54]. VSM have an in-situ externally applied field in which allows for accurate, flexible hysterisis measurements of a wide variety of magnetic samples. The applied field has no influence on the signal the pick up coils generate, since it does not contribute to any time dependent change in magnetic flux through the coil.

In this dissertation VSM was the primary tool for measuring the hysteresis of magnetic samples due to its accuracy, wide field range, and flexibility to measure a wide variety of samples (the only inhibiting factor is if the sample can fit between the electromagnetic coils). The VSM used was Lakeshore model 7400 VSM, with maximum field of +-1.5 T, and a sensitivity of 0.1μemu.

3.2.2 Microscopic Structural and Magnetic Characterization

This sections covers non x-ray based advanced structural and magnetic microscopies. The techniques used in this section characterize the structural and magnetic properties of various materials with nanometer (or Å) resolution.

Atomic Force Microscopy

Atomic force microscopy (AFM) is a common scanning probe microscopy technique, that provides information about surface topology and lateral dimensions. AFM involves taking a fine probe tip and moving it slowly over the surface of a sample while keeping the distance between the probe tip and the sample constant. Rastering the tip over the sample and keeping track of the tip's relative height will produce a topographic map of the sample. In order to achieve atomic resolution using this technique accurate measurement of the probe tip's vertical position is required. This is achieved via a light lever set up: an ultrafine probe tip is attached to a flexible, reflective cantilever which has a laser focused on the cantilever right above the probe tip. This laser is reflected onto a position sensitive photodiode array so that small changes in tip height correspond to large physical motion of the laser on the photodiode allowing for atomic scale tracking of the tip's vertical position. The tip is held at a constant relative distance to the sample by keeping the force on the tip due to the sample -tip interaction constant. The force generated on the tip due to the sample at small distances has two different regimes with two different physical causes. At very small

separation between sample and tip, less than a nanometer, Pauli repulsion between electrons generates a strong repulsive force; this is contact mode AFM. When the tip is farther away from the sample, but still closer than 5nm, Van der Waals attraction pulls the tip and the sample together; this is non-contact mode AFM. [55] Since both of these forces are monotonic functions of the distance between sample and tip, by keeping the attractive or repulsive force constant the distance between sample and tip is kept constant and the sample topology can be mapped.

AFM with subnanometer spatial resolution requires a sample stage that is isolated from vibrations and piezoelectrics with subnanometer resolution of movement are required. Tip diameter also has a large effect on the lateral resolution of an AFM; features smaller than the tip diameter can't be resolved. In this dissertation non-contact, amplitude modulated dynamic AFM was performed using an Asylum MFP3D Origin AFM with 10-40nm diameter Silicon tips. AFM provides subnanometer vertical resolution and was used to measure subnanometer roughness of thin films, finely calibrate lithographic process and measure the height of sub-micron thick structures. AFM can also accurately measure the lateral distance between nanostructures, with 1nm lateral resolution. Even though AFM is performed in ambient conditions, there are restrictions on sample geometry and size. Samples with large, $> 1\mu$m, local changes in topography cannot be measured accurately due to the range of the tips piezoelectric, samples that are larger than 5cmx5cm can't fit in the AFM to be measured, and measurements performed on membranes are noisy due to the vibration of the membrane.

Magnetic Force Microscopy

Modifying the sample- tip interaction, AFMs can operate in various different modes to detect various material properties. In this dissertation **magnetic force microscopy (MFM)** was performed by using a ferromagnetic CoCr coated Si tip, with 10-50nm tip diameter. MFM is achieved by first performing a topology line scan with the tip to generate a height map of the sample. This allows for a second scan where the tip is kept a constant 20-70nm away from the surface. In the second scan, when the tip is 20-70nm away from the sample, sample-tip interaction is restricted to magnetic forces.

During the second scan, the phase shift for a cantilever oscillating in the Z direction is $\Delta\varphi = \frac{\partial F_z}{\partial z} C$ where C is a constant. The magnetic force on a tip with magnetization $\mathbf{M}$ from a sample's stray field $\mathbf{H}$ is $\mathbf{F} = (\mathbf{M} \cdot \nabla)\mathbf{H}$. For a tip where $\mathbf{M} = M_z \hat{z}$ then $\mathbf{F} = M_z \frac{\partial H_z}{\partial z} \hat{z}$, and since H_z monotonically increases the closer the tip is to the surface, $\Delta\varphi > 0$ when M_z, H_z are parallel and $\Delta\varphi < 0$ when they are anti parallel [55, 56]. Therefore, measuring the phase shift as a function of position maps the z component of the stray field generated by the sample.

MFM produces nanometer scale magnetic images of topology and magnetic signal, but has the same physical, topological restrictions on sample geometry and size as AFM. Sample magnetization and coercivity are also important factors to consider when performing MFM; for samples with large M_s it is possible to flip the magnetization of the probe tip, and samples with low coercivity can have their magnetization flipped by the probe tip. Using a tip with the correct magnetization, coercivity, and adjusting the height of the magnetic line scan are all ways to address these problems. In this dissertation MFM has primarily been used for initial microscopic magnetometry screenings to qualitatively check for PMA, check the magnetization of small magnetic structures, and to identify the full magnetization of well defined/ simulated magnetic heterostructures such as magnetic vortices or films with strong PMA.

Scanning Electron Microscopy

All **Scanning Electron Microscopes (SEM)** have an electron source where electrons are accelerated to somewhere between 0.5 and 40KeV from a low work function element filament, often tungsten. The electron beam accelerated off the thermionic element has a diameter of 15μm to 20μm which is too large to have better resolution than an optical microscope. One or more electromagnetic condenser lenses adjust the electron beam to as fine a point as possible while directing it to hit the sample. When the electron beam hits the sample loosely bound electrons in the first 5nm are released, contributing to the SEM signal. [57] The electron beam is then rastered over the sample with a electromagnetic scanning coil. Image resolution is dependent on the spot size of the electron beam and its raster speed. In an SEM image each pixel corresponds to the full average intensity observed by the detector

due to the impinging electron beam on the sample. This is different when compared to an optical microscope which looks at photons coming off all different parts of the sample at the same time. In order to change magnification on an SEM, no physical changes are made to the lenses, rather the raster speed, pixel size of the SEM screen are adjusted to that each pixel corresponds to the average electron intensity of a smaller area. SEMs used in this dissertation operate in low vacuum, 10^{-6}torr.

In this dissertation SEM is used as the primary structural characterization of fabricated nanostructures. There is great flexibility in the type, size and number of samples that can be mounted in the SEM. Typical imaging time is 10s and with up to 10nm resolution. SEM measurement were for physical structure only. Secondary electrons and backscattered electrons were the electrons measured/ detectors used.

Lorentz Transmission Electron Microscopy

Transmission electron microscopy (TEM) focuses a very high energy beam, using electromagnetic lenses, on a sample and the transmitted electrons are measured by a CCD giving information about structure and elemental composition on the atomic scale. When a TEM is in focus there is no magnetic information in the resulting signal. Fresnel mode **Lorentz TEM (L-TEM)** generates magnetic contrast by defocusing the electron beam, via a Lorentz lens, which causes electrons to be deflected by the Lorentz force due to the in-plane magnetic induction field, see Fig.4.19. Mathematically this can be represented as the change in intensity, $\Delta \mathrm{I}(\mathrm{x},\mathrm{y})$ caused by a small change in the focus, $\Delta \mathrm{z}$:

$$\frac{-\mathrm{e}2\pi}{\mathrm{t}\hbar\lambda}\frac{\Delta \mathrm{I}(\mathrm{x},\mathrm{y})}{\hat{\mathrm{z}}} = \nabla_{\mathrm{xy}}[\mathrm{I}(\mathrm{x},\mathrm{y})(\mathbf{m}\times\mathbf{n}_{\mathrm{z}})] \tag{3.2}$$

where λ is the electron wavelength and t is the sample thickness.

This results in 2-4nm resolution images of the in-plane magnetic induction field, which is the highest resolution magnetic microscopy used in this dissertation (Fig.4.21). LTEM is used in this dissertation to extract information about the in-plane component of magnetization, which is needed in order to confirm topological magnetic structures. Since LTEM does not reveal any information about the OOP component of magnetization, it is often used in conjunction with other magnetic microscopy techniques.

3.2.3 X-ray Based Spectromicroscopies

To study magnetic materials with polarized x-rays, x-ray magnetic circular dicroism (XMCD) measurements either measure the number of photons absorbed or reflected from a sample, or the number of electrons emitted when circularly polarized x-rays interact with a magnetic sample. The intensity of an XMCD measurement, i.e. the number of transmitted or reflected photons, or secondary electrons depends on the relative orientation between the helicity of the incoming circularly polarized photons and the projection of the local magnetization onto the photon propagation direction. In combination with spatially resolving spectromicroscopies, XMCD allows one to image magnetic domains with high spatial resolution down to about 10-30n,

Quantitative XMCD Spectroscopy, was performed at Beam Line (BL) 6.3.1 at the Advanced Light Source (ALS) in Berkeley, California which measures electron yield when circularly polarized x-rays hit a sample, is surface sensitive due to the limited escape depth, 5nm [57], of secondary photoelectrons. Using XMCD sum rules, the spin and orbital moment are able to be extracted, as done in Fig.4.20. 6.3.1 has in-situ- variable magnetic field of 2.5T and is flexible with regards to sample geometry.

X-Ray Photoemission Electron Microscopy

Spectromicrosopic magnetic imaging can be performed with electrons emitted by circularly polarized x-rays hitting a sample by focusing the emitted electrons onto a CCD. This is called **X-ray photoemission electron microscopy (X-PEEM)**. In this dissertation, X-PEEM was performed at ALS BL 11.0.1.1, PEEM-3. After coherent x-rays hit the sample electrons are accelerated off the sample, due to a 10-18KeV potential on the sample, through an objective lens and several field lenses, bounced off a Hartmann mirror to correct for chromatic aberration, and focused onto a CCD camera. PEEM-3 allows for sub 100nm resolution magnetic imaging

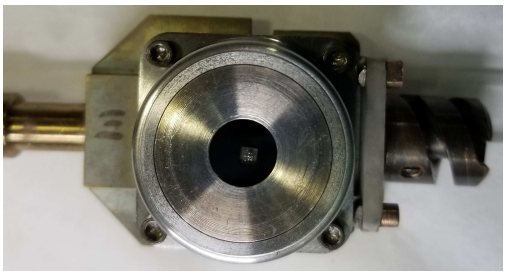

Figure 3.4: A 1cm x 1cm Si Frame with a 2cm x 2cm SiN membrane mounted in a PEEM-3 sample holder. Sample S30 from section 4.3.3 is visible.

[58]. Since X-PEEM measures emitted electrons, X-PEEM is only sensitive to the first 5nm-8nm of material [57].

In PEEM-3, x-rays hit the sample at a 30° angle relative to the plane of the sample (60° to the sample normal) picking up magnetic contrast that has both in and out-of-plane components. A rotational sample holder allows for full three dimensional reconstruction of the observed magnetic signal, by rotating about the sample's normal axis. Comparing XMCD images recorded at various angles allows to distinguish in-plane and out-of-plane signals. Assuming the sample starts at $\Theta = 0°$, adding the $\Theta = 0°$ and $\Theta = 180°$ images gives the out-of-plane magnetic signal since the in-plane signal reverses, but the out-of-plane signal stays the same. Removing the out-of-plane signal from $\Theta = 0°$ and $\Theta = 90°$ allows for reconstruction of the full in-plane magnetic signal.

Sample geometry and composition are essential factors to consider when imaging in PEEM-3. The sample holders can only hold samples that can fit in a circle with a diameter between 3mm and 17mm (Fig.3.4). The area being imaged needs to be in electric contact with the edge of the sample holder to avoid charge build up. This can be particularly problematic with isolated structures, but conductive over/under-layers can be deposited to alleviate this problem.

Magnetic Transmission X-Ray Microscopy

In full field **magnetic transmission x-ray microscopy(MTXM)** a condenser lens focuses light onto a sample and an objective lens projects an image onto a CCD (Fig.3.5). In this dissertation two different MTXM microscopes were used: BL 6.1.2 at the ALS, XM-1, and BL 09, MISTRAL, at the ALBA synchrotron in Barcelona, Spain. XM-1 has a condenser zone plate and a micro zone plate which act as the condenser and objective lens, respectively. Fresnel zone plates are circular gratings with a linearly increasing line density in the radial direction which focuses light as a function of wavelength [59]. For a given focal length, ring spacing, thickness is proportional to the square root of the wavelength of the zone plates; soft x-rays require ring spacing, thickness on the order of 10nm. At MISTRAL a polarity grating mirror reflects light onto a single reflection glass capillary which focuses light onto the sample. After passing through the sample, light goes through a zone plate which focuses

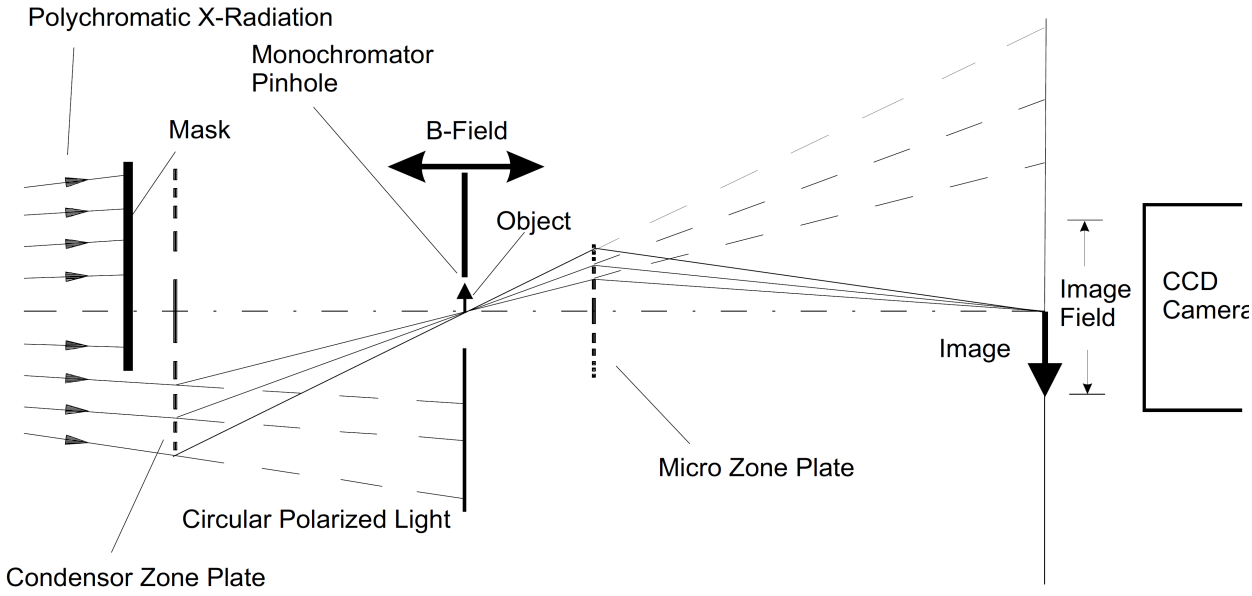

Figure 3.5: General Schematic for MTXM. In this dissertation XM-1 at the ALS has this setup. Reproduced with permission from [60].

it onto a CCD. The glass capillary is coated with a highly reflective material and designed such that all light passing through must reflect once, and only once, off the capillary in such a way that all light gets focused to a single point.

To measure different components of the magnetization samples are tilted relative to the x-rays momentum. XM-1 has a tilted (30°) sample holders that allow for measuring both a combination of out-of-plane and in-plane magnetic signal. MISTRAL has a variable tilt stage with an in-situ 70° major tilt axis and 65° minor tilt axis allowing for full tomographic reconstructions, but requires a TEM grid.

XMCD Scattering

The last micromagnetic measurement technique to be discussed is XMCD scattering. This is when coherent circularly polarized x-rays scatter off a magnetic sample and a scattering intensity, I, that is dependent on the XMCD scattering factor, f_m, and charge scattering, f_c is produced [52]:

$$I = |f_c|^2 + |f_m|^2 = |f_c|^2 + C\sigma^{abs} \tag{3.3}$$

where C is a constant and σ^{abs} is the absorption cross section. Hence circularly polarized light scatters differently depending on the magnetization of the sample relative to the momentum of the light.

XMCD scattering data gives information about periodic magnetic phases that cover a sizable portion of the sample; just like with charge scattering the scattering intensity pattern is built up via periodic structures and reflects the symmetries of what is being measured. Since $\frac{f_m}{f_c} << 1$ it is important that the physical and magnetic symmetries of the sample have different length scales, or drastically different symmetries. XMCD scattering can be measured in transmission or reflection. In transmission the beam is parallel to the normal of the sample, and gives information about out-of-plane magnetic component. Reflection can be done at a large angle, relative to the surface normal, to give information about the in-plane component. In the course of this dissertation XMCD scattering was tried on several samples (XY spins, coupled vortex, Fe/Gd). Working with thin films insures that the periodic size scale of the charge (atomic spacing) is much smaller than that of the magnetic structure and is preferred for XMCD scattering.

Chapter 4

Results and Discussion

In this section results on a variety of systems that illustrate the relationship between interacting nanomagnetic heterostructures and topologically protected spin textures are presented. Emphasis is given to results that establish how topologically nontrivial magnetic structures are stabilized or the energies that contribute to their stabilization, and how heterostructures interact with each other and multilayers.

Nanomagnetic heterostructures encompass both nanometer thin film multilayers and structures with dimensions on the nanometer scale that are magnetic. Both of these types of heterostructures allow for customization of magnetic properties through shape anisotropy, and other interfacial effects. Additionally, the combination of multiple nanomagnetic structures interacting with each other, or with magnetic films, has been shown to generate topologically protected spin textures.

Interacting nanomagnetic structures, whose magnetization is determined by their shape anisotropy, have generated topological structures and collective magnetic properties that contrast with the properties of the individual nanomagnetic structures. The first example of this, described here, is a study of the properties of interacting topologically nontrivial nanomagnetic vortex structures, with $N_{sk} = 1/2$, in permalloy disks observed in MTXM [61]. The results from that study provided information about how closely packed nanomagnetic disks interact through their stray field, which led to the study of interacting XY macrospins. There, each individual disk is superparamagnetic due to its shape anisotropy [62]. Collective ferromagnetic behavior induced by array structure and topologically protected spin textures

are revealed in the macrospin arrays.

Similarly, a transition from paramagnetic behavior to ferromagnetism in magnetic nanoparticles that are jammed at liquid-liquid interfaces led to the discovery of reshapable ferromagnetic liquids [63].

This section will also describe examples where topology impacts the spin textures. These studies use the various competing magnetic interactions to stabilize skyrmions and other topologically nontrivial magnetic structures in thin films. The systems studied include Fe/Gd heterostructures showing magnetic skyrmions [64] and asymmetric stacks of Ir/GdCo/Pt exhibiting ferrimagnetic skyrmions [65].

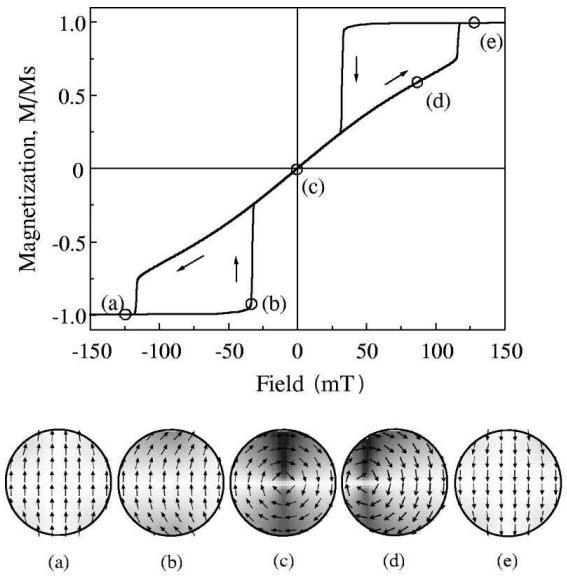

Figure 4.1: The magnetic hysteresis of a vortex disk (top) with schematics of the vortex disk at the applied field (bottom). The vortex disk is primarily in-plane except for a small out-of-plane core that can be seen in c,d. At zero field, the vortex generates no external in-plane stray field, c. Reprinted figure with permission, from [39]. Copyright 2017 by the American Physical Society.

Combining thin multilayers with shape anisotropy, via structural anisotropy imprinting, higher order target skyrmions were formed [66]. These TSks were also investigated as precursors of knot- solitons, known as Hopfions, as novel topological 3D spin textures in variable PMA multilayer pillars.

4.1 Stray Field Induced Spin Textures

The collective properties of micromagnetic and nanomagnetic heterostructures confined to a 2d and plane interacting through stray field have generated exotic (frustrated) phases, such as spin ice and spin glass [40], novel phase transitions, collective spin excitations in magnonic crystals [67, 68] and collective topological structures. In this dissertation, various systems, arranged in high symmetry arrays, were investigated to understand novel magnetic behavior and topologically nontrivial spin textures.

4.1.1 Vortex Circulation Patterns

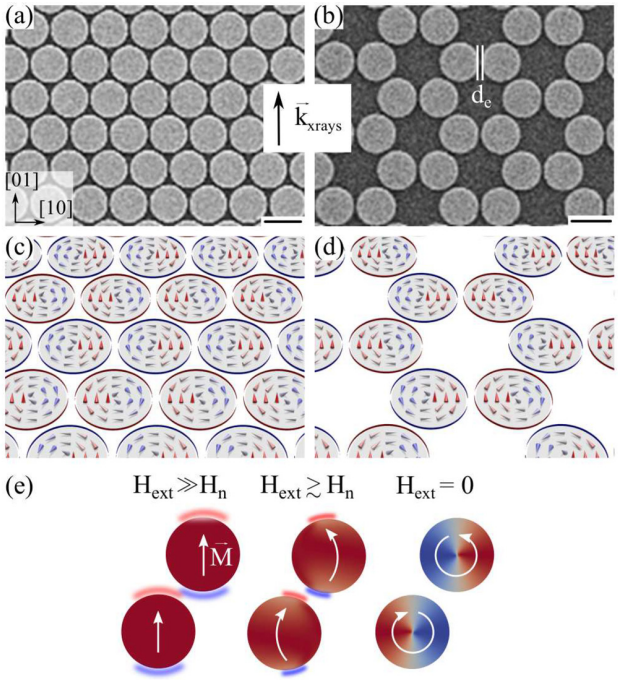

Figure 4.2: SEM images of 1μm diameter 40nm thick PY disks, separated by 70nm, arranged in a)hexagonal lattice and b) honeycomb lattice, with the [01] [10] directions defined. The inset shows the in-plane component of the incoming x-rays for MTXM measurements. The lowest energy ground state from simulation is shown for the c) hexagonal and d) honeycomb lattices. e) Example stray field interaction for two disks whose displacement vector from each other is at a 30° angle relative to the saturating field. Reprinted from [61], with the permission of AIP Publishing.

Note: Most of the results discussed in this subsection were previously published in the following paper: S. Velten, R. Streubel, A. Farhan, ***N. Kent****, M.-Y. Im, A. Scholl, S. Dhuey, U. Merkt, C. Behncke, G. Meier, P. Fischer,* Vortex circulation patterns in planar macrodisk arrays*, Appl Phys Lett 110, 262406 (2017).*

Magnetic vortices and skyrmions, both chiral spin textures, share a significant overlap in their behavior due to their stability and nontrivial topological charge [21, 69–72]. Magnetic vortices represent the energetic ground state of the spin configuration in thin magnetic disks due to the competition of stray fields and shape anisotropy. Vortices have a constantly rotating in-plane component, with an out-of-plane core (Fig.4.1c) and $N_{sk} = 1/2$, see Sec. 2.3. The stray field generated by this spin texture originates from the magnetization of the small out-of-plane core only, and therefore is weak. In order to better understanding the collective properties of groups of topologically nontrivial nanomagnetic structures as a function of their collective arrangement magnetic vortex disks confined to a lateral plane and forced to interact via the stray field serve as a good model system.

For isolated magnetic disks there is an energy degeneracy in the circulation of the spin texture (clockwise, or counter-clockwise) and the polarity of the out-of-plane core (up or down). There is also, a priori, no preferred combination of polarity and circulation (chirality).

Magnetic vortices which are arranged in arrays, can couple via their stray fields from the core, which leads to collective order in the polarization [23, 73, 74]. The magnetic vortex disks can have their chirality coupled, via their stray fields, by applying a strong in-plane fields to unwind the vortex state (Fig.4.2), but this has only been done small sets of disks [75].

In the following, hexagonal and honeycomb vortex disks lattices, with different lattice constants, will be described by detailing the impact of stray field interaction on the observed spin textures and resultant chirality patterns. Varying the lattice type allows for different arrangement and numbers of nearest neighbors, which results in different chirality patterns. Varying the inter disk spacing changes the strength of the magnetostatic interaction between disks resulting in different coupling strengths and pattern sizes. 1μm diameter 40nm thick permalloy disk arrays were fabricated using EBL, liftoff on SiN membranes. In [61] the vortex disks were arrayed in 25x25μm^2 honeycomb and hexagonal lattices lattices, with edge to edge spacing of 200nm, 100nm, and 70nm.

SEM images of the structures with the different array symmetry axis, [01] and [10], defined can be seen in Fig.4.2 a,b. In isolated Py disks of this size the magnetic vortex state is the lowest energy state, with an energy degeneracy in circularity and polarization, but when arrayed in lattices certain arrangements of the chirality are preferred depending on the direction of the saturating in-plane field relative to the orientation of lattice (Fig.4.3).

Looking at the hysteresis loop for vortex disks and its spin texture, as a function of applied magnetic field (Fig.4.1) it is clear that there is no in-plane stray field at remanence, the stray field is largest in the structures right after they are saturated, the vortex nucleation process happens over a very small field range and the chirality is determined by a slight canting of the saturated state (Fig.4.1b) which is random for isolated disks. As can be seen in Fig.4.2e, for a pair of disks the slight canting of the uniformly saturated state during vortex nucleation couples disks via the stray field which results in the chirality of the disks no longer being independent. Hence magnetostatic interaction during the vortex nucleation process from saturation is responsible for the chirality patterns seen in the disk arrays. A change in the orientation of the field relative to the disks, or a change in disk spacing, results in the disks experiencing stray fields of different strengths and orientations from other disks, and thus a different interaction strength between disks. The coupling between two disks can be

categorized by the relative angle of the displacement vector between the two disks and the saturating field: $(30°, 60°, 120°, 150°)$, hereby refereed to uniformly as 30°, result in opposite circulations.$(0°, 90°, 180°, 270°)$, result in same circulation. Note that the polarization of the core has no influence on the circulation coupling because the out-of-plane core isn't formed until after the disks have coupled their circulations, see Fig.4.1 and Fig.4.2c.

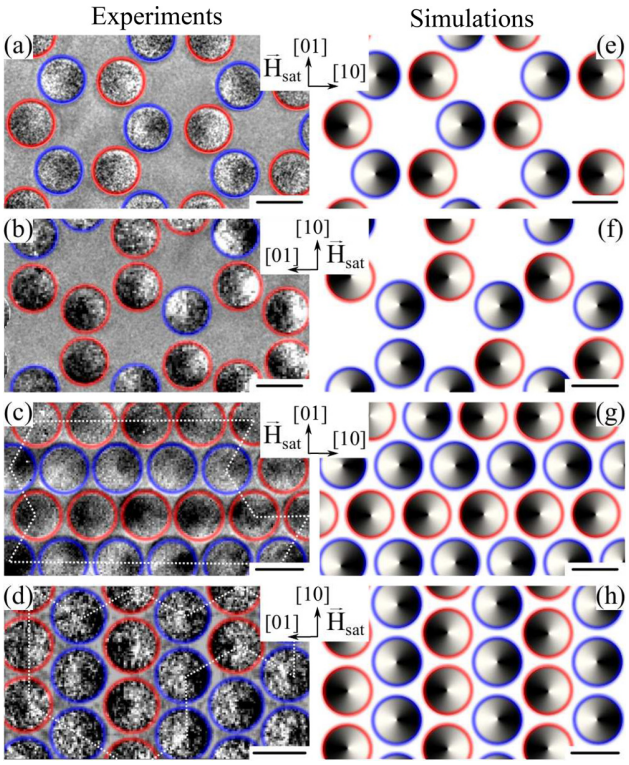

Figure 4.3: MTXM results for (a),(b) honeycomb and (c),(d) hexagonal lattices saturated along the [01] direction in (a),(c) and the [10] direction in (b),(d). The corresponding micromagnetic simulation (e-h) is next to the experimental results. Reprinted from [61], with the permission of AIP Publishing.

Micromagnetic simulations, to compare with experimental results, were performed by using Nmag and typical material parameters for Py [76] i.e., saturation magnetization Ms = 860 kA/m, exchange stiffness A = 1.3 $10^1$1 J/m, and no anisotropy. They confirm that different circulations patterns occur depending on the arrangement (honeycomb and hexagonal), and whether the array was saturated along the [01] (Fig.4.3a,c) or [10] (Fig.4.3b,d) directions.

Fig.4.2 shows MTXM images of the in-plane component of the magnetization in the disk arrays, confirming the simulation's results. The honeycomb array, after saturating along the [01] direction, shows an extended alternating circulation pattern matching simulation (Fig.4.3a,e) since the displacement vector between all neighboring disks is at a 30° angle relative to the saturating field, as seen in Fig.4.2e. When saturated along the [10] direction all disks have two neighbors at a 30° angle relative to the saturating field, and one nearest neighbor disk aligned along the saturating field. This results in magnetic frustration of circulation state coupling and there is a disordered circulation pattern (Fig.4.3b,f).

In the hexagonal array a different behavior is observed due to a change in the number and orientation of neighboring disks. Both saturation directions result in lines of alternating circulation (Fig.4.3c,d) but with the lines being perpendicular (parallel) to the applied field when saturated along the [01] ([10]) direction. For a given disk in the hexagonal array, when saturating along the [01], [10] directions each disk has four neighbors at 30° orientation and two neighbors that are at 90° relative to the applied field for the [01] direction and 0° for the [10] direction. For the four nearest neighbors at 30° it is more favorable energetically to have opposite circulation relative to the central disk and for the the other two nearest neighbors it is more energetically favorable to have the same circulation as the central disk. Therefore, in the hexagonal array, removing the field after saturation results in lines of alternating circulation that are parallel or perpendicular to the applied field.

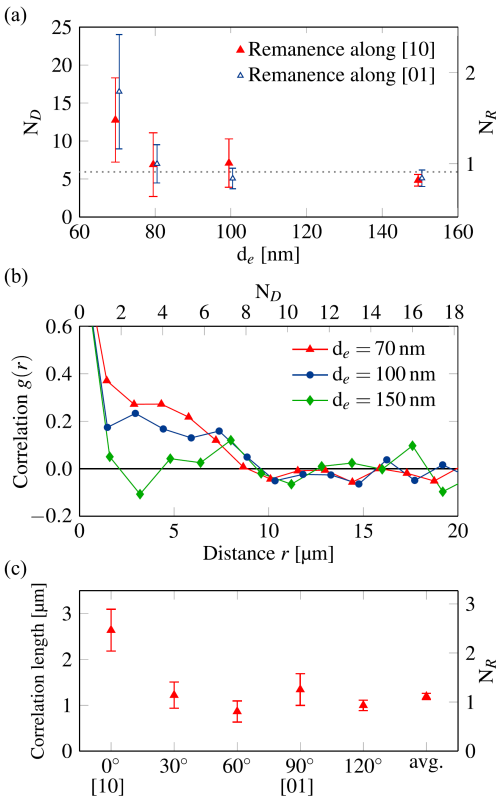

Figure 4.4: (a) In the hexagonal lattice, the average number of disks, N_d in a uniform alternating chiral line domain, the ground state of the lattice as a function of the edge to edge distance. The gray dotted line represents N_d for disks that have random chirality (they are not interacting). (b) Spatial correlation along[10] for different d_e.(c) Derived correlation lengths along different angular directions. Reprinted from [61], with the permission of AIP Publishing.

If all disks nucleate simultaneously there is no coupling between neighboring disks, since chirality is selected as soon as the vortex starts to nucleate(Fig.4.2). It follows that, if all disks nucleate at the *exact* same time, they can't influence each other. In a real system defects in disks and thermal fluctuations can lead to preferred circulations or different vortex nucleation times both of which lead to vortex circulations pattern mismatches. Additionally disks near the edge of a lattice nucleate their vortex state slightly before disks not at the edge.

Simulations shown in Fig.4.3(e-h) match well with the corresponding experimentally measured lattice and saturation direction combination. These simulations do not account for lattice defects or thermal fluctuations, so they have much larger areas of a given uniform

circulation pattern; disks at the edge of the simulated array nucleate first which is the only source for pattern mismatches in this simulation. A simulation with periodic boundary conditions shows random circulation states since all disks nucleate at the same time, indicating that some level of disorder is required to nucleate vortex circulation patterns.

The pattern size can be used to determine the influence of lattice defects and thermal fluctuations competing with the magnetostatic coupling. Varying the inter-disk spacing, d_e allows for variation of the magnetostatic coupling while leaving the thermal fluctuations and lattice defects constant. Fig.4.4a shows a decreasing number of disks, N_d, forming a pattern region with increasing lattice spacing for the hexagonal lattice. At room temperature, only the disks with 70nm edge to edge spacing show patterns that are larger than what would be expected with no circulation coupling (Fig.4.4b). In simulation disks with spacing of up to 250nm show statistically significant coupling. However, in experiment this is not true. The difference between experiment and simulation is likely due to the influence of thermal fluctuations, structural defects in the disks, and structural lattice defects.

The correlation length function (Fig.4.4) g(r) (see Section 2.1) quantitatively measures the coupling between disks as a function of disk spacing. g(r) requires large number of measurements to be statistically significant, so X-PEEM was used to measure the chirality of over 400 disks (Fig.4.5).

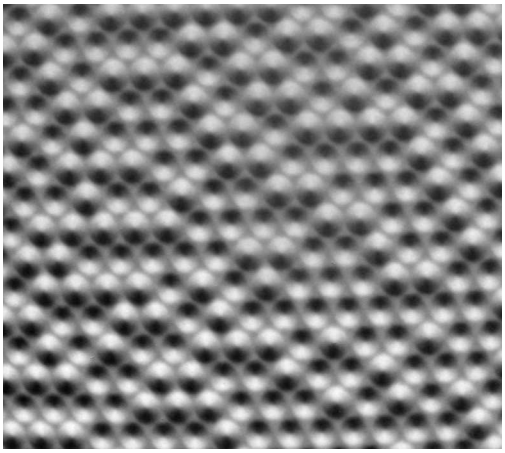

Figure 4.5: XPEEM measurement of coupled 1μm vortex disks with 70nm edge to edge spacing.

In Fig.4.4b, the correlation as a function of edge to edge disk spacing along the [10] axis, after saturating along the [01] axis, is calculated for the hexagonal lattice. The [10] axis is chosen for this calculation because, theoretically, all disks laying along this axis should have the same circulation. The disks with edge to edge spacing of greater then 150nm show no correlations at all and represent the regime where thermal fluctuations at room temperature dominate magnetostatic interactions. For $d_e = 100, 70$nm the disks are positively coupled in agreement with experiment and simulation. A correlation length, defined as the distance where g(r) decreases by a factor of 1/e, along different axes

was calculated and is shown in Fig.4.4c for the lattice with $d_e = 70$nm, initially saturated along [01]. Along all axes the disks are coupled, but most strongly along the [10] axis. The average radius of coherent circulation patterns, N_r given in disk pitch, allows for meaningful comparison between correlation length and the number of disks in a single vortex circulation pattern. Fig.4.4a,c shows that closely packing the disks increases the strength of their magnetic coupling.

The vortex coupling arrays shows that coupling between magnetic nanostructures are influenced by the packing of individual nanomagnetic structures as can be seen in Fig.4.4b. Additionally, the effects of defects from individual structures have a very strong influence on the collective behavior of the nanomagnetic array, since in simulation even the $d_e = 150$nm lattices show strong coupling between disks.

With the coupled vortex disks, the magnetostatic interaction between nanostructures only occurs during saturation and during the initial stage of the vortex phase nucleation (Fig.4.1, 4.2c) as there is only a stray field generated by the small out-of-plane core during remanence.

In order to gain more insight into the collective behavior of structured nanomagnets, and how small structural changes in the lattice and the individual nanostructures effect the overall magnetic properties of the system, a system that interacts via the dipole field in no external field should be studied. Since all collective topological magnetic behavior observed so far has a parameter space that is at least two dimensional, a system with at least a two dimensional parameter space should be considered in order to stabilize collective topological magnetic structures.

4.1.2 XY Macro Spins

Note: Most of the results discussed in this subsection were previously published in the following paper: R. Streubel, ***N. Kent****, S. Dhuey, A. Scholl, S. Kevan, P. Fischer,* Spatial and Temporal Correlations of XY Macro Spins.*, Nano Lett. 18,7428 (2018).*

XY macrospins are nanomagnetic disks with a magnetization that can point in any direction in plane(Fig.2.2b), therefore the parameter space of these disks is two dimensional. Other magnetic systems with the same parameter space restriction have shown collective

topological behavior with the formation of magnetic monopoles and Dirac strings. Since XY spins have an in-plane magnetization, they generate a stray field in the plane the disks are confined to. Isolated disks experience a uniform energy landscape as a function of magnetization direction (Fig.2.2) so they are always super-paramagnetic at finite temperature when isolated.

Isotropic XY spins confined to a plane interacting only through their dipole fields have been theorized to exhibit very different phase transition behavior depending on the structure of the lattice the XY spins are arrayed [77–82]. Systems with square symmetry exhibit a first or second order phase transition from a magnetically interactive stable phase to a disordered fluctuating paramagnetic phase [78, 80]. If there is an intermediate phase with quasi long-range order and vortex formation, this is known as a Berezinskii-Thouless-Kosterlitz-like (BTK-like) phase transition [78] which has topologically non-trivial, $N_{sk-2d} = 1$, vortices. Theoretical predictions for systems with a BTK phase transition include XY macro spins with symmetric exchange and square symmetry [81, 82], XY dipole systems with square symmetry containing defects and no exchange [80], and XY dipole systems with hexagonal symmetry [77–79].

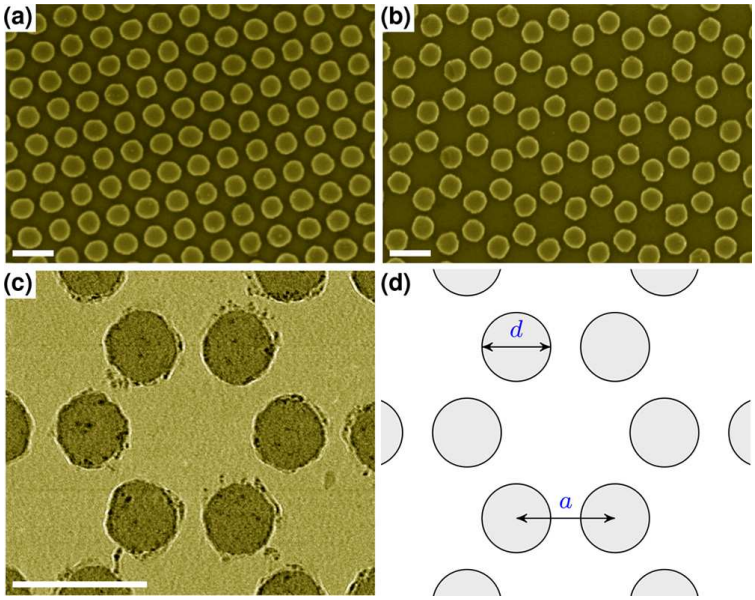

Figure 4.6: SEM images of 100nm diameter, 10nm thick nanodisks in (a) honeycomb and (b) hexagonal arrays. (c) Higher resolution TEM image of the nanodisks, showing good circualirty, with some polymeric residue. This was imaged on a SiN membrane, so lithographic quality is lower and there is more residue compared to arrays on solid Si wafers. (d) Schematic indicating notation used for disk spacing. Scale bars are 200nm. Reprinted with permission from [62]. Copyright 2018 American Chemical Society.

Experimentally studied XY dipole systems include lattices of $FeCl_3$ atoms that are layered between Fe^{3+} ions creating a hexagonal XY-dipole lattice [77] and artificially created XY macrospin systems with square symmetry [83–86]. They reveal excellent agreement between

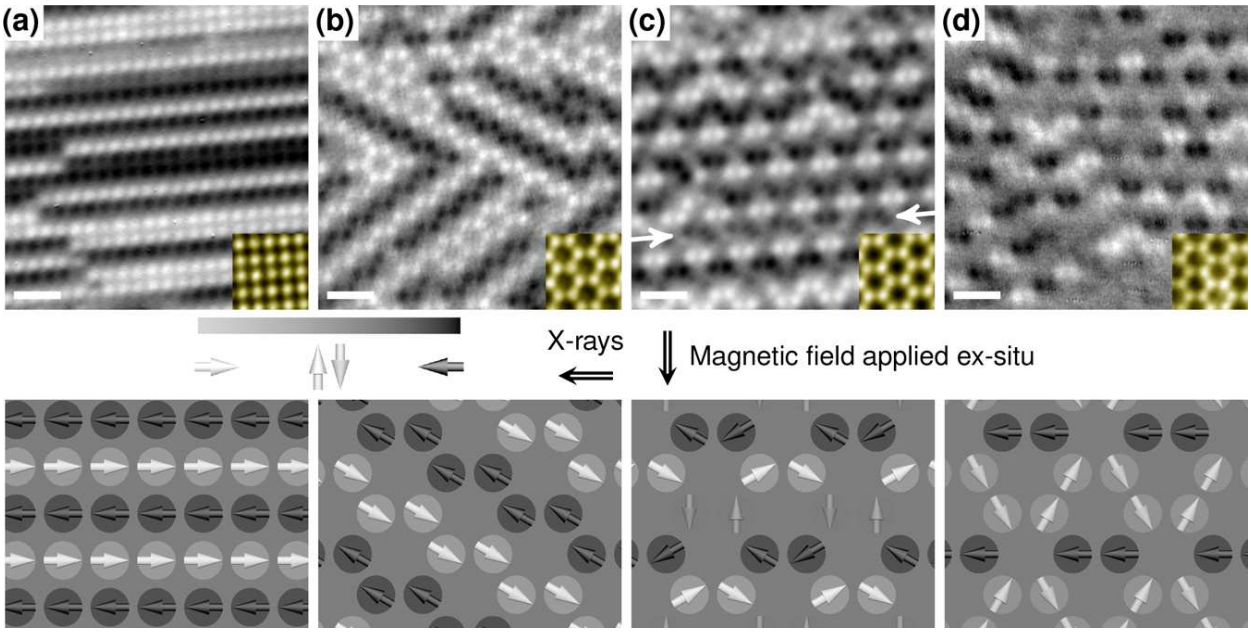

Figure 4.7: Ordering of magnetic XY macro spins in planar nano disk arrays (h = 10 nm; d = 100 nm; a = 150 nm) visualized with XMCD-XPEEM. Each disk behaves as an (isotropic) XY macro spin which is magnetostatically coupled to its neighbors, resembling systems with (a, b) uniaxial (striped) and (c, d) 6-fold symmetry, including two predicted honeycomb ground states: (c) vortices and (d) paired ground state. The white arrows in part c indicate a region possibly in the paired ground state. The images display the remanent states at room temperature after ex-situ saturation along the indicated field direction, e.g., perpendicular to the short edge of the honeycomb lattice. Scale bars are 500nm. Reprinted with permission from [62]. Copyright 2018 American Chemical Society.

theory and experimentally measured integral magnetometry measurements, but no direct microscopic evidence of frustrated, dynamic behavior has been observed in XY macrospins, unlike other XY Ising systems that form spin ice [40, 87, 88] and spin glass [89]. Microscopy shows both of these can host $N_{sk} = 1$ magnetic structures[40, 87–89].

In this section the behavior of XY macro spins is directly studied with magnetic microscopies. The macrospins were arranged in square, honeycomb, and hexagonal lattices, with different lattice spacing at and studied at different temperatures, in order to vary the relative strength of thermal and dipole energies experienced by the macrospins. Depending on the lattice type and spacing the interacting XY macrospins show frustration between multiple ground states, signs of a BTK-like phase transition, and mobile floating vortices with $N_{sk} = 1$. It is also seen that the individual superparamagnetic structures, when arrayed together, *can* collectively have ferromagnetic behavior depending on the lattice type and temperature.

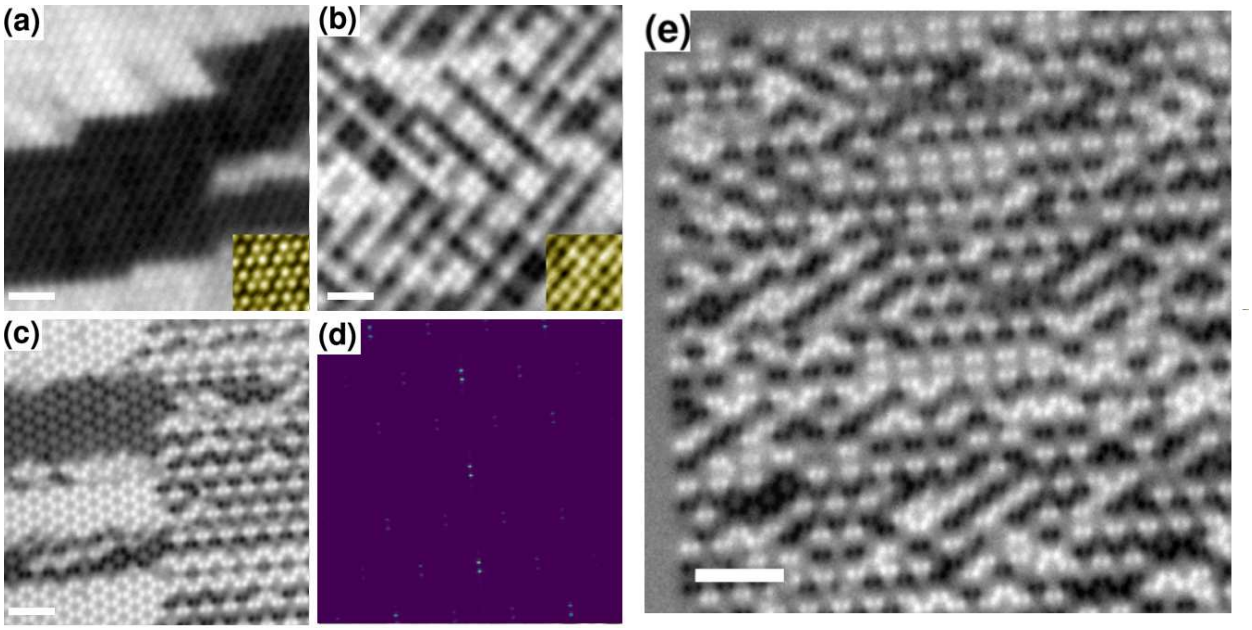

Figure 4.8: PEEM XMCD measurements of disks (a) in a hexagonal lattice showing large in-plane meander domains, similar to that of a film with easy axis anisotropy, (b) disks in a square lattice showing biaxial symmetry, (c) the interface of a mixed state in a honeycomb lattice, and (e) view of a disordered honeycomb lattice. With the exception of (a) all of these states are a result of disorder, or frustration. All scale bars are 500nm. (d) XMCD scattering signal from a honeycomb lattice with meander domains of alternating magnetization.

The XY macro spin arrays were fabricated using EBL on SiO wafers and TEM membranes in nanodisk arrays of dimension 10x10μm and 500x500μm, with lattice constant a = (130-160nm), in square (Fig.4.6a) hexagonal (Fig.4.8a) and honeycomb (Fig.4.6b) arrays. The individual disks were 10nm of Py, with 2nm of Ti on the top and bottom to prevent oxidation, and are 100nm in diameter. These dimensions for Py result in XY macrospins.

Fig.4.8e,c shows the remanent, thermally stable, magnetization configuration recorded after the samples were initially inserted and shows distinct magnetic phases coexisting with each other. The hexagonal array is not expected to have multiple ground states, and at remanence simply has in-plane striped domains, similar to a film with easy axis anisotropy (Fig.4.8a). The square lattice forms alternating macrospin chains predominately oriented perpendicular to the saturation direction (Fig.4.7a) or lattices with biaxial symmetry (Fig.4.8b). Smaller areas of the lattice show macrospin chains aligned parallel to the saturating field.

The ground state of a defect free version of this system would be where the macrospin

chains are aligned perpendicular to the saturating field. Since parallel chains of macrospins are the preferred ground state of this system, it is likely that a small structural defect has created a uniaxial anisotropy axis in one of the macrospins that is parallel to the applied field, influencing its neighbors and creating macrospin chains aligned parallel to the applied field. The square lattice exhibits no thermal fluctuations even at 390K; this is because of the enhanced stability, correlation and anisotropy of square lattices compared to honeycomb lattices [79, 86, 90]. The net remanent magnetization observed in the square lattice (Fig.4.10) is likely due to small structural defects giving disks an anisotropy axis, frustration arising from disks relaxing from saturation at slightly different times, and higher order multipoles terms from finite size of the XY spin disks can also contribute to ferromagnetic order, showing that superparamagnetic nanostructures when arrayed together can be ferromagnetic.

For honeycomb lattices, the remanent magnetization state is a ferromagnetic alternating stripe domain state mixed with vortices of different types (Fig.4.7c) with a smaller remanent magnetization (Fig.4.10a) than what was observed in the square lattice. This is because only in a square lattice do the higher order multipole terms contribute to a net magnetization at zero field; in the honeycomb lattice only structural defects result in a magnetic remanence. If remanence is achieved via cooling from above the Curie temperature, a topologically protected hexagonal magnetic vortex phase is the theoretically predicted ground state (Fig.4.7c, Fig.4.9e). Since XY macrospins are confined to a 2d plane, magnetic vortices are topologically protected structures with a winding number of one (Note that the parameter space is 2d instead of 3d). In experiment both phases are seen to coexist (Fig.4.8c,e) with preference for the stripe phase if the edge to edge spacing of disks is < 50nm, and a preference for the vortex phase if the edge to edge spacing is > 50nm, suggesting that temperature competing with the magnetostatic interaction is the cause for the striped phase. Additionally, disks with a preferred anisotropy axis can nucleate a striped phase locally in other nearby disks, especially when interdisk spacing is < 50nm. There are two intermediate phases, that can be viewed as a combination of the striped phase and the vortex phase. One results in bound vortex pairs of opposite chirality and is similar to the original BTK theory for 2D XY spin systems (Fig.4.7c, Fig.4.9e,f). The other is a slightly larger vortex formed across several pairs of disks, but still forming a flux closure state (Fig.4.7d, Fig.4.9e,f). The ratio between phase coverage of the striped domains and vortices is two to three. XMCD scattering mea-

surements were performed on a few select samples of the 500x500μm arrays, and was able to corroborate what was observed in PEEM (Fig.4.8d) for striped domains in a honeycomb lattice, but was inconclusive with regards to other magnetic structures.

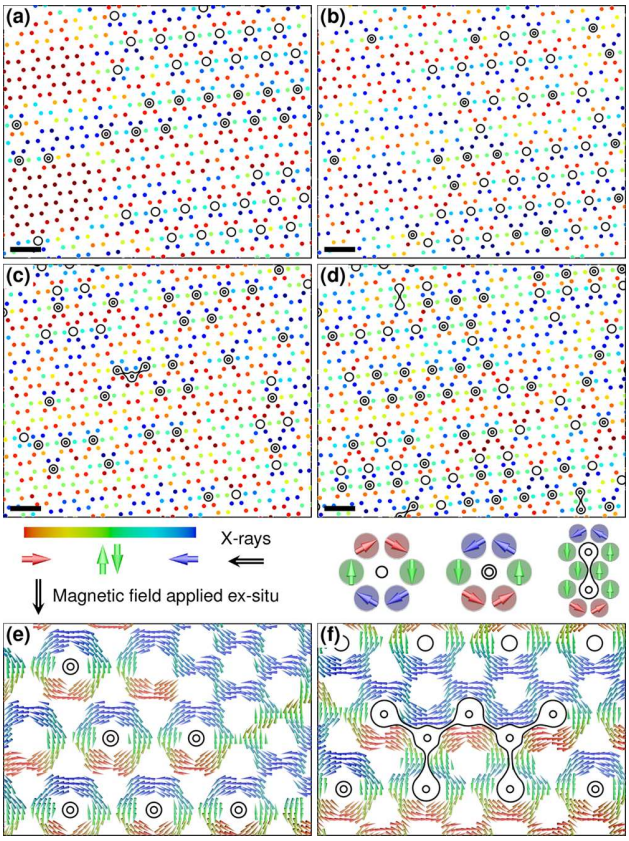

Figure 4.9: Remanent and a thermally partially equilibrated states in honeycomb nano disk arrays at 300k (a),(c) and 390k (b),(d) with a = 150nm (a),(b) and a = 155nm (c),(d). The different types of black circles in (a)-(d) match the vortex types illustrated in the schematic, as well as the results of simulation (e),(f). Reprinted with permission from [62]. Copyright 2018 American Chemical Society.

Comparing remanent states of the honeycomb lattice with (a=150nm, 155nm) at 300k (Fig.4.9a,c) and 390k (Fig. 4.9b,d) show several qualitative differences before and after heating. The initial net magnetization is reduced to zero after heating (Fig.4.10a) implying that the anisotropy energy barrier imposed by structural defects and other disks are more readily overcome to reduce stray field energy at higher temperatures. This magneto-structural change can be seen in the reduced size of uniform stripes from ten lattice spacings to 1-2 lattice spacings (left side of Fig.4.9a,b).

Additionally the vortex phase in both sets of disks moves laterally while maintaining a correlated, somewhat coherent, structure, similar to a skyrmion lattice subjected to a current. This mimics the behavior of spin liquids and implies that this mixed phase is BTK like. More importantly, it shows that in the XY macro spin arrays where the vortex arrays float, there is no structural pinning, implying that structural defects responsible for the remanent magnetization of the honeycomb lattice are non local in nature. This is because a single disk with a defect, a ferromagnetic disk, will impart non-local net magnetization and ferromagnetic order in the closely packed array of XY spin superparamagnets. For a=155nm the vortex phase coverage increases from 39% percent to 59% post thermalization (Fig.4.9c,d,

Fig.4.10b). However, the ratio of the ordered vortex phase to disorder phases (trigonal/ square) decreases from from 11.5 to 5.8 (Fig.4.9c,d). This is likely due to the fact that regions which are turned into vortices after thermalization are either near, or strongly effected by a disk which has a defect; regions which are not in the ground state pre-thermalization are that way because of some defect or disorder.

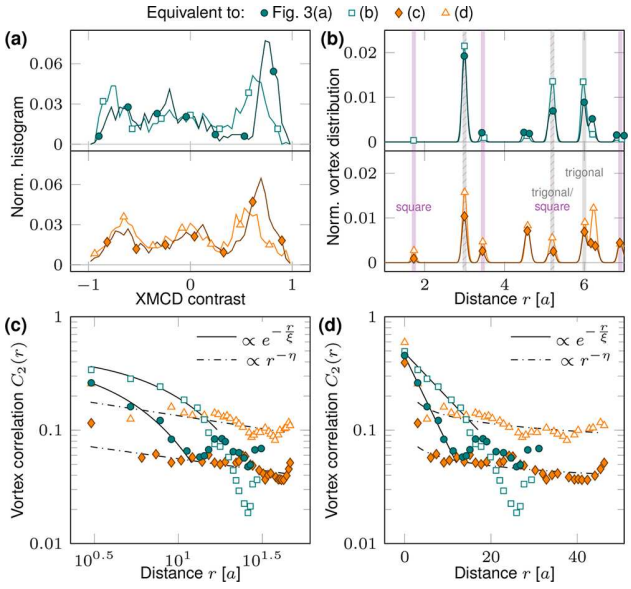

Figure 4.10: (a) XMCD histogram revealing an initial net magnetization in both lattices from Fig.4.9a,c. After heating and allowed time to equilibrate, the net magnetization goes away (Fig.4.9b,d). (b)Percentage of Vortex states in a given vortex type. There is an increase in disordered vortex configurations after thermalization. Vortex correlation function plotted on a (c)log-log scale, and semi-log scale(d). The algebraic decay of the correlation function for a=150nm lattice,$\eta = 0.23, 0.2$, is close to the algebraic decay predicted in a BTK phase transition, $\eta = 0.25$. Reprinted with permission from [62]. Copyright 2018 American Chemical Society.

Micromagnetic simulations, of arrays of 230 nanodisks (d = 100 nm, h = 10 nm, a = 150 nm, mesh size: 5 nm) were carried out at 0 K and reveal a hexagonal vortex phase for the honeycomb lattice, where all vortices have the same chirality.

Calculating a higher order vortex circulation function, similar as to what was seen with the coupled vortices, $C_2(r) = 3\left\langle c_i^2 c_j^2 \right\rangle$, allows one to quantify the long range order of the vortex phase and quantitatively check if the vortex phase is similar to the BTK transition. A BTK phase has a correlation function with an algerbraic decay rather then an exponential one (Fig.4.10). The a=150nm lattice shows a correlation function with algebraic decay with $\eta = 0.2 \pm 0.1$ for room temperature and $\eta = 0.23 \pm 0.1$ for 390K (Fig.4.10c,d). This is within error of the value $\eta = 0.25$ for a BTK transition, implying that the disordered vortex phase is close to being a BTK-like transition.

To study the superparamagnetic- ferromagnetic transition for individual disks in the array, temporally resolved XPEEM experiments with a temporal resolution of (7 ± 0.5)s were performed to investigate local magnetic fluctuations in the samples. Samples with a < 155nm do not show any significant fluctuations even at 390K, and samples with a > 155nm fluctuate

too fast to be resolved by XPEEM.

Observing fluctuations we can calculate the auto correlation function between disks as a function of time: G(t) [62]. If we record no fluctuations over a time period for two disks because they both are fluctuating too fast, and they both have the same average magnetization it is reasonable to say that these disks are correlated. To understand this behavior with topologically non-trivial magnetic structures, thermal fluctuations are observed in a single vortex unit cell of six disks (Fig.4.11), with a = 155nm. The temporal evolution shows periodic switching with a tendency to stay in the vortex phase (Fig.4.11a). G(t) is calculated (Fig.4.11c) for the average magnetization of the top two disks with the average of the bottom two disks (Fig.4.11b). The average magnetization for the top two disks (Fig.4.11b) and G(t) (Fig.4.11c) confirms the semi periodic fluctuations of this vortex state (Fig.4.11c).

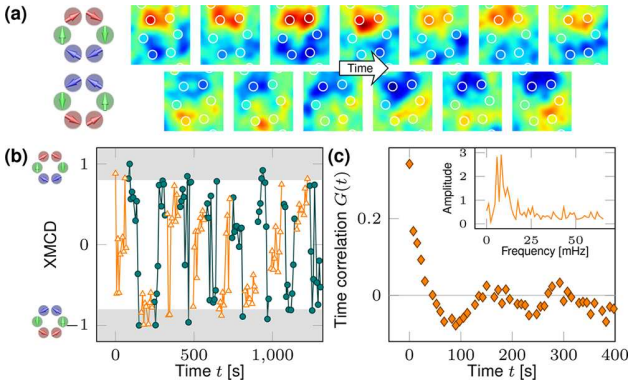

Figure 4.11: (a) Temporal evolution of disks in a correlated vortex state imaged at 390K. (b) Average in-plane magnetization as a function of time, showing the temporally periodic existence of the vortex state (when the magnetization is 0). (c) Temporal correlation function as a function of time, revealing periodic switching of disks relative to each other. Reprinted with permission from [62]. Copyright 2018 American Chemical Society.

It is observed that superparamagnetic XY-spins interacting through their dipole field have an alternating striped ground state if arranged in a square or hexagonal lattice and a hexagonal vortex array, with $N_{sk} = 1$, if arranged in a honeycomb lattice. In experiment the honeycomb lattice has two degenerate ground states in competition with each other: a striped phase generated from structural defects and a vortex phase. This leads to disordered floating vortices which can form bound pairs of opposite chirality and winding number, which is similar to the BTK transition. Reducing the stray field energy, by increasing disk spacing, shows short range topological order by forming vortices with no preferred chirality (vortex chirality is degenerate). Collective topological stability is observed in the floating vortex phase since the topologically non-trivial vortices are stable, even when the constituent nanomagnets are fluctuating.

4.1.3 Ferromagnetic Liquid Droplets

Note: Most of the results discussed in this subsection were previously published in the following paper: X. Liu, ***N. Kent****, A. Ceballos, R. Streubel, Y. Jiang, Y. Chai, P. Kim, J. Forth, F. Hellman, S. Shi, D. Wang, B. Helms, P. Ashby, P. Fischer, T. Russell* Reconfigurable ferromagnetic liquid droplets *, Science 365, 6450 (2019).*

The previous discussion of paramagnetic XY macrospins indicates that long range magnetic order can be established by closely packing superparamagnetic particles. A net magnetic moment can also be imparted to a lattice when an ideally superparamagnetic XY spin has a structural defect, causing it to have an anisotropy axis, becoming ferromagnetic and influencing its neighbors. This implies that ferromagnetic order can be imparted to arrays of superparamagnetic particles if some of the particles are ferromagnetic.

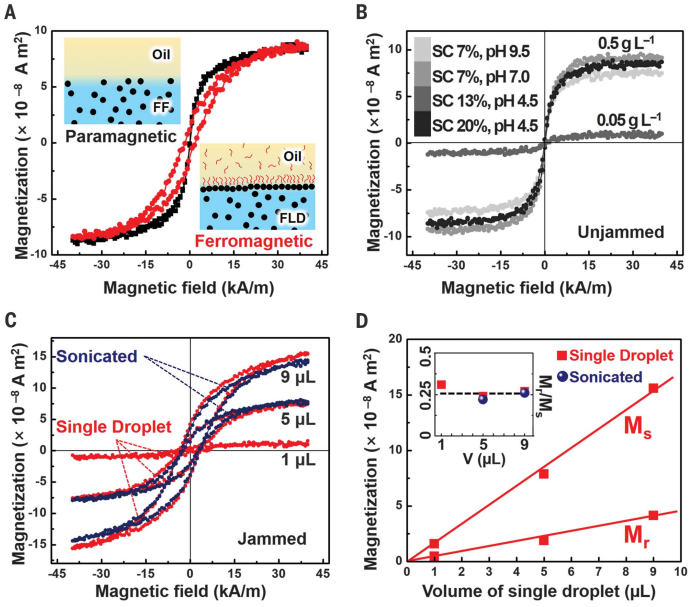

Figure 4.12: (A) VSM measurements of jammed (red line) and unjammed (black line) FLD droplets. The jammed droplets are ferromagnetic. (B) Hysteresis of a droplet with 0.05g/L MNPs and 0.5g/L MNPs droplets in various Ph concentrations showing the surface coverage of MNPs. (C) Hysterisis of jammed droplets of various sizes, showing very similar magnetic properties. (D) M_s, M_r as a function of droplet volume. Both scale linearly with volume, and the ratio M_r/M_s stays constant. From [63]. Reprinted with permission from AAAS.

One of the most interesting superparamagnetic systems is a ferrofluid: dispersions of magnetic nanoparticles (MNP) in a carrier fluid. The individual magnetic nanoparticles are effectively superparamagnetic because they are allowed to rotate freely in the fluid, so even if an individual MNP has a net magnetization, that magnetization can freely rotate in the fluid, even though it is not rotating relative to the particle itself. As a result a ferrofluid is paramagnetic, and has no remanent magnetization [91, 92]. Ferrofluids have found many uses in medicine and technology [93, 94]. However, ferromagnetic materials behave differently than a paramagnet in an external magnetic field;

ferromagnets can be attracted or repelled by a magnetic field while paramagnets can only be attracted to a magnetic field, i.e. they can never be pushed away from a field source. Liquid ferromagnetism on the atomic scale is only possible in exotic systems such as superfluid helium [95]. Given that frozen ferrofluid is ferromagnetic [96], one could envision making a liquid ferromagnet from a ferrofluid with the right control of the structure of individual MNPs that compose a ferrofluid, and how they move relative to each other. Here a method of producing liquid droplets held together by surface tension, that are truly ferromagnetic, with tunable magnetic properties and a controlled ferromagnetic to paramagnetic transition is presented.

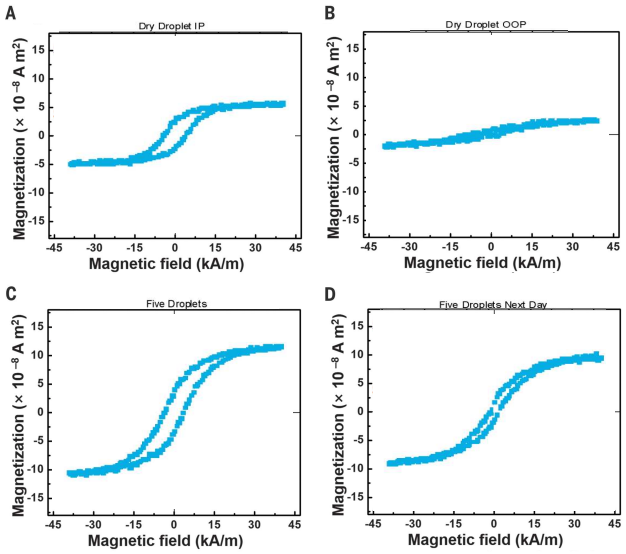

Figure 4.13: In-plane (A) and out-of-plane (B) VSM measurement for a dried 5µL droplet with easy axis shape anisotropy. VSM measurement of five droplets right after being jammed (C) and the same droplets partially unjammed (D) one day later.

MNPs can be ferromagnetic or superparamagnetic depending on their diameter, the ambient temperature, and how closely they are packed. At room temperature Fe_3O_4 nanoparticles transition from superparamagnetic behavior to ferromagnetic behavior between 15-20nm in diameter [28, 97, 98]. Spherical Fe_3O_4 nanoparticles have also been found to have cubic anisotropy or uniaxial anisotropy and to be in a single domain state when below 50nm in diameter [28, 97]. For this study, nanoparticles with an average diameter of 22nm were chosen to be used in the ferromagnetic liquid droplets (FLDs); they are ferromagnetic at room temperature with cubic or uniaxial anisotropy [28]. Ferromagnetism of the individual stable MNPs was confirmed by affixing them to a substrate, measuring their hysteresis via VSM, and observing a non-vanishing coercivity and remanent magnetization (Fig.4.13a). When the MNPs are affixed to a substrate, the shape anisotropy of the MNPs creates a collective in-plane easy axis anisotropy (Fig.4.13a,b). It is essential that the MNPs are ferromagnetic at room temperature when affixed to a solid substrate, because if the physically fixed nanopar-

ticles are innately (super)paramagnetic, freezing them while they are in liquid does would not impart ferromagnetism to the liquid as a whole [96].

Previous work has jammed silicon oxide nanoparticles particles together in liquid to build structured fluids [99], while closely packing the nanoparticles. In order to arrest some of the motion of the MNPs in a ferrofluid, the 22-nm-diameter MNPs ($Fe_3O_4 - CO_2H$) were immersed in a solution of amine-modified polyhedral oligomeric silsesquioxane ($POSS - NH_2$) in toluene. $POSS - NH_2$ binds with the MNPs turning them into MNP-surfactants. With only small amounts of MNP surfactants, the MNPs are free to enter and leave the interface forming paramagnetic ferrofluid droplets confirmed via VSM (Fig.4.12b). Adding larger amounts of $POSS - NH_2$ ligands results in a higher concentrations of MNP-surfactants until they are compressed and jam, locking them physically so they are no longer free to rotate. This effectively [100, 101] changes some of the MNPs from superparamagnetic to ferromagnetic, confirmed via VSM (Fig.4.12a,c). Comparing magnetic hysteresis for ferrofluid liquid droplets (FLD) versus a ferrofluid droplet with an identical size and concentration of MNPs (Fig.4.12) show an identical M_s, which is to be expected since it should only be proportional to the total number of MNPs, but the FLD has a non zero M_r of $1.89 \cdot 10^{-8} A \cdot m^2$ with a finite coercivity (H_c) of $7.2 kAm^{-1}$ showing it is ferromagnetic. Droplets of different sizes show almost identical magnetic properties, except for a M_s, M_r that is dependent on the total volume of magnetic material, see Fig.4.12b,c,d. The droplets show no shape anisotropy; the magnetic hysteresis curve looks identical regardless of droplet orientation in the VSM. Additionally, the uniquely ferromagnetic behavior of being attracted and repelled by different magnetic field sources is observed.

FLDs still retain their liquid properties and can be reshaped using magnetic fields and glass capillaries, (Fig.4.14a) and the resultant droplet's final aspect ratio is a function of droplet volume, and capillary diameter (Fig.4.14b). Changing the pH from 4.5 to 9 allows the MNP to un-jam (Fig.4.14c) resulting in a paramagnetic droplet again. Droplets with a ferrofluid core, and a jammed shell of nonmagnetic sodium carboxymethyl cellulose, are also paramagnetic, showing that the jamming of the MNPs is responsible for the droplet being ferromagnetic. Several jammed, ferromagnetic droplets were left out overnight, becoming partially unjammed, and were measured again. The smaller droplets became paramagnetic, while the larger collections of droplets have a large reduction in remanence magnetization

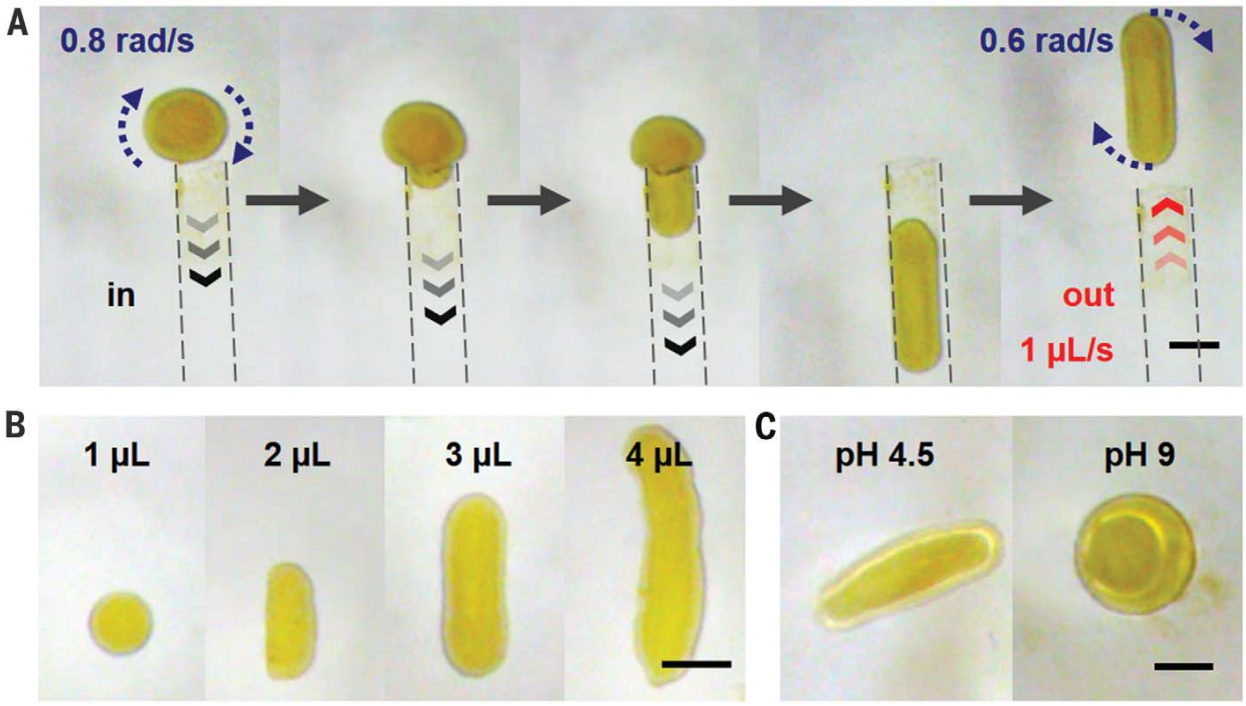

Figure 4.14: (A) FLDs can be reshaped using glass capillaries. (B) The dimensions of the resultant droplet are a function of the capillary diameter and droplet volume. (C) The droplet can transition from a ferromagnetic jammed state (left) to an unjammed paramagnetic state (right). All scale bars are 1mm. From [63]. Reprinted with permission from AAAS.

(Fig.4.13c,d) suggesting that there is degradation of the mechanism that induces ferromagnetism in the FLDs.

Freezing ferrofluids also arrests the physical rotations of the MNPs inducing ferromagnetism, and this has been shown in experiment [96]. Our systems can be thought of as a hybrid between ferrofluid and frozen ferrofluid. There is a thin layer of MNPs particles "frozen" by being jammed at the edge, these particles are no longer free to rotate and hence have a finite coercivity. Since the entire droplets appears to be ferromagnetic, there seems to be a strong coupling between the frozen edge state and the purely liquid inner core.

Since the the frozen edge state is an interfacial effect, droplets of various sizes were studied in order to see the effect of the surface to volume ratio (S/V) by measuring their hysteresis loops. Sonicating large droplets into an emulsion of smaller droplets increases the S/V ratio by two orders of magnitude (Fig.4.12d). As expected M_s and M_r scale linearly with the total volume (total number of MNPs) and H_c remains constant. Surprisingly, despite the jammed

MNPs being an interfacial effect, M_r/M_s remains constant, implying that there is a strong enough coupling between the core and surface states to effectively turn the droplet core into a ferromagnet, independent of droplet size. This origin of this strong coupling effect is not fully understood.

It is possible to see if FLDs have a weaker induced ferromagnetic coupling than other fixed assemblies of similar nanoparticles by comparing the M_r/M_s ratio. For a collection of randomly oriented single domain non-interacting MNP with uniaxial or cubic anisotropy M_r/M_s= 0.5 [102]. If $M_r/M_s > 0.5$ there are additional ferromagnetic interactions between particles and if $M_r/M_s < 0.5$ there are additional interactions between particles that energetically prefer anti-parallel alignment of magnetic moments. In both frozen ferrofluid, and for fixed assemblies of Fe3O4 nanoparticles Mr/Ms is between 0.2 and 0.25 [28, 97, 98, 102]. The M_r/M_s of FLDs is 0.25 independent of droplet volume and is in good agreement with the other similar systems. The interaction that reduces M_r/M_s from 0.5 is simply long range stray field energy reduction, and is what results in domain formation in solid ferromagnets as well as fixed nanoparticle assemblies [103], and XY macrospins. It is surprising how close the value of M_s/M_r for FLDs match that of a fixed assembly of nanoparticles and frozen ferrofluids; one would expect a lower value of M_r/M_s due to the fact that some rotation of the MNPs should still be possible. The fact that so many magnetic properties are in agreement with a fixed assembly of nanoparticles implies that the jammed surface state behaves like a fixed assembly and the paramagnetic liquid bulk mimics the behavior of the surface state. This is additionally supported by the fact that changing the S/V ratio of FLDs does not change their magnetic properties.

4.2 Magnetic Structures in Thin Multilayers

The previous section discussed magnetic structures induced by stray fields, now the magnetic structures will be affected by the interfaces in multilayers. Magnetic thin films and the nanomagnetic energies that stabilize topologically nontrivial spin textures are discussed.

The thickness of a thin film is on the nanometer, or Ångstrom scale leading to an in-plane shape anisotropy. PMA is induced in thin films by creating multilayers with magnetic materials and materials with spin orbit coupling. Since this PMA is an interfacial effect the

thickness of the film does not change the interfacially induced PMA, however increasing the thickness does increase the in-plane anisotropy. This means that the PMA can be tuned in these films by adjusting film thickness. Since M_s scales with the number of magnetic moments, i.e. size/volume of the magnetic material, M_s can be tuned by varying either the thickness of the individual layers or the number of repeats in a stack of multilayers.

Although not absolutely necessary, tuning the DMI is an established way to stabilize skyrmions and other topological spin textures. DMI prefers, from an energetic point of view, that spins have a preferred rotational sense, i.e. non-collinear magnetic structures. However, DMI requires broken inversion symmetry which is why asymmetric multilayers can have a large DMI depending on the thickness and elemental composition of materials used in the multilayers.

4.2.1 Skyrmions in Fe/Gd Multilayer Heterostructures

Note: Most of the results discussed in this subsection were previously published in the following paper: S. A. Montoya, S. Couture, J. J. Chess, J. C. T. Lee, ***N. Kent****, D. Henze, S. K. Sinha, M.-Y. Im, S. D. Kevan, P. Fischer, B. J. McMorran, V. Lomakin, S. Roy, and E. E. Fullerton* Tailoring magnetic energies to form dipole skyrmions and skyrmion lattices *Phys. Rev. B. 95, 024415 (2017).*

Skyrmions are readily stabilized in systems with DMI and broken inversion symmetry [104] because the DMI generates a preferred canting angle between adjacent spins, reducing the energy cost of non-collinear magnetic structures and making skyrmions of a preferred chirality more stable. Dipole fields can generate generate topologically equivalent chiral magnetic bubbles stabilized by symmetric exchange and PMA, without DMI. Due to the similarities between DMI stabilized skyrmions, and chiral magnetic bubbles, it is common to refer to these as dipole skyrmions [104–107]. Achiral magnetic bubbles can also be stabilized in these materials, but do not have a topological charge.

The formation of dipole stabilized skyrmions and skyrmion lattices in amorphous Fe/Gd multilayers as a function of total thickness, individual multilayer thickness, alloy composition, and temperature was studied in order to understand the magnetic energies that stabilize dipole skyrmions.

Fe/Gd was chosen since there is a weak ferrimagnetic coupling between the two layers, allowing for a tunable M_S, and the Gd/Fe interface induces a PMA in both materials, allowing for a tunable anisotropy. In Figure 4.15 the real space magnetic domain structure of a [Fe 0.34nm/ Gd 0.4nm]x80 multilayer (total thickness 53.6 nm) imaged by LTEM is shown. At zero field the film is in a striped domain phase with a periodicity of approximately 124nm (Fig 4.15a,b,c).

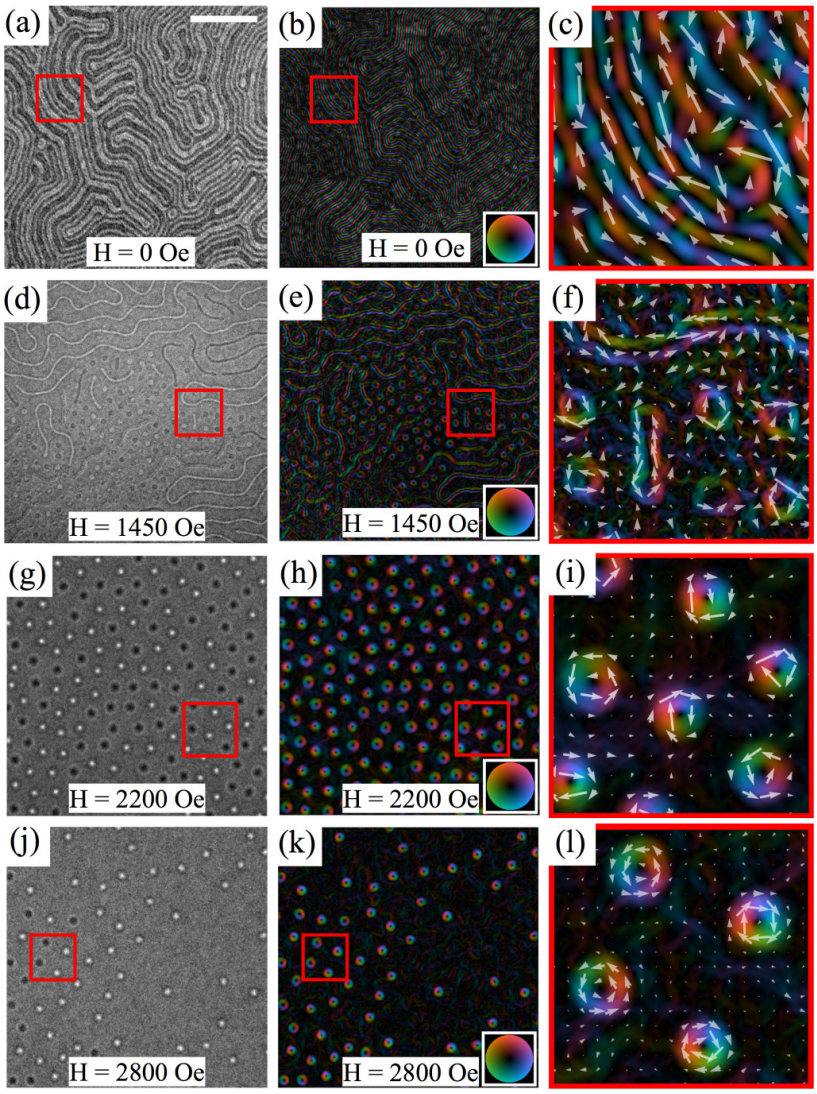

Figure 4.15: (Left column)[Fe (0.34 nm)/Gd (0.4 nm)]x80 imaged at different fields in under focused LTEM images. The middle column is the reconstructed induction map of the left column, and the right column is a zoomed-in induction map as highlighted in the middle column. As the external field is increased (a) Stripe domains transition into (d) a mixed skyrmion stripe phase to (g) a skyrmion lattice to (j) isolated skyrmions. Reprinted figure with permission from [64]. Copyright 2017 by the American Physical Society.

Domain walls imaged in underfocused LTEM show Bloch walls, with no preferred chirality, as expected in relatively thick, symmetric films. It is worth noting there may be Néel caps, as observed in other FeGd films [108], but this would not be observed in LTEM as the in-plane components of the Néel caps at the top and the bottom of the film are opposite and would cancel.

As an in-situ out-of-plane magnetic field is applied, the amount of magnetization, size of domains, parallel to the applied field increases, until some stripe domains collapse into individual bubble domains at approximately 1450 Oe, leaving a mixed phase between dipole

skyrmions and stripes (Fig 4.15d-f).

LTEM induction maps shows a constant chirality around these individual domains (Fig.4.15e,f), confirming these are dipole skyrmions with a winding number of 1. It can also be seen there is no uniform chirality for the dipole skyrmions, as would be expected of DMI stabilized skyrmions, with a (counter)clockwise in-plane wrapping having (negative) positive helicity.

The skyrmions have an average diameter of 71nm which doesn't change noticeably as the field is swept, only rapidly nucleating or collapsing during annihilation or creation. As the field is further increased all of the stripe domains convert to skyrmions in a weakly correlated hexagonal lattice (Fig.4.15g-i) with an equal distribution of chirality. This skyrmion lattice is stable from 1700 to 2400 Oe at which point the topological protection of the dipole skyrmions are overcome, and individual bubbles start to collapse (Fig.4.15j-l) leaving individual skyrmions (Fig.4.15j-k) until a high enough field saturates the sample uniformly.

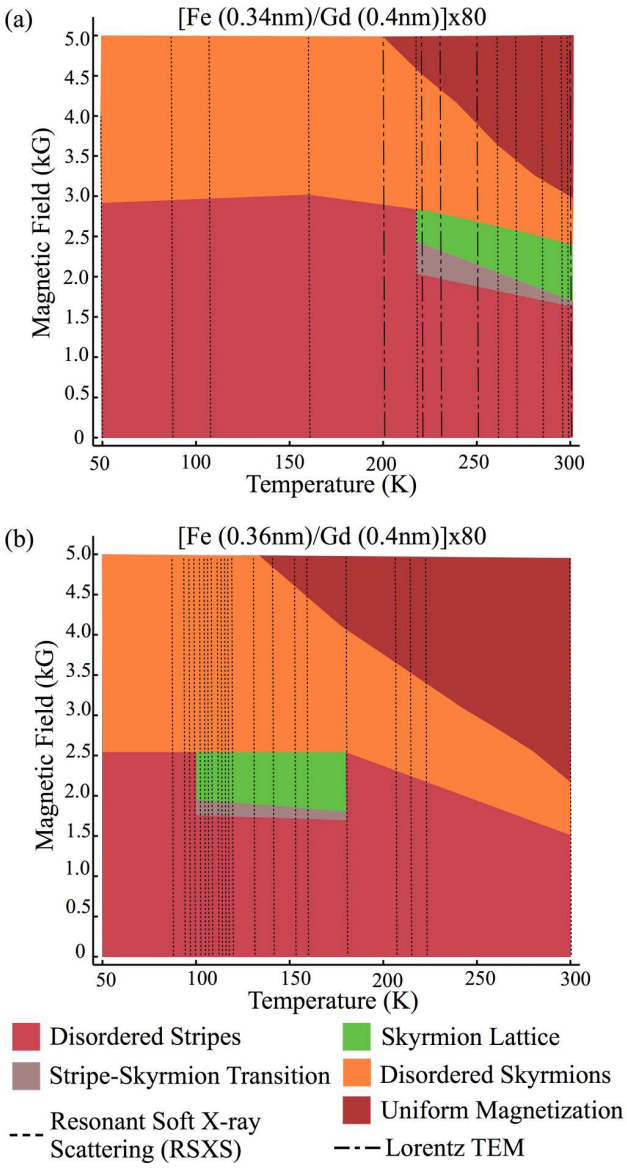

Figure 4.16: Magnetic domain phase as a function of temperature and external field for two different Fe/Gd multilayers. Reprinted figure with permission from [64]. Copyright 2017 by the American Physical Society.

This [Fe 0.34nm/ Gd 0.4nm]x80 sample and an additional [Fe 0.36nm/ Gd 0.4nm]x80 have their magnetic phase space probed as a function of temperature and applied magnetic field in both LTEM and XMCD scattering (Fig.4.16). The five distinct magnetic phases can all be seen in Fig.4.15 except for the uniformly magnetized state. Measurements taken

in LTEM and XMCD scattering corroborate each other, however XMCD scattering measurements are quicker so more data was obtained via this technique. Both samples have a temperature range for which there is a transition from disordered stripes, to a mixed skyrmion/stripe phase, to a skyrmion crystal as a function of increasing magnetic field. However, the temperature range at which these skyrmion crystals are able to be stabilized is different. This is most likely due to the a coupling between the Fe and Gd layers resulting in this material being semi-ferrimagnetic. As a result M_s can be varied as a function of temperature (Fig.4.18a).

In order to quantify this behavior, magnetic hysteresis loops of the sample were taken measuring the perpendicular anisotropy field of the sample, H_k, and M_s. K_u, and the effective magnetization M_{eff}, can be found by using $H_k = 2 \cdot K_u/M_s$ and for thin films $M_s - H_k \frac{1}{4\pi} = M_{eff}$. For thin films $K_u^{eff} = K_u - \frac{1}{2}\mu_0 M_s^2$ [109]. Measurements indicate that $K_u > 0$ (Fig4.18b) for all temperatures, however the shape anisotropy field, $K_d = \frac{1}{2\mu_0} M_s^2$ is greater than K_u so the effective anisotropy is in plane. As the temperature is reduced both, the in-plane anisotropy field increases and K_u decreases, making the films more in plane, similar to other films like this in the literature [110, 111].

For such films there is a critical thickness for the onset of weak stripe domains [109, 112–115] which scales with $M_s^2/K_u^{3/2}$, so it is reasonable to think that the skyrmion lattice phase transition might be proportional to this, which is why this quantity is plotted versus temperature in Fig.4.18d. Of all the plotted quantities, this is the only value, for which when the same in both films, both films will be in a skyrmion lattice phase.

Changing the total thickness of the multilayers allows variation of the magnetostatic energy, while keeping interfacial and internal magnetic energies constant. [Fe 0.34nm/ Gd 0.41nm]xN multilayers with 40, 80, and 120 repetitions had their domain patter imaged in MTXM while sweeping the out-of-plane magnetic field (Fig.4.17). For N=40 hysteresis measurements reveal an easy plane anisotropy. Given the weak PMA induced by the interface of Fe and Gd [116], it is clear that for thinner films the shape anisotropy, K_d overwhelms the interfacially induced uniaxial PMA, K_u.

The N = 80 sample is in a striped phase at zero field (Fig.4.17a) and as the field is increased striped domains pinch off into bubble domains (Fig.4.17b,c), until a weakly correlated bubble lattice is formed (Fig.4.17d). Unlike other samples, at higher fields only the

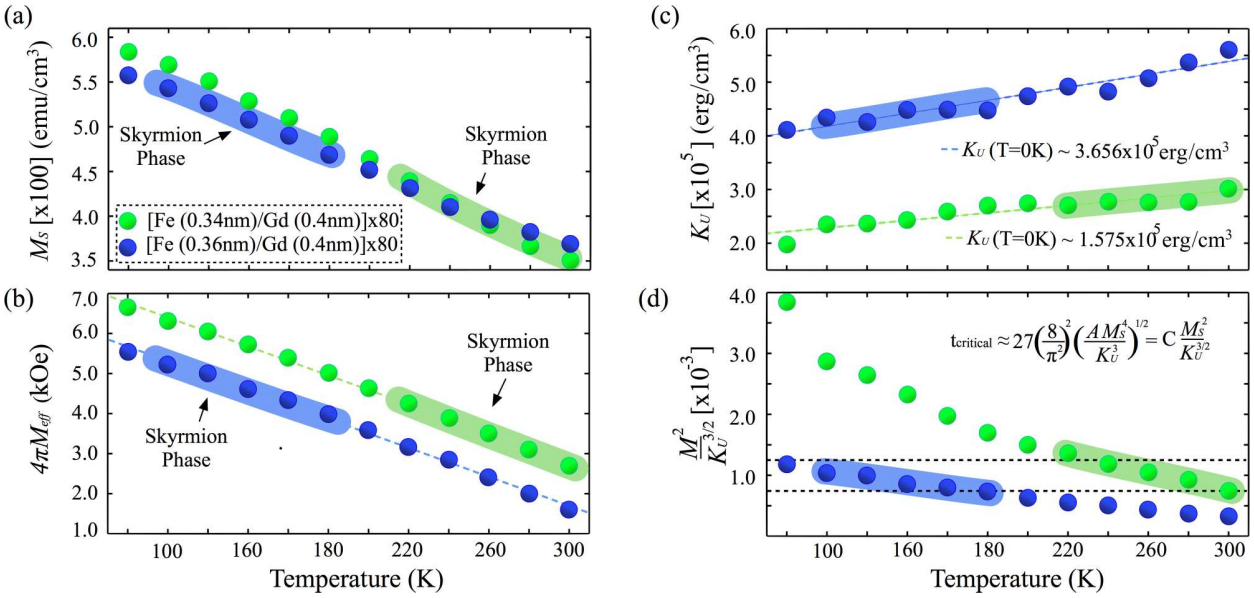

Figure 4.18: Magnetic properties of two Fe/Gd films plotted as a function of temperature. The temperature region where a skyrmion lattice phase can be stabilized is highlighted in each chart. Only for the values of (d) $M^2/K_u^{3/2}$, a parameter known for scaling with phase transitions thicknesses in thin films, are both films able to stabilize a skyrmion lattice phase at the same time, as highlighted by the dashed lines. Reprinted figure with permission from [64]. Copyright 2017 by the American Physical Society.

bubble like structures that were stabilized at 650 Oe (Fig.4.17c), not 750 Oe (Fig.4.17d) are still existent at 1000 Oe. This is different from other samples, where there is no correlation between when the bubble structures form and when they collapse. It is postulated that the bubbles formed at 650 Oe are dipole skyrmions with topological protection that stabilizes them at higher fields relative to achiral bubble domains, which are formed at 750 Oe.

The thicker sample, N=120, starts off showing a large number of dumbbell domains (Fig.4.17g), increasing the field shows a similar progression as the first two films until a skyrmion lattice is formed at 1000 Oe (Fig.4.17j). Increasing the field to 2500 Oe shows no noticeable change in the lattice or the skyrmion size of 70nm. It has been seen previously that dipolar skyrmion crystals are only stabilized for a certain combination of the anisotropy field and M_s, postulated to be $M_s^2/K_u^{3/2}$ (Fig.4.18d). Since the skyrmion crystal phase is stable for a range of $M_s^2/K_u^{3/2}$, and the skyrmion crystal phase appears at different fields for different repeats, increasing the thickness from 40-80-120 increases the PMA and M_s in unequal ratios.

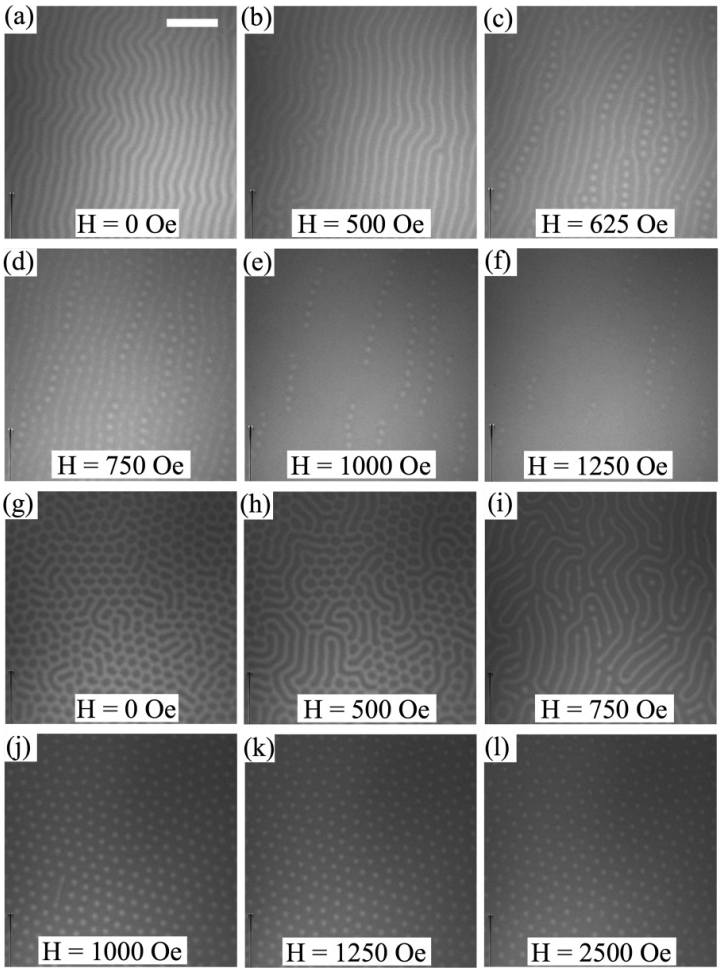

Figure 4.17: Real space MTXM images of (a-f) [Fe (0.34 nm)/Gd (0.41 nm)] x 80 and [Fe (0.34 nm)/Gd (0.41 nm)] x 120 as a function of external out-of-plane field. Reprinted figure with permission from [64]. Copyright 2017 by the American Physical Society.

It has been seen here Fe/Gd multilayers can stabilize dipole skyrmion crystals without any DMI. The properties of the Fe/Gd multilayers can be varied by changing the individual layer thickness, or total thickness of the multilayers demonstrating that thin film multilayers can be tailored in a variety of ways to stabilize topologically nontrivial spin textures.

4.2.2 Chiral Ferrimagnets

Note: Most of the results discussed in this subsection were previously published in the following paper: R. Streubel, C.-H. Lambert, ***N. Kent****, P. Ercius, A. T. N'Diaye, C. Ophus, S. Salahuddin, P. Fischer* Experimental Evidence of Chiral Ferrimagnetism in Amorphous GdCo Films *, Adv. Mater., 30, 1800199 (2018).*

The Fe/Gd multilayers are ferrimagnetic multi-layers that host topologically nontrivial textures without DMI. It is a natural to ask whether it possible to impart DMI to ferrimagnetic materials and what is the effect on the ferrimagnetic sublattices. It has been shown that large DMI, necessitating inversion symmetry breaking can be induced either one of two ways: chiral crystals [117], or antisymmetric multilayers[118]. The theoretically pre-

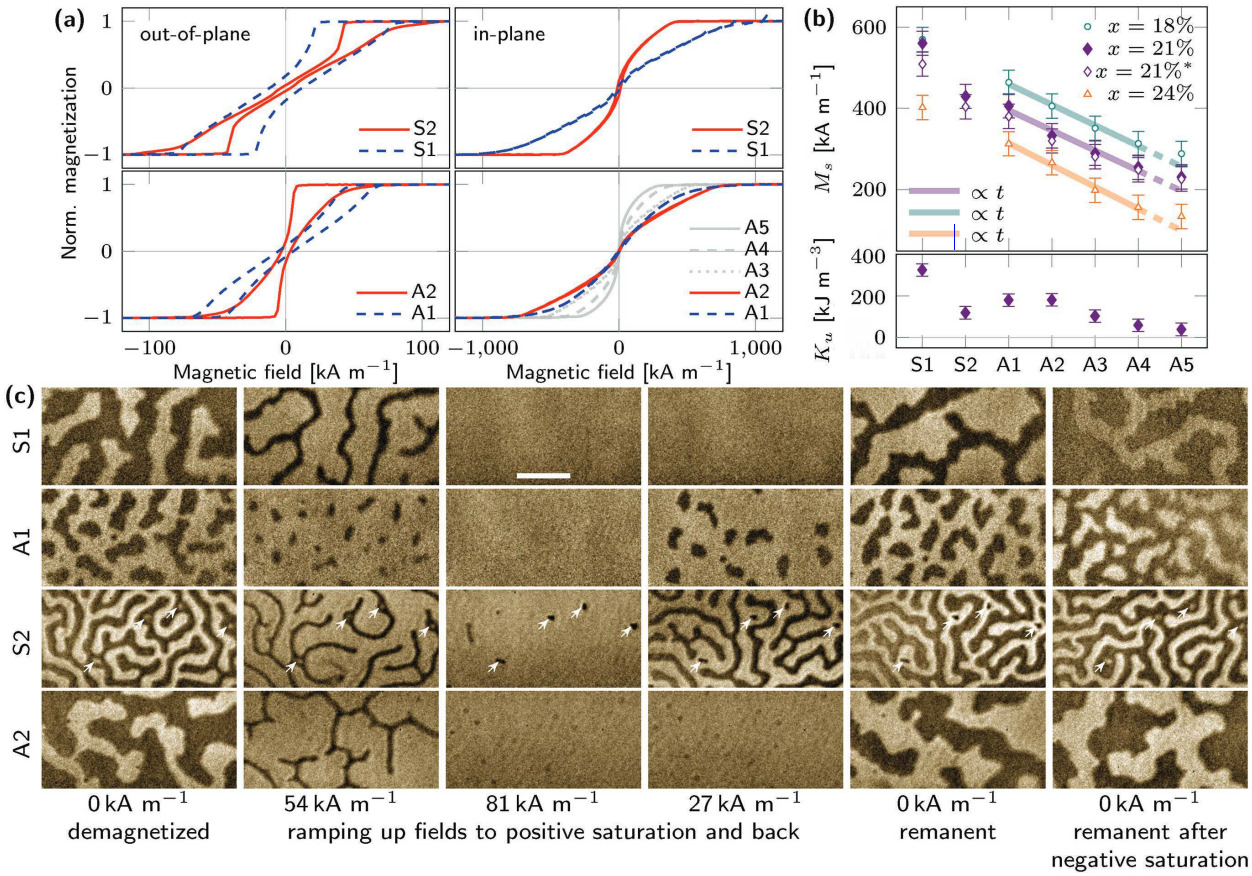

Figure 4.19: (a) VSM measurements of films with varied GdCo thickness. (b) M_s, K_u as a function of GdCo thickness for films with different percentages of Gd. (c) MTXM images at the Co L_3 edge of various GdCo multilayers at different external fields. White arrows in S2 highlight regions with a high Gd composition. Reproduced with permission from [65].

dicted chiral ferrimagnetic crystals are only magnetic near absolute zero and non metallic compounds.

Antisymmetric multilayers show that a large additive DMI can be generated by fabricating a ferromagnetic metal between two heavy metals with opposite signs of DMI, notably with Pt/Co/Ir multilayers showing the first room temperature zero field skyrmions [119]. In order to take advantage of this ferrimagnetic layers of GdCo were sandwiched between heavy metals forming symmetric Pt/GdCo/Pt multilayers and anti-symmetric Ir/GdCo/Pt multilayers. Quantitative electron yield XMCD, MTXM, and LTEM, reveal chiral ferrimagnetism in the asymmetric multilayers with room temperature zero field skyrmions, while the

symmetric ones are achiral.

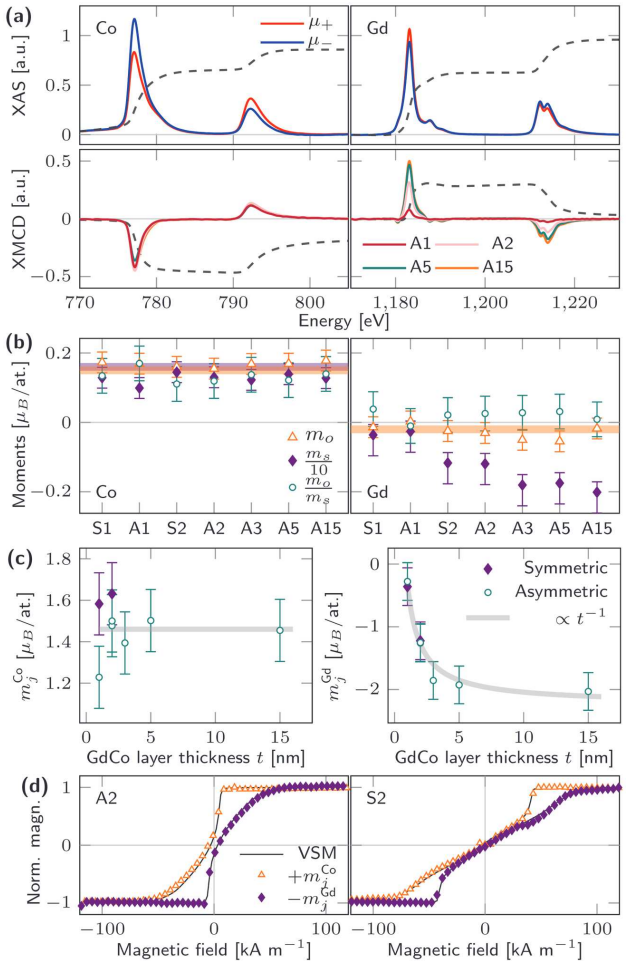

Figure 4.20: (a)XAS and XMCD signal of the Co $L_{3,2}$ and Gd $M_{5,4}$ edge. (b) Calculated orbital and spin moments, compared to their literature values (solid lines). (c) M_s as a function of GdCo layer thickness. (d) Element specific hystersis looops showing ferrimagnetism. Reproduced with permission from [65].

Several ferrimagnetic multilayers were prepared by dc magnetron co-sputtering of GdCo between Ir and Pt (Fig.4.20). The GdCo thickness ranging from 1 to 5nm and the Ir/ Pt layers were either 1nm or 2nm thick, as any more thickness does not change the DMI in Co since it is an interfacial effect. The samples are denoted as SX or AX, for symmetric and asymmteric, where X is the thickness of the GdCo layer [118]. The Gd percentage was x=(18-24) so that out-of-plane magnetic domains, with Fe holding the majority magnetization, would form. A 15nm GdCo layer was used as a reference sample to understand the bulk properties of GdCo with no interfacial effects.

The hysteretic behavior of these ferrimagnetic multilayers was measured using MTXM and VSM. SX has a higher effective PMA than AX as can be seen by noting that in-plane saturating field, H_k, for a given SX compared to AX is higher (Fig.4.19a). This makes sense as Pt induces a larger interfacial PMA than Ir in Co, and is also the reason for the higher M_s in the symmetric samples. as well for the linearly decreasing M_s as the thickness of the GdCo layer is increased (Fig.4.19b). All samples, AX and SX, show a decrease in PMA as the thickness of the GdCo is increased (Fig.4.19a), this is to be expected as the PMA is an interfacially induced effect competing with the in-plane shape anisotropy of the thin film. Several sample were measured in MTXM at the Fe L_3 edge, showing a similar domain pattern to other ferromagnetic films with PMA

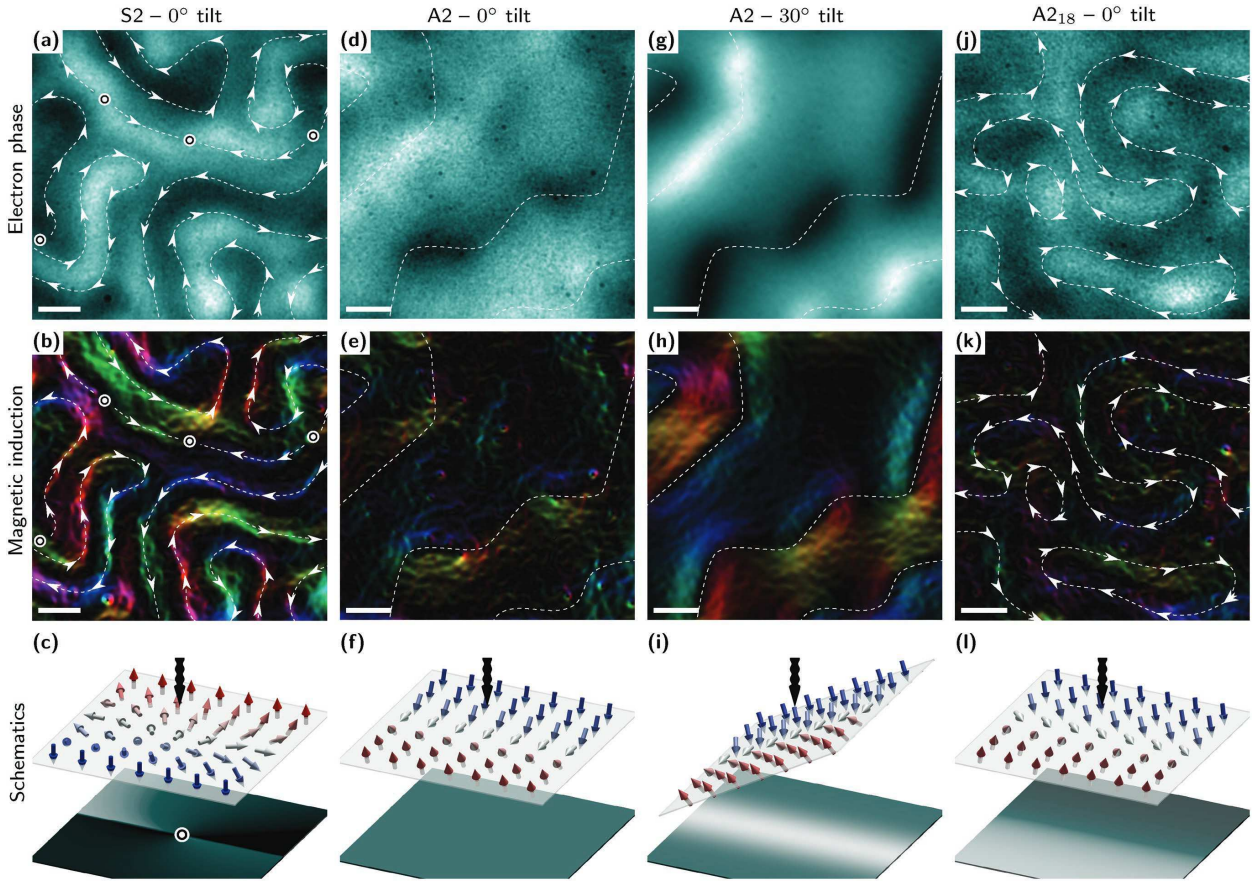

Figure 4.21: (a,d,g,j) Electron phase, (b,e,h,k), reconstructed magnetic induction map of S2 and A2 at various angles of electron incidence. Simulated phase of a (c) Bloch line, (f) Néel wall, (i) tilted Néel wall, and a (l) hybrid Néel -Bloch wall. Reproduced with permission from [65].

and DMI (Fig.4.19c). Individual room temperature zero field ferrimagnetic skyrmions can be seen in A1 when demagnetized and in both remanent states. In S2 we are able to see several areas where there is a higher concentration of Gd, so Fe no longer holds the majority spin state. This is confirmed at saturation when the white spots noted at lower fields flip to black; the majority spin state is aligned with the saturating field, which means that since Fe is anti aligned with the majority magnetization at the highlighted locations, Gd has the majority magnetization.

Elemental specific quantitative XMCD was performed to disentangle the behavior of the two magnetic elements in the GdCo layer. The dichroic absorption spectrum was collected for the Co $L_{3,2}$ edge from750-850 eV, and the Gd $M_{5,4}$ edge 1150-1255 eV (Fig.4.19a),

by saturating the samples out of plane with a ±200kA/m field. From this, the XMCD spectrum was calculated and the sum rules for the appropriate XMCD edge [53, 120] are used to calculate the orbital and spin moments of Gd and Co. The measured spin, and orbital moment of Co are within error of the bulk values, (Fig.4.20b,c). The Pt induces PMA in the Co more strongly than Ir, with a ratio of M_s between the 1, 2nm thick GdCo symmetric and antisymmetric stack is 1.3 ± 0.1 and 1.1 ± 0.1 respectively, and matches very well with the same ratio of saturation magnetizations measured in VSM, (Fig.4.20). Interestingly, the Gd spin moments deviates from it's bulk values (Fig.4.20b). This is independent of orbital moment and capping, but shows a t^{-1} dependence on GdCo layer thickness (Fig.4.20c). It has been shown, that ferromagnetic coupling can be mediated between Co and Gd through Pt, so there is a symmetric exchange between Gd and Pt in *other* layers of the multilayer. This competing exchange mechanism introduced at the interface forces the spin moment of Gd to no longer be out of plane. Elemental specific hystersis loops show good anti correlations between the Co and Gd magnetization's (when it can be measured) in Fig.4.20d as expected of a ferrimagnet.

Since skyrmions and other topological magnetic structures require a constant chirality, in order to determine if there is a constant chirality in the ferrimagnetic films LTEM imaging was performed (Fig.4.21). In the symmetric sample, S2, achiral Bloch walls can be seen. It is usually difficult to determine chirality in LTEM since only the in-plane induction is measured and chirality is determined by how the magnetization rotates from out of plane to in plane. However, locations where the chirality of the domain walls change are accompanied by two Bloch lines, which allows for identification of domain walls that change chirality. If we can identify double Bloch lines then the materials which hosts them is achiral. In the symmetric stack (Fig.4.21a,b), S2, multiple double Bloch lines are identified (Fig.4.21b,c), confirming a lack of a preferred chirality and no DMI. In A2, a very weak magnetic contrast is observed in normal incidence (Fig.4.21d,f), and a much stronger one is observed when the sample is tiled 30°. This is consistent with LTEM contrast from Néel domain walls (Fig.4.21f,i) and is a characteristic of interfacially induced DMI. Additionally, no changes in chirality are observed for the domain walls.

In conclusion, it has been shown that a constant chirality can be imparted to a GdCo ferrimagnetic thin film by sandwiching it in between two heavy metals, that have DMI

interactions of opposite magnitude with GdCo. Symmetric multilayers by comparison are achiral. Additionally it has been shown that in these multilayer stacks changing the thickness of the individual layers allows for tuning of the anisotropy and M_s, both of which have been shown to impact the stabilization of skyrmions.

4.3 Topological Spin Textures via Structural Anisotropy

Note: Most of the results discussed in this subsection were previously published in the following paper: ***N. Kent****, R. Streubel, C.H. Lambert, A. Ceballos, S.G Je, S. Dhuey, M.Y. Im, F. Büttner, F. Hellman, S. Salahuddin, P. Fischer,* Generation and stability of structurally imprinted target skyrmions in magnetic multilayers *, APL, 115, 11 (2019).*

In the past two sections control over magnetic structure and topology through shape anisotropy and multilayer composition has been demonstrated, here we combine both concepts to generate novel topologically nontrivial spin textures. This combination has previously been used to enhance skyrmion stability, generate local topological spin textures with varying charge, and locally modify properties of magnetic films [121][22]. Here we discuss the novel topological structures generated, and some of the more general effects, of combining multilayers with finite size effects and shape anisotropy.

4.3.1 Topologically Trivial Spin Textures

In order to combine shape anisotropy with magnetic multilayers the most direct approach is to fabricate nanomagnetic structures, whose magnetization is determined by their shape anisotropy, directly on top of magnetic multilayers (Fig.4.22): this is called shape anisotropy imprinting (SAI). SAI can be broken down into two separate but interconnected phenomena: the film's effect on the disk, and the disk's effect on the film. In both cases, this is determined by the anisotropy of the film, the magnetization of the magnetic nanostructure on top of the film, and the strength of the coupling between the film and the nanostructure. Here, the general effects of SAI on the magnetic structure of the disk and the film will be discussed. SAI's effects on topological magnetic structures will be discussed in the next section.

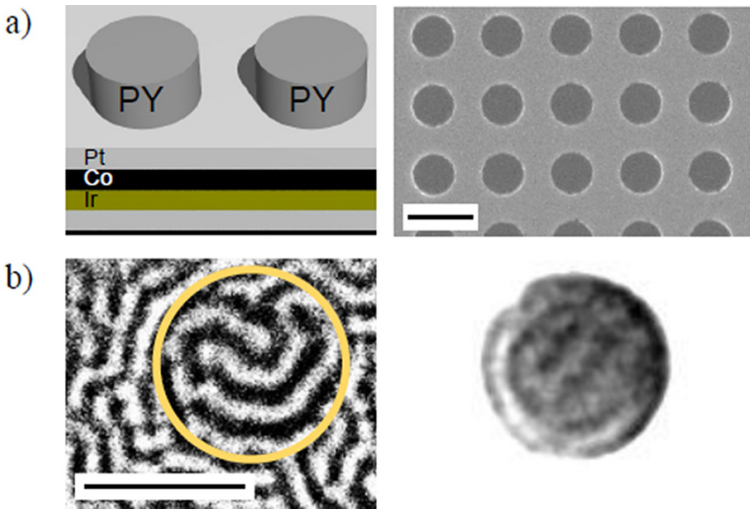

Figure 4.22: a) Left: Schematic of PY heterostructures on top of Ir/Co/Pt multilayers. Right: SEM image of disks on the multilayers. Scale bar is 2μM. b) Left: MTXM image at the CoL_3 edge. Right: MTXM image at the Fe L_3 edge. Scale bar is 1μM for both images. Reprinted from [66], with the permission of AIP Publishing.

In order to understand the magnetic nanostructure's effects on thin film multilayers, Ta[3]+ [Ir(1)/Co(N)/Pt(1)]x7 +Pt[2](nm) (N= 1.5, 2, 3)nm assymetric multilayers with various magnetic permalloy (PY) nanostructures are considered. For N= 1.5nm the film has PMA, for N=2 it has an effective anisotropy close to 0 (Fig.4.24), and for N=3nm the film has easy in-plane anisotropy. This increase of in-plane anisotropy with Co layer thickness makes sense given that the PMA is an interfacially induced effect competing with the easy axis shape anisotropy that increases as the film's thickness increases. This is consistent with previously studied samples [65][64].

The inherent elemental specificity in MTXM allows for measurement of the different structures independently, i.e. recording images of the PY nanostructures at the Fe L_3 edge and the corresponding images of the PMA Co layer at the Co L_3 edge (Fig.4.22). The domain structure of each film was checked in MTXM at remanence to compare with the anisotropy measurements. N=1.5 has only out-of-plane domains and no in-plane magnetization at remanence. An out-of-plane meander pattern and room temperature zero field skyrmions are observed at remanence. For N=2 only the out-of-plane component was imaged with MTXM and the domain pattern (Fig.4.24) is consistent with a spin spiral (both in-plane and out-of-plane components), with some zero field skyrmions observed. This is consistent with the formation of weak stripe domains in thin films for which $K_d \approx K_u$, such as in the Fe/Gd multilayers [113, 115]. N=3 shows no out-of-plane domain structures but, when imaged at a 30° tilt, shows (Fig.4.23f) in-plane domains as expected. It is likely N=2 has in-plane domains at remanence also due to its in-plane magnetization at remanence (Fig.4.24Left), but this has not been confirmed directly with microscopy.

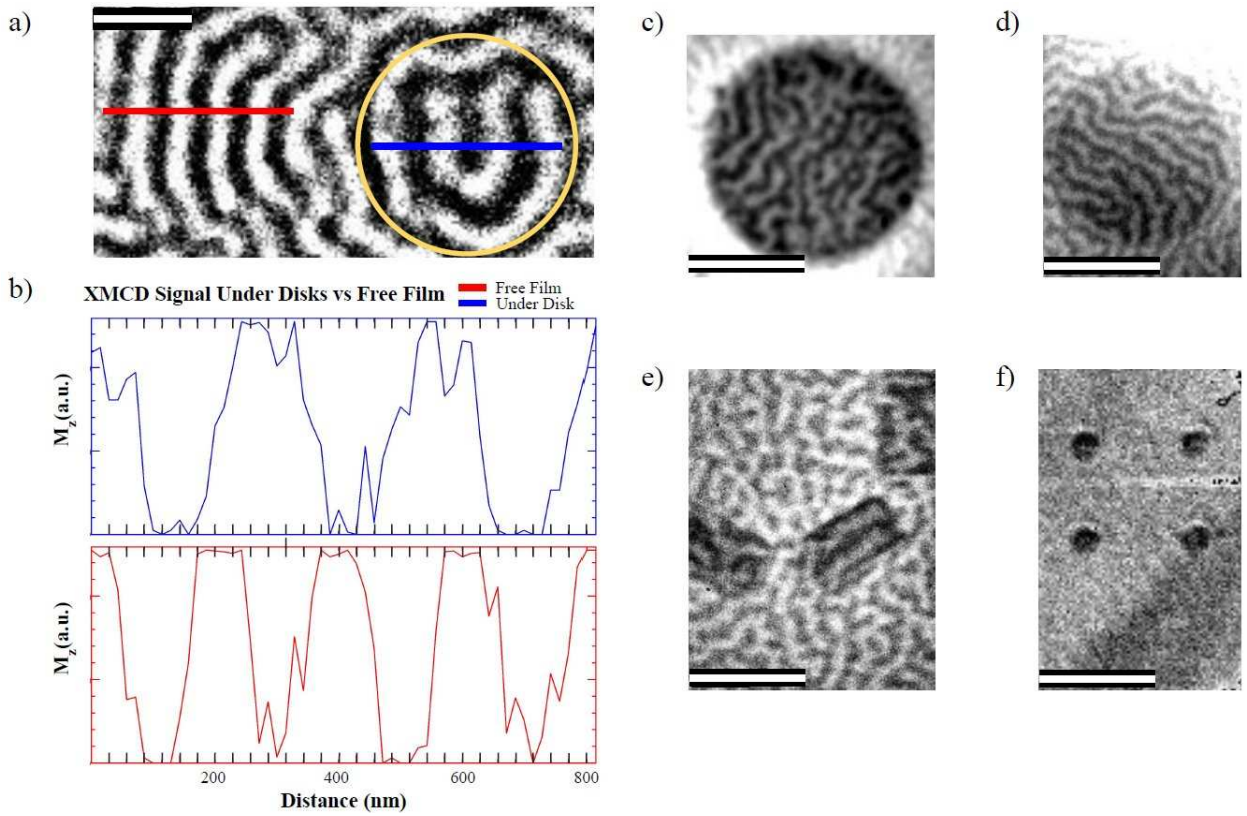

Figure 4.23: All scale bars are 1μm. a) MTXM image and the b) corresponding intensity profiles for measuring domain periodicty underneath and outside a 1μm 30nm thick PY disk in a N=1.5nm film. MTXM images for a N=1.5nm film taken at the Co edge with a PY c) 2 μm diameter, 20nm thick disk, d) 1.5 μm diameter, 10nm thick disk, e) 30nm thick 500x900 μm bars. f) MTXM image taken, with a stage with 30° tilt, at the Co edge of the N=3nm film with easy axis anisotropy showing an in-plane domain. a),b) Reprinted from [66], with the permission of AIP Publishing.

Using MTXM to image the Co film independent of the PY, the film underneath microstructures looks very similar to the domain pattern of the film outside the structures (Fig.4.22b, Fig.4.23a,e,d). It can be seen that there is a noticeable change in size of the domain patterns of both films with an out-of-plane component (N= 1.5nm, 2nm) under PY nanostructures of various shapes, sizes, and thicknesses (Fig.4.23a,b). For the Co N=1.5nm film, the domain periodicity of the free film is measured and under disks with diameter larger than 500nm and thicknesses, 30nm, 20nm, and 10nm (Fig.4.23). Measurements show that, under disks with a thickness of 30nm or 20nm, there is an increase in domain periodicity that is independent of disk diameter. This change in domain periodicity does not vary spatially underneath the nanostructure implying this effect is a general effect of having a PY

capping layer on top of the film. Under 30nm thick disks the domain periodicity increases from (180 ± 20)nm which increases to (240 ± 20)nm. This can be explained by a reduction in stray field energy; since the stray field energy in a magnetic material is inversely proprtional to the relative permeability, μ, the larger the relative permeability is the smaller the magnetic field energy is in that material. Alternatively the relative permeability of a material is the factor of energy reduction for a magnetic field to exist in that material compared with vacuum; permalloy has a relative permeability of 20,000-60,000 [122], resulting in the stray field energy being reduced by several orders of magnitude in a very small volume. This can be understood quantitatively by finding the energy minima of a complex analytical energy equation given for domain periodicity in thin films with DMI given by [123]

$$E_{tot} = M_s^2 F_1(\Delta, t, W, P, \psi) + F_2(\Delta, t, W, P, \psi)$$

$$+\frac{2}{P}\left(\frac{2A}{\Delta} + 2K_u\Delta + \pi D\sin(\psi) - M_s\left(1 - \frac{2W}{P}\right)B_z\right.$$

where t is the film thickness, W is the minority domain width, P is the domain periodicity, Δ is the domain wall width, D is the DMI energy. It is found that reducing the stray field energy, produces a reasonable change in domain periodicity. The percent energy reduction, $E_{\downarrow}$, can be found by varying the stray field energy. This is done by multiplying M_s by $E_{\downarrow}/100$ in the first and last term of the analytical energy equation and the calculating the domain periodicity. For the 30nm thick nanodisks there is found to be a stray field energy reduction of 17%.

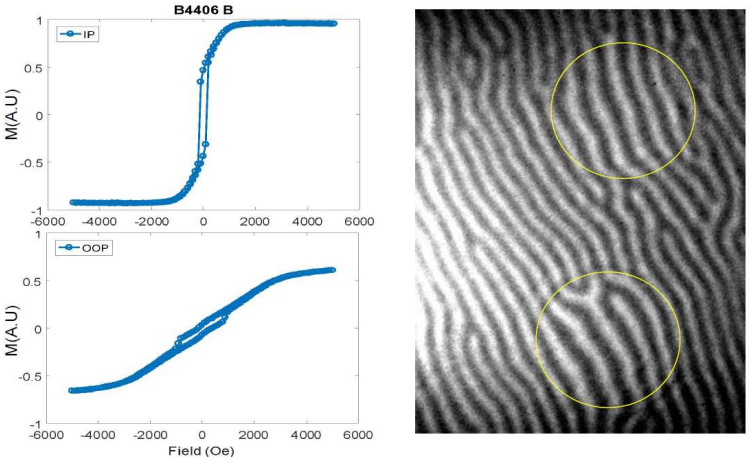

Figure 4.24: Left: In-plane and out-of-plane VSM measurements showing near zero anisotropy in the N=2 film. Right: MTXM image at the Co L_3 edge of the N=2 film, with locations of 1μm PY disks highlighted.

It is observed, for the N=1.5nm film, that underneath PY disks, that would be in a magnetic vortex state if isolated, there is a tendency for the domains to run parallel to the edge of the disk. In order to quantify this behavior the domain wall edge pinning percentage, , P_e, for a film with a PMA domain structure is defined as:

$$P_e = \frac{1}{L} \oint_{edge} \delta(\hat{n}_{xy} \times \nabla M_z) \delta(M_z)$$

Where L is the total edge length of the nanostructure, M_z is the z component of the magnetization, $\hat{n}_{xy}$ is the surface normal vector of the nanostructure in the xy plane, and $\delta(x)$ is the Dirac delta function. This function returns the percentage of the edge of a nanostructure for which there is a domain wall running parallel to the edge.

The P_e of 1μm disks and 900nm x 500nm rectangles were measured on the asymmetric N=1.5 multilayers. As a control, 1μm disk areas were randomly selected on the free film and P_e was measured along the circumferences of these imaginary disks. The P_e of the 1μm disks was found to be 85.2%, higher than the measured P_e 18.3% of the control imaginary disks, or the rectangles. The P_e of the rectangles was found to be 22.5%. The P_e of 1μm disks was measured on the symmetric N=1.5 multilayers and found to be 80.1%, similar to the 1μm diameter disks on the asymmetric multilayers.

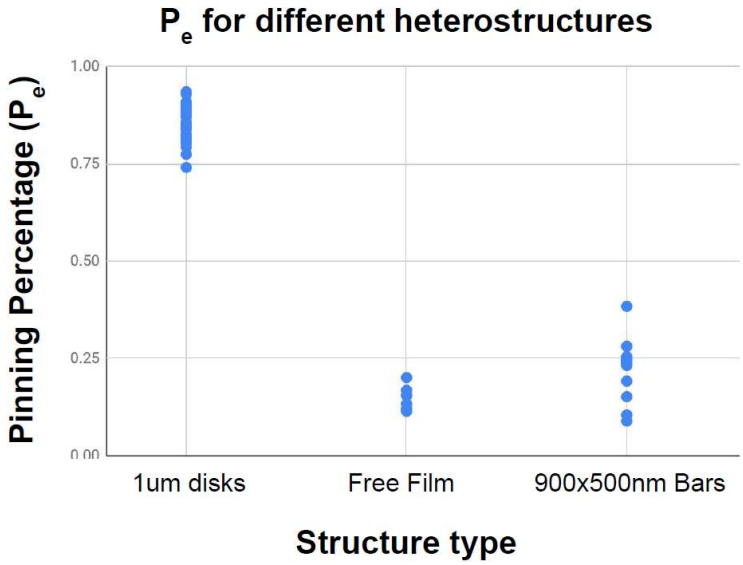

Figure 4.25: Percentage of the edge (P_e) of a micro structure, for which a domain wall is running along the edge. Formally defined by $P_e = \frac{1}{L} \oint_{edge} \delta(\hat{n} \times \nabla M_z) \delta(M_z)$, where $\hat{n}$ is the outwardly pointing normal vector when looking down on the heterostructure.

In order to understand this behavior better, disks were placed on the asymmetric N = (2,3)nm films. For the N=2 films no anisotropy, no domain pinning was detected at all (Fig.4.24) and P_e matched that of the free film. For the in-plane N=3 films the domains wall

were not pinned by the edge of the disks, but rather by the centers of the disks (Fig.4.23f). Quantifying the N=3 film behavior is difficult due to the large size of the in-plane domains relative to the disks: the P_e of control disks is zero.

Given that the pinning of domain walls is a function of the anisotropy of the film and the energy of domain walls is proportional to the anisotropy of the film for thin films, it is reasonable to assume that the structures on top are some how modifying the anisotropy of the film below. If a weak surface anisotropy is induced in the Co films proportional to the magnetization of the vortex disk above then this behavior can be explained. Such an effect is predicted for very weak interlayer exchange coupling [34]. For the N=1.5 film with PMA, domain wall energy is proportional to the PMA; when the PMA is reduced, or the in-plane anisotropy is increased, the domain wall energy is reduced. The edge of the disks, where the in-plane anisotropy is strongest, reduce the energy of domain walls the most, so domain walls have a preference to align on the edge of the disks (Fig.4.25). In the N=3 film, with easy axis anisotropy, the domain wall energy is inversely proportional to the PMA, and the out-of-plane vortex core induces a higher PMA in the film than anywhere else, so domain walls are pinned to vortex cores. In the N=2 film with no effective anisotropy, domain wall energy is not dependent on the anisotropy, so the disks don't pin domain walls anymore (Fig.4.24).

OOMMF simulations are able to confirm, that the in-plane anisotropy of a 1μm diameter, 30nm thick PY disk is largest near the edge of of the disk, by looking at the spatially resolved magnetic torque in the disk with a PMA domain structure (both uniform and multidomain), see Fig.2.4. In a magnetic nanobar structure, the Landau state is preferred when the structure is isolated. In the Landau state the greatest impetus to be in plane is not located on the edge of the bar, resulting in less domain pinning than the vortex disks (Fig.4.23e). The observed domain structure underneath the bars seems to loosely match the Landau state, but it is hard to quantify without precisely knowing the magnetization in the bars. OOMMF simulations of a film with the bulk thickness and properties of the N=1.5 film coupled to a PY vortex nanodisk of appropriate dimensions are not able to reduce the domain wall pinning observed in experiment, even when varying the coupling between the disk and the film over a wide range of couplings strengths. At high coupling strength, $> 0.1\text{erg/cm}^2$, the disk forces the film in plane and at low to negligible coupling strength,

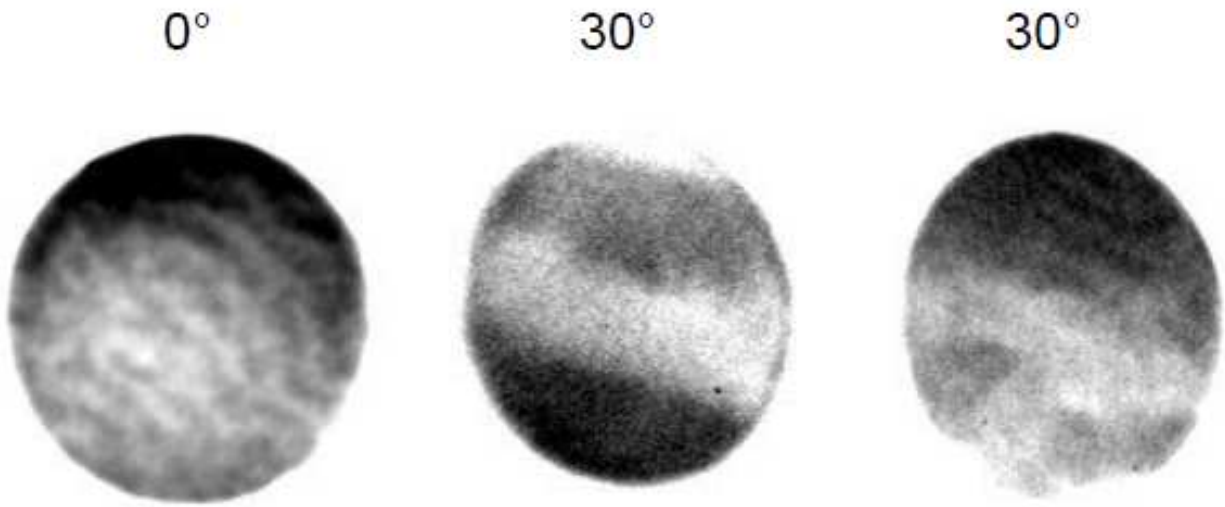

Figure 4.26: MTXM taken at the Fe L_3 of 1.5μm PY disks on a N=1.5 film imaged at different tilt angles showing the out-of-plane and in-plane components of magnetization. Left: The disk has the out-of-plane domain structure imprinted on it from the film below. Middle, right, the in-plane component of the disks shows a double vortex like (middle), and a cross shape in-plane magnetization (right), anomalously.

$< 0.1\text{erg/cm}^2$, no noticeable change is noticed in the film below. A circular domain wall pinning effect can be achieved by reducing the out-of-plane anisotropy of the PMA film for circle of a given radius. The pinning effect due to a vortex core is able to be simulated in a N=3nm film by creating a small region with out-of-plane anisotropy in otherwise uniform easy axis film.

So far we have only considered how the magnetic structure of the film changes due to the nanomagnets on top, but the nanomagnetic structures are also effected by the film. In order to connect the domain structure of the film to the magnetic structure of the disks, a N=1.5nm film underneath a 1.5μm diameter, 30nm thick, PY disk was imaged at the Co L_3 edge. The energy was then changed to the Fe L_3 edge and an out-of-plane component is seen which matches the multidomain structure of the film underneath (Fig.4.22, Fig.4.26left). Such an effect is reproduced in simulation regardless of whether or not there is interlayer exchange coupling; stray fields emanating from the film below are enough to tilt the magnetization of the PY disk out of plane.

The disk was tilted to $\pm 30^\circ$ to image the in-plane component of the magnetization. For disks with a diameter between (500-800)nm the expected magnetic vortex structure is

observed. Anomalously, a mixed in plane, double vortex like state and a cross like in-plane signal is observed in a large number of disks between (900nm-2000)nm (Fig.4.26 middle, right). This effect has not been reproduced in simulation.

In conclusion, the basic principles of shape anisotropy imprinting have been identified: when a magnetic structure, with a varying anisotropy due to its shape, is weakly coupled to a film underneath, the film underneath will experience a weak anisotropy which is proportional to the preferred magnetization of the heterostructure on top and the stray field energy of the film will be modified. The specific effect on the film beneath is dependent on the film's anisotropy, which we can be tuned in multilayers, such as in Ir/Co/Pt by varying the Co thickness, allowing for customization of domain patterns in the film. Additionally the disk is effected by the film: canting slightly out of plane, and forming an anomalous in-plane structure.

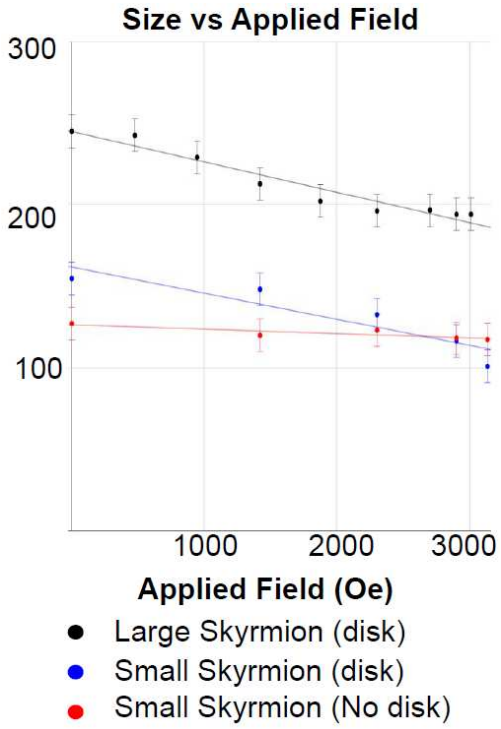

Figure 4.27: Skyrmion diameter in nm versus applied field. Skyrmions underneath disks experience a reduced field due to the PY redirecting field lines.

4.3.2 SAI's effect on Topologically Nontrivial Magnetic Structures

The DMI of the [Ir(1)/Co(1.5)/Pt(1)] x 7 multilayers is responsible for the creation of room temperature zero field skyrmions observed in the film. Here we discuss the effects of nanomagnetic disks on skyrmions, and the creation, stability of nπ(n=2, 3, 4) Target skyrmions (TSk) [37]. Target skyrmions are extended skyrmion spin textures where the z component of magnetization goes through nπ radians of rotation as one moves radially outward from the center of the skyrmion. Using SAI to stabilize and modify topologically nontrivial structures, 30nm thick disks with a diameter of 250nm, 500nm, 1000nm are fabricated on the N=1.5nm [Pt/Co/Ir] multilayers, and the effects of imprinting on topologically nontrivial spin textures is studied.

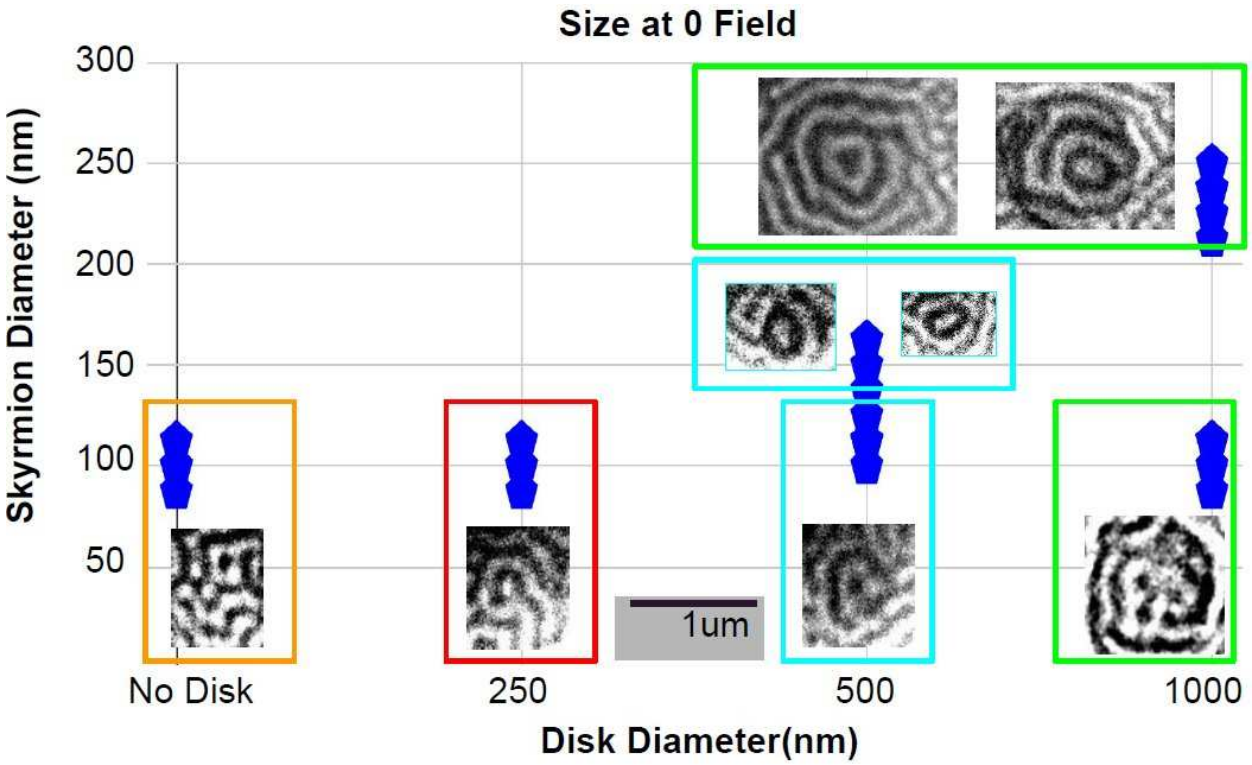

Figure 4.28: Skyrmion diameter vs the diameter of the disk which they are stabilized underneath. Boxes group data points with images of the corresponding skyrmions. Orange box: free film. Red, blue, green boxes correspond to 250, 500, 1000nm disks, respectively.

Both skyrmions and target skyrmions require a constant chirality to have a topological charge, which can be imparted by DMI. To confirm that the DMI, and constant chirality, of the film underneath PY disks is unaffected by the coupling to the heterostructure, an out-of-plane field pulse, with a small in-plane asymmetry is applied in-situ during MTXM. The asymmetric expansion of a bubble domain in the direction of the in-plane asymmetry (Fig.4.29b) confirms a constant Néel type chirality, in agreement with the DMI observed in Ir/Co/Pt multilayers without nanostructures on top.

The diameter of skyrmions in the free film is (120 ± 20)nm. Underneath disks of all sizes, skyrmions of this diameter are observed, see Fig.4.28 bottom row. 250nm diameter disks, 2 times the 120nm skyrmion size, tend to pin these skyrmions almost all of the time (Fig.4.28 red box). 500nm diameter disks stretch these naturally occurring skyrmions out,

sometime asymmetrically, up to an average diameter of 170nm. The ellipse like skyrmions have a major axis of 220nm and a minor axis of 120nm length (top Blue Box). Both of these effects are explainable when one considers domain walls get pinned near the edge of disks. Both of these skyrmions have their size slightly adjusted to align better with the edge of the nanodisk.

In 1μm diameter disks, skyrmions with a (225 ± 20)nm diameter are stabilized (Fig.4.28 top green box). Such a bistability in skyrmion size has been theoretically predicted to exist in films with DMI and shape anisotropy [124]. In this particular case the bistability in skyrmion diameter is caused by the reduction in stray field energy underneath the disks [124].

As an out-of-plane magnetic field is applied in the direction opposite the observed skyrmion's core, the skyrmion diameter shrinks. In Fig.4.27 skyrmion diameter is recorded as a function of applied field in the free film and underneath nanostructures. The rate of change of the skyrmion's diameter is different between the skyrmions in the free film and those underneath nanostructures. The PY nanostructure on top can be viewed as a magnetic shield, redirecting field lines around the film underneath, so the skyrmion feels a smaller effective field. It is unsurprising that this effective reduction occurs with PY as high permeability materials, such as PY and mu-metal,

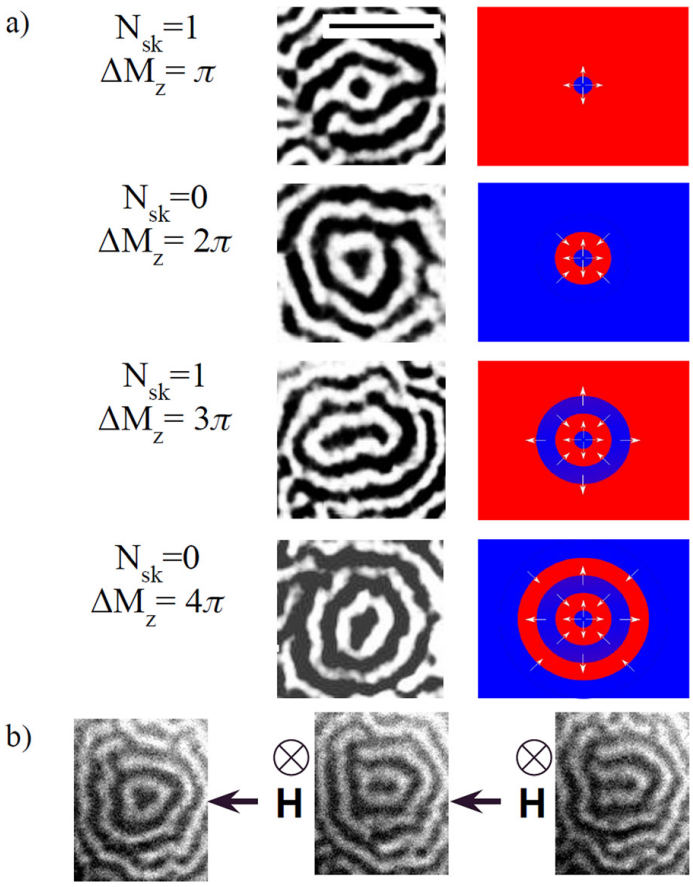

Figure 4.29: (a) XMCD images of 2-4 π TSKs paired with schematics of the structure. Red(blue) corresponds to black (white) out-of-plane magnetization as measured in XMCD. The in-plane arrows show a constant Néel type chirality. Scale bar is 1μm. (b) Néel chirality is confirmed due to a uniform, asymmetric domain expansion from an out-of-plane field pulse with an in-plane asymmetry which is shown. All images were taken at zero field. Reprinted from [66], with the permission of AIP Publishing.

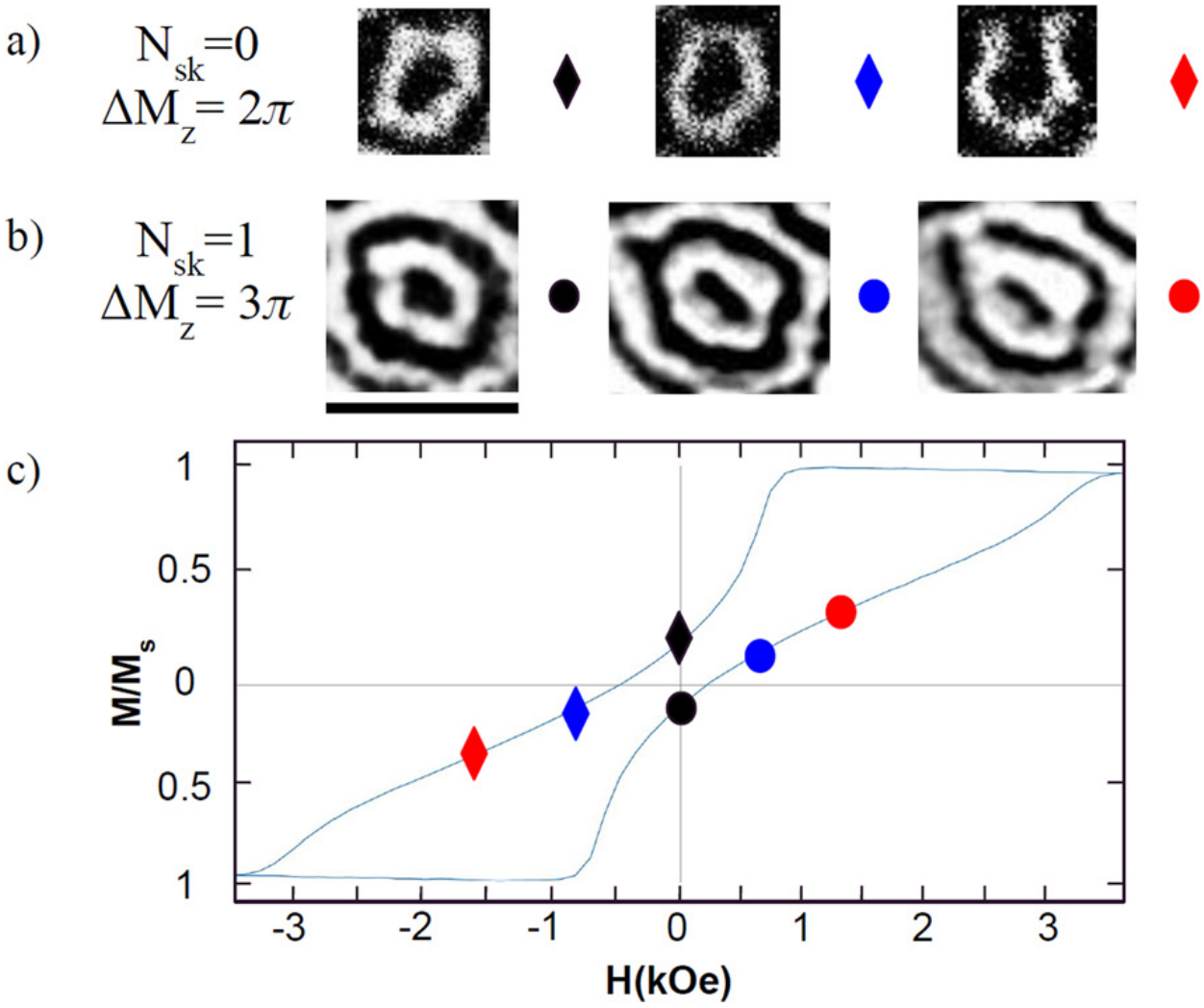

Figure 4.30: (a) Evolution of a 2p TSk in an external field aligned with the spins at infinite (in the direction of the black magnetization). (b) Same as in (a) but for a 3p TSk with an external field aligned with the spins into the white direction. Scale bar: 1μm. (c) M(H) of the multilayers measured with VSM. The black, blue, and red data points correspond to the images for the 2p, 3p TSk. The red markers are where the extended TSk structure collapses. Reprinted from [66], with the permission of AIP Publishing.

are often used as magnetic shielding.

In several 1μm disks where P_e is unusually high nπ(n=2, 3, 4) target skyrmions are stabilized (Fig.4.29a) due to the reduced stray field energy and enforced radial symmetry. No higher order target skyrmions are stabilized as the 4π TSk takes up the entire area underneath the 1μm disks and, necessarily, $P_e = 1$. Since the topological charge of a TSk is $N_{sk} = (1-\cos(\Delta Z))/2$, where ΔZ is the number of radians the z component of magnetization

rotates through, the topological charge of each target skyrmion toggles back and forth from 0 to 1 for each additional "ring" on the target (Fig.4.29). As such, it is possible to study the stability and evolution of TSks as a function of external magnetic field.

In Fig.4.30 a 2π TSk with $N_{sk} = 0$ and a 3π TSk with $N_{sk} = 1$ are subjected to an external magnetic field in the direction of the spins at infinity for each structure: parallel to the core of the 2π TSk and anti-parallel to the core of the 3π TSk. Depending on whether the initial topological charge of the TSk structure is 0 or 1 there is a is a change of -1 or +1, respectively, to the total topological charge when an external field collapses the structure at 1.6kOe (Fig.4.30 red markers). The collapse of the ring like structures occurs in a similar manner to the collapse of a 2π domain wall, and is in agreement with other observed 2π TSks [125].

Both the 2π and 3π collapse at the same field value, because a 3π TSk is just a classic skyrmion wrapped by a topologically trivial 2π TSk. Near saturating fields, we expect all structures to collapse to a uniform magnetization.

To briefly summarize this section, it was found that the properties of skyrmions are able to be manipulated by SAI and higher order topological structures can have their structure stabilized with SAI. Additionally, additive DMI and tunable anisotropy make Ir/Co/Pt multilayers very attractive for exploring topologically nontrivial magnetic structures.

4.3.3 Creating Magnetic Hopfions

Theory has shown that a 2π TSk can transform into a Hopfion, in a nanomagnetic pillar with DMI, when the PMA at the top at the bottom of the TSk is increased ([46, 50]). This causes the magnetization at the top and bottom of the TSk to match the magnetization at the center of the TSk (Fig.4.32a). Further simulations show that taking a low PMA layer, with K_{u1} that hosts TSks, and sandwiching it between two high PMA layers, with K_{u2} of the same thickness as the first layer, a Hopfion will form when $K_{u2} : K_{u1} \geq 3$ (Fig.4.31b,c). When $K_{u2} : K_{u1}$ is two or smaller (Fig.4.31a) the out-of-plane domain structure of the TSk will extend all the way through the material (Fig.4.32a) and a Hopfion won't be stabilized (Fig.4.31a).

Q=1 Hopfions are found in
[Ir(1nm)/Co(1nm)/Pt(1nm)]x10 +
[Ir(1nm)/Co(1.5nm)/Pt(1nm)]x10 +
[Ir(1nm)/Co(1nm)/Pt(1nm)]x10 (Fig.4.32a) multilayers (S30) deposited by sputtering and shaped into pillars of 400nm diameter (Fig.4.33c). Even though these pillars have the correct PMA ratio between the high and low PMA layers, $K_{u2} : K_{u1} \approx 4 : 1$, distinguishing Hopfions from TSks is nontrivial due to their shared symmetries; 2π TSks and Q=1 Hopfions are indistinguishable in MTXM (Fig.4.32b).

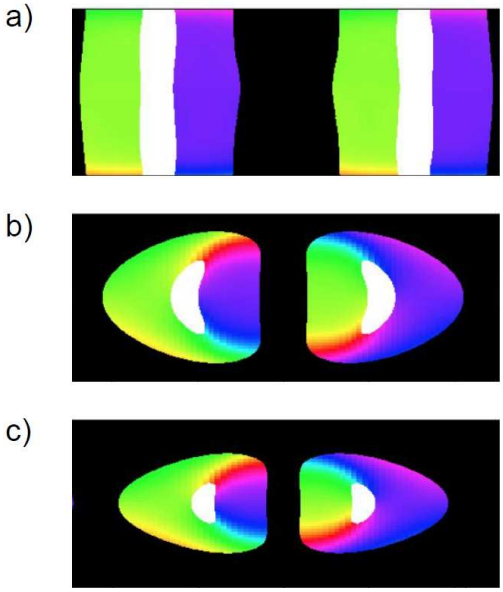

Figure 4.31: A slice along the x-z plane (as defined in Fig.4.32) of a variable PMA magnet with DMI hosting a Hopfion. Black corresponds to up, and white to down (as in Fig.4.32), and the color refers to the in-plane (x-y plane) magnetization direction as seen in the color wheel of Fig.4.32. The PMA in the middle1/3 of each simulation is lower than the PMA of the top, bottom 1/3 of each simulation. The ratio of high to low PMA is a) 2:1, b) 3:1, c) 4:1.

Distinguishing a Hopfion from a TSk can be accomplished by measuring the same sample in depth averaging MTXM and surface sensitive X-PEEM; A sample with an out-of-plane "bullseye" like structure when measured in MTXM, and the in-plane Néel type chirality measured in XPEEM is unique to a Hopfion transformed from a TSk stabilized by interfacial DMI (Fig.4.32b). A TSk when measured in the same way, will show the same MTXM signal as a Hopfion, but will also show a bullseye like structure when imaged in XPEEM since the out-of-plane component of magnetization extends to the top and the bottom of the magnetic material (Fig.4.32). Additionally, the simulations show that when there is an out-of-plane bullseye like magnetic structure that does not extend all the way through the sample (Fig.4.31) a Hopfion is always formed; if this magnetic signal is measured in XPEEM and MTXM and it can be confirmed the central layers can host a TSk, then a Q=1 Hopfion is most certainly stabilized.

In 24 of the 25 400nm diameter pillars of S30 measured a bullseye like out-of-plane magnetic signal is observed (Fig.4.33c). This is expected when the average domain width is approximately one third the diameter of the pillar, and such an effect has been previously used to stabilize TSk, [22], and is theoretically predicted to stabilize Hopfions [46, 50]. When the exact same set of disks is imaged in surface sensitive XPEEM, in-plane magnetic contrast

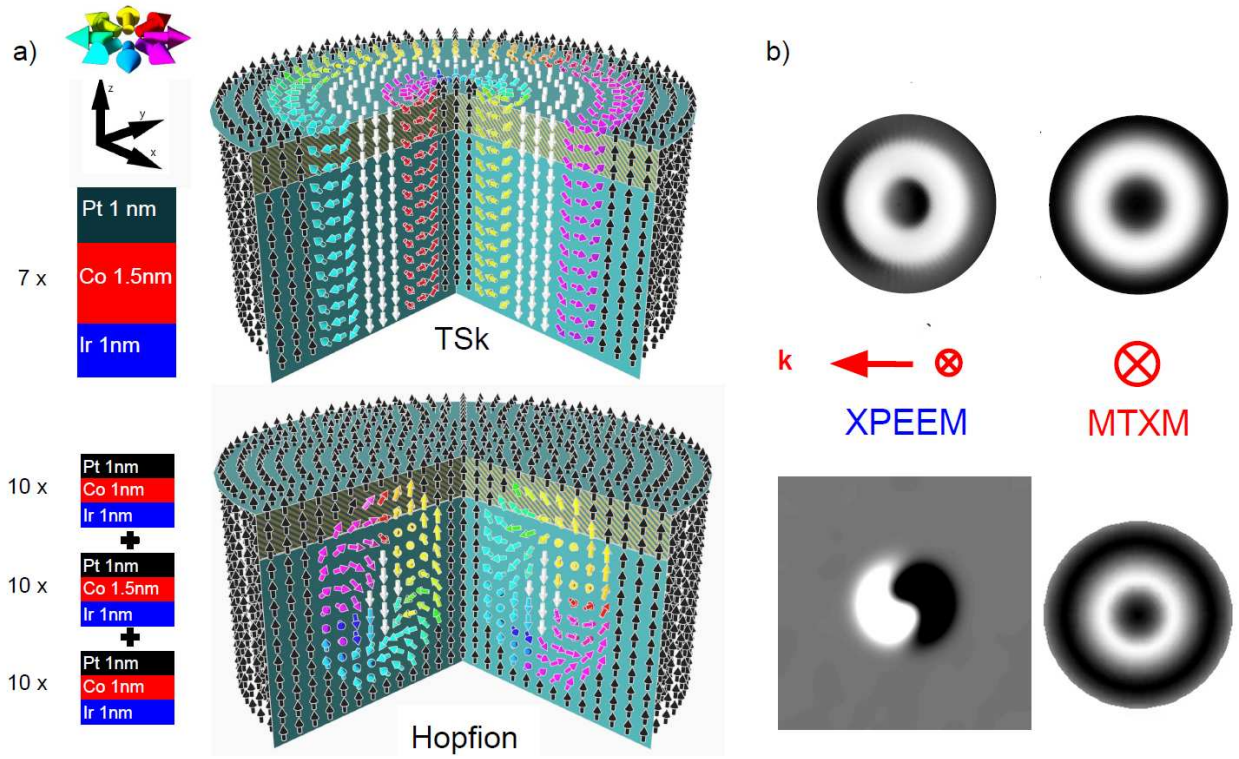

Figure 4.32: Spin texture of TSk and Hopfions. a) Structure of a 2π TSk (top) and a symmetric Q=1 Hopfion (bottom) next to schematics of the Ir/Co/Pt multilayers which host them. The highlighted region shows the approximate depth sensitivity of XPEEM. b) Simulated X-PEEM and MTXM signals for a TSk (top) and a Hopfion (bottom) calculated from the simulations shown in Fig.4.31. MTXM images for both structures are similar due to the shared symmetries between a TSk and a Hopfion. The direction of the photon angular momentum is shown for XPEEM, which is sensitive to both the in and out-of-plane components of magnetization and MTXM, which is only sensitive to the out-of-plane component.

is seen which matches that of a Hopfion, transformed from a TSk stabilized by interfacial DMI (Fig.4.31d). A 3D magnetization reconstruction, generated by rotating the sample in XPEEM, shows a uniform out-of-plane signal in the disks with the in-plane Hopfion signal; this also agrees with the magnetic structure of a Q=1 Hopfion, (Fig.4.32a, Fig.4.31c,d).

To confirm that the combination of MTXM and XPEEM can distinguish TSk from Hopfions and to show that the central layers of sample S30 can host a TSk, [Ir(1nm)/Co(1.5nm)/Pt(1nm)]x7 (S7), inspired by other TSk hosting samples [66], multilayers were shaped into pillars of varying diameters and measured in the two x-ray microscopes. In both MTXM and XPEEM, a PMA domain structure is observed in S7, regardless of pillar diameter, showing that surface sensitive XPEEM is measuring primarily an out-of-plane

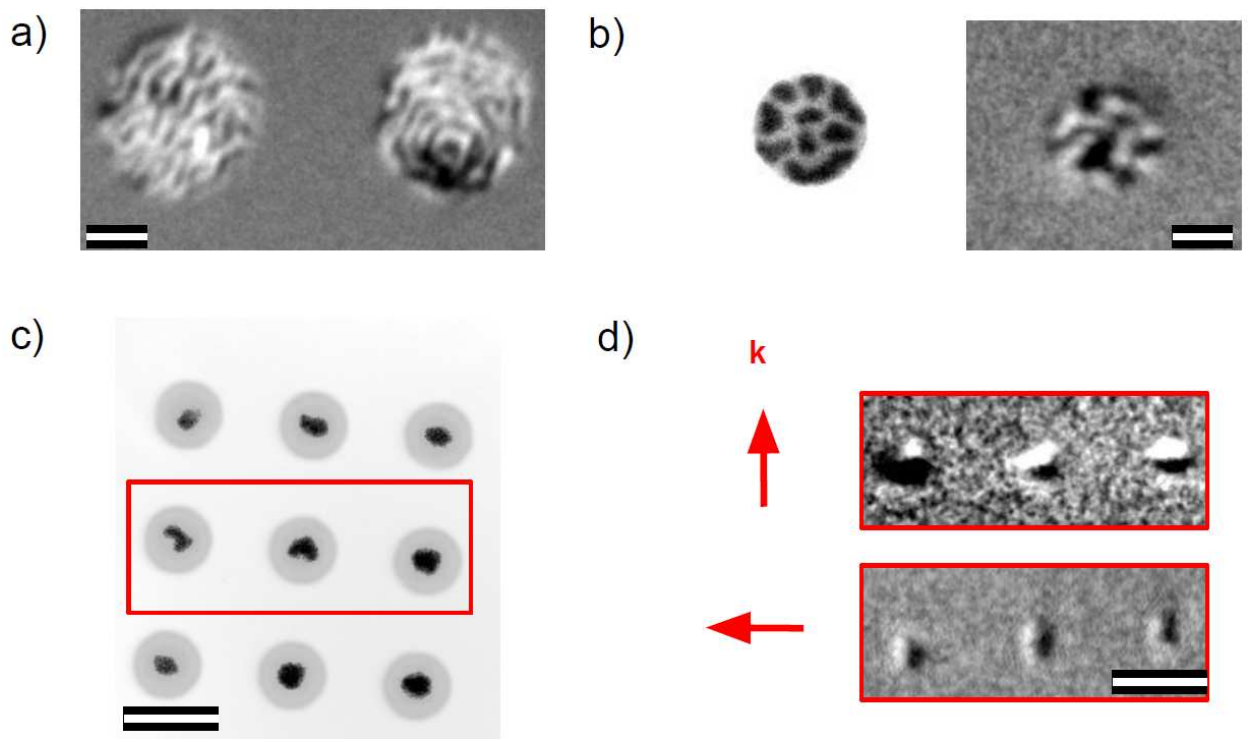

Figure 4.33: All scale bars are 500nm. a) XPEEM image of pillars of S7. A PMA domain structure is observed matching what is seen in TXMCD. A 2π TSk can be seen in the bottom section of the right pillar. b) Right: MTXM image of a 1μm diameter disk of sample S30. Left: XPEEM image of the same exact disk. The magnetic contrast is noticeably different, showing magnetic contrast from spin textures with both in-plane and out-of-plane components. c) TXMCD image of 400nm disks showing the characteristic bullseye out-of-plane magnetic structure of a Q=1 Hopfion. The red box highlights the disks shown in d). d) XPEEM images of disks from c) in the red box, with two incoming directions of x-rays. The contrast change between the different incoming XPEEM direction confirms that the magnetic signal is in-plane. This in-plane magnetic contrast signal matches that of the top surface of a Hopfion stabilized in a material with a D vector in-plane. (Fig.4.32a, Fig.4.31). In X-PEEM isolated nanostructures (Fig.4.32b) have charge build up near their edges, which is why the magnetic contrast in d comes from a smaller region then c).

magnetic signal in sample S7 (Fig.4.33a). This is in direct contrast to S30, which even for larger pillars of material, > 600nm diameter, a magnetic signal that is a combination of in-plane, out-of-plane, and canted magnetic contrast (Fig.4.33b) is seen. Furthermore, a 2π TSk is directly measured in S7 (Fig.4.33a) showing that the out-of-plane domain structure of the TSks seen in S7 extends all the way through the thickness of the sample.

The combinations of surface sensitive and bulk averaging magnetic measurements with a Q=1 Hopfion's signal, the contrast with a TSk that extends all the way through the material using the same measurements, and the theoretical simulations that show a Hopfion is always

stabilized when the out-of-plane bulls-eye like structure does not extend all the way through the magnetic material, confirms that Q=1 Hopfions are stabilized in the variable PMA pillars of sample S30 with 400nm diameter. Variable PMA multilayer pillars have successfully stabilized Hopfions and have the potential to generate other exotic spin textures.

Chapter 5

Conclusion and Outlook

5.1 Conclusion

To address the question of topological and structural nanomagnetism, various prototypical material systems were studied experimentally and supported via micromagnetic simulations. The properties of nanomagnetic heterostructures whose magnetization is determined by shape anisotropy and whom interact with each other through their magnetic fields were observed. Coupled vortices show how topologically nontrivial spin textures in heterostructures interact with each other via the stray field. The stray field interaction in XY spin arrays was used to generate collective topologically nontrivial magnetic structures and collective magnetic properties, which differ from the constituent nanostructures. Jamming magnetic nanoparticles at a liquid liquid interface in ferrofluid resulted in liquid ferromagnetic droplets.

The discussion of interacting nanostructures was followed by one of magnetic thin film multilayers which generate topologically nontrivial spin textures. The magnetic properties of these multilayers are able to be tuned by varying the thickness of individual layers, number of repeats in the multilayer, and the composition of the layers. In Fe/Gd multilayers, without DMI, it was found that shape anisotropy and M_s play a crucial role in stabilizing skyrmions. It was found that in ferrimagntic asymmetric Pt/GdCo/Ir multilayers a constant chirality is induced, due to DMI, in the ferrimagnetic material resulting in ferrimagnetic skyrmions.

Finally, both magnetic multilayers and nanostructures with shape anisotropy were com-

bined. Shape anisotropy imprinting in Ir/Co/Pt multilayers were investigated by weakly coupling nanomagnetic permalloy structures to the multilayers. It was found that the properties of the multilayers can be locally modified, depending on the size and shape of the nanomagnet on top, resulting in modification of topological spin textures found in the film and generation of nπ TSk.

In magnetic multilayer pillars with spatially varying DMI, Q=1 Hopfions were stabilized and identified through a combination of surface sensitive and bulk microscopies. This dissertation has shown that novel nanomagnetic phenomena and structures can be generated through control over topology and structure in nanomagnets.

5.2 Outlook

Even though progress was made with understanding structural and topological magnetism in this dissertation, there are still many open questions that future research needs to address.

Scientific Outlook

There is still much work to be done with regards to understanding the science of magnetic textures generated by the systems in this dissertation. There were magnetic structures observed in structural anisotropy imprinting that are not fully understood: the anomalous in-plane structure found in Permalloy disks (Fig.4.26) and the domain wall pinning observed in the films (Fig.4.25). Both of these phenomena are connected to the shape anisotropy of the disk and explanations for these behaviors could lead to new types of magnetic interaction.

In FLDs, changing the composition, and type, of the magnetic nanoparticles that compose the FLD could allow for unprecedented customization of magnetic properties, in a way not possible in solid magnets. The MNPs in the fabricated FLDs can be customized and shaped differently. Additionally, it should be possible to induce an anisotropy in FLDs by changing the ambient conditions in which the FLD is stabilized in; when the FLD is jammed all the MNPs are aligned in a random way, if a field was applied to the MNPs when the FLD is jammed it should be able to create a net anisotropy by aligning the anisotropy axis of the individual MNPs.

Understanding the dynamics of a confined Hopfion could lead to all electric detection of Hopfions enabling them to be used in data storage. It is also essential to understand Hopfion-Hopfion interactions; when Hopfions interact they can link, repulse, or annihilate themselves effectively being able to directly perform complex mathematical operations, such as multiplication and division. This is very different from skyrmions who either repel or annihilate each other. In the future, with atomic control of magnetic atoms it would be possible to generate magnetic structures with precisely controlled spatially varying DMI or systems with precisely controlled spatially varying symmetric exchange constants. Both of these systems could enable stabilization of sub-nanometer Hopfions with a Hopf charge greater than one (Fig.5.1) [51].

Instrumentation Outlook

The systems studied in this dissertation followed a progression in dimensionality from two dimensional systems to three dimensional systems, i.e., two-dimensional coupled vortices and XY spins lead to three dimensional arrangements of nanomagnetic structures (ferromagnetic liquid droplets). Similarly, varying the spatial properties over all three dimension in magnetic multilayers turns films which host two dimensional skyrmions into three dimensional structures which host three dimensional Hopfions. Progress along these lines not only requires advances in synthesis and characterization, but will accelerate current developments using state-of-the-art tools. True three dimensional nano-fabrication techniques, such as electron beam induced deposition [126] and two photon lithography [127] will allow for new types of nanostructures, leading to new types of topological magnetic structures and collective three dimensional magnetic systems. One can envision that a three dimensional magnetic spin ice systems could host three dimensional magnetic monopoles, similar to how two dimensional spin ice systems host two dimensional magnetic monopoles [26].

As nanomagnetic systems become more complex physically, advancements in measurement techniques are equally essential. Advanced three dimensional magnetic characterization techniques have a resolution on the order of 50nm [128], but identifying a Hopfion requires a resolution on the order of nanometers. Additionally, the magnetic structures described in this dissertation can be excited by a short (sub-ns) magnetic field or current pulses, or even

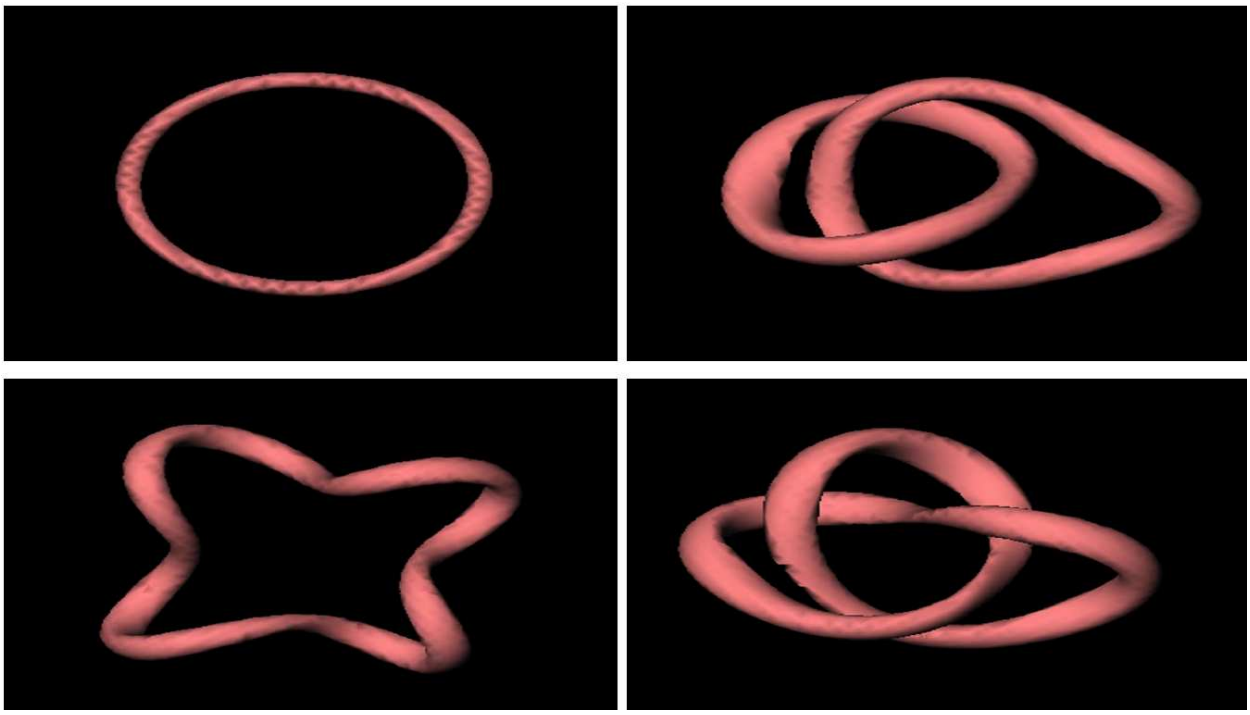

Figure 5.1: Diagrams of Q=7 Hopfions, with several distinct structural configurations. All of these configurations have the same topological charge, and can be smoothly permuted into each other. This figure was created (with permission) from data generated by Paul Sutcliffe.

faster optical pulses [129]. Topological magnetic structures show great technological potential due to their stability and mobility in external fields. Ultimately, the goal is to resolve the spin dynamics in those complex 3D structures with spatiotemporal resolutions that match the fundamental length and time scales of magnetism, i.e. in the nm and fsec ranges. A full 3D characterization with sufficient temporal resolution will also inherently provide insight into phenomena, that originate at buried interfaces, e.g. the DMI in magnetic multilayers. The upcoming capabilities at next generation x-ray facilities, i.e. fully coherent X-ray Free Electron Lasers have the potential to address those challenges.

Technological Outlook

In the search for low-power electronics, which is required in view of the ever increasing demand for information technology, spintronics is seen as a major enabler. This is primarily due to the fact that charge-based devices have the inevitable Ohm-loss, which is exacerbated

at shrinking dimensions due to the inability to transport sufficient heat away. Novel spin textures, such as skyrmions have therefore come into focus [21].

Systems with nanodisks pinning skyrmions in a random lattice via structural anisotropy imprinting are promising candidates for neural network reservoirs (NNR) [130]: chaotic systems that are complex enough to allow for an approximation of a neural network using multiple inputs and outputs. For skyrmions in a random lattice distorting their structure via a sub-nanosecond pulse will give rise to anomalous anisotropic magneto resistance that is chaotic enough to be used as a NNR.

Hopfions hold significant technological potential. For Hopfions with a large Hopf number, multiple structurally distinct Hopfions with the same Hopf number can exist at several different energetic minima (Fig.5.1); in a magnetic data storage system that utilizes Hopfions, data could be stored, on the nanoscale, i.e., as octal instead of binary, increasing data storage density significantly. Additionally, since Hopfions are three dimensional, it should be possible to store multiple Hopfions at the same lateral position further increasing data storage density. Recent theoretical work on the dynamics of Hopfions show that they are promising candidates for spintronic applications since they can be pushed by a current in a straight line, unlike skyrmions, as they have no gyrovector, which is responsible for the Magnus force in skyrmions [21, 131].

Despite the fact that a fundamental understanding of FLDs is almost completly lacking, the prospect that a ferromagnetic liquid could not only be reshaped into any configuration, but that ferromagnetism itself could be turned on and off by a chemical control of the jamming is tantalizing. Coupling ferromagnetic liquid droplets with motors/ actuators would be a first step towards liquid robotics since they can be precisely and reshaped controlled by magnetic fields. The chemistry of FLDs can also be improved: FLDs have only been stabilized in toluene. Finally, the ability to stabilize FLDs in aqueous solutions could largely impact medical science allowing for in-situ surgery.

This disseration has provided evidence, that the combination of structure and topology in confined nanomagnetic system is a viable path to discover novel phenomena, where a fundamental understanding of the underlying physics will likely lead to scientific and technological advancement.

Bibliography

1. The Early History of Magnetism. *Nature* **13,** 523. ISSN: 1476-4687. `https://doi.org/10.1038/013523a0` (1876).
2. O'Grady, P. F. *Thales of Miletus: The Beginnings of Western Science and Philosophy* (Routledge, 2002).
3. Neckam, A. *De naturis rerum libri duo, with the poem of the same author, De laudibus Divinae Sapientiae* (ed Wright, T.) (Longman, Green, Longman , Roberts, and Green, 1863).
4. De Maricourt Pierre, B. A. *The letter of Petrus Peregrinus on the magnet, A.D. 1269* (Sagwan Press, 2015).
5. Gilbert, W. *William Gilbert of Colchester, physician of London, On the loadstone and magnetic bodies and on the great magnet the earth. A new physiology, demonstrated with many arguments and experiments* (New York, J. Wiley and son, 1893).
6. De Coulomb, C.-A. Premier mémoire sur l'électricité et le magnétisme. *Histoire de l'Académie Royale des Sciences,* 569 (1785).
7. Ørsted, H. C., Jelved, K. & Jackson, A. D. *Selected Scientific Works of Hans Christian Ørsted* (Princeton University Press, Princeton, New Jersey, 2014).
8. Ampère, A.-M. *Exposé des nouvelles découvertes sur l'électricité et le magnétisme* (Chez Mequignon-Marvis, 1822).
9. Fleisch, D. *A Student's Guide to Maxwell's Equations* (Cambridge University Press, The Edinburgh Building, Cambridge CB2 8RU, UK, 2008).

10. Williams, L. P. *Michael Faraday, a biography* (Basic Books, New York, New York, 1965).

11. Doppelbauer, M. *A short history of electric motors 1800-1893* `http://www.eti.kit.edu/english/1376.php`.

12. *Electricity generation by source via the International Energy Agency* `https://www.iea.org/data-and-statistics?country=WORLD`.

13. Néel, L. Propriétées magnétiques des ferrites; Férrimagnétisme et antiferromagnétisme. *Annales de Physique* **3,** 137 (1948).

14. Langevin, P. Magnetisme et theorie des electrons. *Annales de chimie et de physique* **5,** 70 (1905).

15. Langevin, P. L'hypothese du champ moleculaire et la propriete ferromagnetique. *Journal de Physique et le Radium* **5,** 661 (1907).

16. Bitter, F. Experiments on the nature of Ferromagnetism. *Phys. Rev. B.* **108,** 507 (1932).

17. Gerlach, W. & Stern, O. Two phenomena, discovered with the help of the new amplifiers. *Zeitschrift für Physik* **20,** 349 (1922).

18. Tatoute. *Stern-Gerlach experiment svg.svg* `https://commons.wikimedia.org/wiki/File:Stern-Gerlach_experiment_svg.svg` (2020).

19. Dirac, P. The Quantum Theory of the Electron. *Proceedings of the Royal Society, London* **A117,** 610 (1928).

20. Heisenberg, W. Zur Theorie des Ferromagnetismus. *Zeitschrift für Physik* **49,** 619 (1928).

21. Fert, A., Reyren, N. & Cros, V. Magnetic skyrmions: advances in physics and potential applications. *Nature Reviews Materials* **2,** 17031 (2017).

22. Zheng, F., Li, H., Wang, S., Song, D., Jin, C., Wei, W., Kovács, A., Zang, J., Tian, M., Zhang, Y., Du, H. & Dunin-Borkowski, R. E. Direct Imaging of a Zero-Field target Skyrmion and Its Polarity Switch in a Chiral Magnetic Nanodisk. *Phys. Rev. Let.* **119,** 197205 (2017).

23. Fischer, P., Im, M., Yamada, K., Ono, T. & Thiaville, A. X-ray imaging of vortex cores in confined magnetic structures. *Phys. Rev. B* **83,** 212402 (2011).

24. Col, S. D., Jamet, S., Rougemaille, N., Locatelli, A., Mentes, T. O., Burgos, B. S., Afid, R., Darques, M., Cagnon, L., Toussaint, J. C. & Fruchart, O. Observation of Bloch-point domain walls in cylindrical magnetic nanowires. *Phys. Rev. B* **89,** 180405 (2014).

25. Li, Q., Kartikowati, C., Horie, S., Ogi, T., Iwaki, T. & Okuyama, K. Correlation between particle size/domain structure and magnetic properties of highly crystalline Fe3O4 nanoparticles. *Scientific Reports* **7** (2017).

26. Pollard, S., Volkov, V. & Zhu, Y. Propagation of magnetic charge monopoles and Dirac flux strings in an artificial spin-ice lattice. *Phys. Rev. B* **85,** 180402 (May 2012).

27. Wang, Z. K., Lim, H. S., Zhang, V. L., Goh, J. L., Ng, S. C., Kuok, M. H., Su, H. L. & Tang, S. L. Collective Spin Waves in High-Density Two-Dimensional Arrays of FeCo Nanowires. *Nano Letters* **6,** 1083 (2006).

28. Akbarzadeh, A., Samiei, M. & Davaran, S. Magnetic nanoparticles: preparation, physical properties, and applications in biomedicine. *Nanoscale Res Lett* **7,** 3520 (2012).

29. Binasch, G., Grünberg, P., Saurenbach, F. & Zinn, W. Enhanced magnetoresistance in layered magnetic structures with antiferromagnetic interlayer exchange. *Phys. Rev. B.* **39,** 4828 (1989).

30. Baibich, M. N., Broto, J. M., Fert, A., Nguyen van Dau, F., Petroff, F., Etienne, P., Creuzet, G., Friederich, A. & Chazelas, J. Giant magnetoresistance of (001)Fe/(001)Cr magnetic superlattices. *Phys. Rev. Lett.* **61,** 2472 (1988).

31. Streubel, R., Kronast, F., Reiche, C., Mühl, T., Wolter, A., Schmidt, O. & Makarov, D. Vortex circulation and polarity patterns in closely packed cap arrays. *Applied Physics Letters* **108,** 042407 (2016).

32. Li, J., Tan, A., Moon, K., Doran, A., Marcus, M., Young, A., Arenholz, E., Ma, S., Yang, R., Hwang, C. & Qiu, Z. Tailoring the topology of an artificial magnetic skyrmion. *Nature communications* **5,** 4704 (2014).

33. Maciel, N., Marques, E., Naviner, L., Zhou, Y. & Cai, H. Magnetic Tunnel Junction Applications. *Sensors* **20,** 121 (2019).

34. Hubert, A. & Schafer, R. *Magnetic Domains* (Springer, New York, New York, 2009).

35. Cortes-Ortuno, D., Nehruji, V., Pepper, R. A. & Fangohr, H. OOMMF extension: Dzyaloshinskii-Moriya interaction (DMI) for crystallographic classes T and O (Version v1.0). *Zenodo,* doi.org/10.5281/zenodo.1196820 (2018).

36. Mulkers, J., Van Waeyenberge, B. & Milošević, M. Effects of spatially engineered Dzyaloshinskii-Moriya interaction in ferromagnetic films. *Phys. Rev. B* **95,** 144401 (2017).

37. Bogdanov, A. & Hubert, A. The stability of vortex-like structures in uniaxial ferromagnets. *Journal of Magnetism and Magnetic Materials* **195,** 182 (1999).

38. Skomski, R., Oepen, H.-P. & Kirschner, J. Unidirectional anisotropy in ultrathin transition-metal films. *Phys. Rev. B* **58,** 11138 (17 1998).

39. Guslienko, K. Y., Novosad, V., Otani, Y., Shima, H. & Fukamichi, K. Magnetization reversal due to vortex nucleation, displacement, and annihilation in submicron ferromagnetic dot arrays. *Phys. Rev. B.* **65,** 024414 (2001).

40. Wang, R., Nisoli, C., Freitas, R., Li, J., McConville, W., Cooley, B., Lund, M., Samarth, N., Leighton, C., Crespi, V. & Schiffer, P. Artificial 'spin ice' in a geometrically frustrated lattice of nanoscale ferromagnetic islands. *Nature* **439,** 303 (2006).

41. Zhang, S., Gilbert, I., Nisoli, C., Chern, G.-W., Erickson, M., O'Brien, L., Leighton, C., Lammert, P., Crespi, V. & Schiffer, P. Crystallites of magnetic charges in artificial spin ice. *Nature* **500,** 553 (2013).

42. Stiles, M. Interlayer exchange coupling. *Journal of Magnetism and Magnetic Materials* **200,** 322 (1999).

43. Fischbacher, T., Franchin, M., Bordignon, G. & Fangohr, H. A Systematic Approach to Multiphysics Extensions of Finite-Element-Based Micromagnetic Simulations: Nmag. *IEEE Transactions on Magnetics* **43,** 2896 (2007).

44. Donahue, M. & Porter, D. *OOMMF User's Guide, Version 1.0* 1990.

45. Hackbusch, W. Hierarchische Matrizen: Algorithmen Und Analysis. *Springer Science and Business Media* (2009).

46. Sutcliffe, P. Hopfions in chiral magnets. *J. Phys. A* **51,** 375401 (2018).

47. Gilbert, T. & Kelly, J. Anomalous rotational damping in ferromagnetic sheets. *Conf. Magnetism and Magnetic Materials* (1955).

48. Braun, H.-B. Topological effects in nanomagnetism: from superparamagnetism to chiral quantum solitons. *Advances in Physics* **61,** 1 (2012).

49. Beg, M., Carey, R., Wang, W., Cortés-Ortuño, D., Vousden, M., Bisotti, M.-A., Albert, M., Chernyshenko, D., Hovorka, O., Stamps, R. & Fangohr, H. Ground state search, hysteretic behaviour, and reversal mechanism of skyrmionic textures in confined helimagnetic nanostructures. *Scientific Reports* **5,** 17137 (2015).

50. Liu, Y., Lake, R. K. & Zang, J. Binding a hopfion in a chiral magnet nanodisk. *Phys. Rev. B* **98,** 174437 (2018).

51. Rybakov, F. N., Kiselev, N. S., Borisov, A. B., Döring, L., Melcher, C. & Blügel, S. *Magnetic hopfions in solids* 2019. arXiv: `1904.00250`.

52. Stöhr, J. & Siegmann, H. *Magnetism From Fundamentals to Nanoscale Dynamics* (Springer, New York, New York, 2006).

53. P. Carra, P. C., Thole, B., Altarelli, M. & Wang, X. X-ray Circular Dichroism and Local Magnetic Fields. *Phys. Rev. Lett. 70, 694,* 694 (1993).

54. Foner, S. Vibrating Sample Magnetometer. *Review of Scientific Instruments* **27,** 548 (1956).

55. S. Morita E. Meyer, R. W. *Noncontact Atomic Force Microscopy, Volume 1* (Springer, New York, New York, 2002).

56. Martin, Y. & Wickramasinghe, H. K. Magnetic imaging by "force microscopy" with 1000 Å resolution. *Applied Physics Letters* **50,** 1455 (1987).

57. Zhou, W., Apkarian, R., Wang, Z. & Joy, D. *Scanning Microscopy for Nanotechnology* (eds Zhou, W. & Wang, Z. L.) 1 (Springer, New York, New York, 2007).

58. Scholl, A., Marcus, M., Doran, A., Nasiatka, J., Young, A., MacDowell, A., Streubel, R., Kent, N. & Feng, J. Hartmann characterization of the PEEM-3 aberration-corrected X-ray photoemission electron microscope. *Ultramicroscopy* **188,** 77 (2018).

59. Kirz, J. Phase zone plates for x rays and the extreme uv. *J. Opt. Soc. Am.* **64(1),** 301 (1974).

60. Fischer, P., Eimüller, T., Schütz, G., Guttmann, P., Schmahl, G., Pruegl, K. & Bayreuther, G. Imaging of magnetic domains by transmission X-ray microscopy. *Journal of Physics D: Applied Physics* **31,** 649 (1999).

61. Velten, S., Streubel, R., Farhan, A., Kent, N., Im, M.-Y., Scholl, A., Dhuey, S., Behncke, C., Meier, G. & Fischer, P. Vortex circulation patterns in planar microdisk arrays. *Applied Physics Letters* **110,** 262406 (2017).

62. Streubel, R., Kent, N., Dhuey, S., Scholl, A., Kevan, S. & Fischer, P. Spatial and Temporal Correlations of XY Macro Spins. *Nano Letters* **18,** 7428 (2018).

63. Liu, X., Kent, N., Ceballos, A., Streubel, R., Jiang, Y., Chai, Y., Kim, P. Y., Forth, J., Hellman, F., Shi, S., Wang, D., Helms, B. A., Ashby, P. D., Fischer, P. & Russell, T. P. Reconfigurable ferromagnetic liquid droplets. *Science* **365,** 264 (2019).

64. Montoya, S. A., Couture, S., Chess, J. J., Lee, J. C. T., Kent, N., Henze, D., Sinha, S. K., Im, M.-Y., Kevan, S. D., Fischer, P., McMorran, B. J., Lomakin, V., Roy, S. & Fullerton, E. E. Tailoring magnetic energies to form dipole skyrmions and skyrmion lattices. *Phys. Rev. B* **95,** 024415 (2017).

65. Streubel, R., Lambert, C.-H., Kent, N., Ercius, P., N'Diaye, A. T., Ophus, C., Salahuddin, S. & Fischer, P. Experimental Evidence of Chiral Ferrimagnetism in Amorphous GdCo Films. *Advanced Materials* **30,** 1800199 (2018).

66. Kent, N., Streubel, R., Lambert, C.-H., Ceballos, A., Je, S.-G., Dhuey, S., Im, M.-Y., Büttner, F., Hellman, F., Salahuddin, S. & Fischer, P. Generation and stability of structurally imprinted target skyrmions in magnetic multilayers. *Applied Physics Letters* **115,** 112404 (2019).

67. Kruglyak, V. & Kuchko, A. Spectrum of spin waves propagating in a periodic magnetic structure. *Phys. Rev, B* **339,** 103 (2003).

68. Puszkarski, H. & Krawczyk, M. Interfacial Effects and Novel Properties of Nanomaterials. *Solid State Phenomena* **94,** 125 (2003).

69. Waeyenberge, B. V., Puzic, A., Stoll, H., Chou, K. W., Tyliszczak, T., Hertel, R., Fähnle, M., Brückl, H., Rott, K., Reiss, G., Neudecker, I., Weiss, D., Back, C. H. & Schütz, G. Magnetic vortex core reversal by excitation with short bursts of an alternating field. *Nature* **444,** 461 (2006).

70. Fert, 5., Cros, V. & Sampaio, J. Skyrmions on the track. *Nature Nanotechnology* **8,** 152 (2013).

71. Wiesendanger, R. Nanoscale magnetic skyrmions in metallic films and multilayers: a new twist for spintronics. *Nature Reviews Materials* **1,** 16044 (2016).

72. Soumyanarayanan, A., Reyren, N. & Fert, A. Emergent phenomena induced by spin–orbit coupling at surfaces and interfaces. *Nature* **1,** 509 (2016).

73. Adolff, C., Hanze, M., Vogel, A., Weigand, M., Martens, M. & Meier, G. Self-organized state formation in magnonic vortex crystals. *Phys. Rev. B.* **88,** 224425 (2013).

74. Jain, S., Novosad, V., Fradin, F., Pearson, J., Tiberkevich, V., Slavin, A. & Bader, S. From chaos to selective ordering of vortex cores in interacting mesomagnets. *Nature Comm.* **3,** 1330 (2012).

75. Jain, S., Ren, Y., Adeyeye, A. O. & Singh, N. Configurational anisotropy and control of magnetic vortex chirality in arrays of circular Ni80Fe20 nanoscale dots. *Phys. Rev. B.* **80,** 132401 (2009).

76. Streubel, R., Kronast, F., Rossler, U., Schmidt, O. & Makarov, D. Reconfigurable large-area magnetic vortex circulation patterns. *Phys. Rev. B.* **92,** 104431 (2015).

77. Zimmerman, G., Ibrahim, A. & Wu, F. Planar classical dipolar system on a honeycomb lattice. *Phys. Rev. B* **37,** 2059 (1988).

78. Baek, S. K., Minnhagen, P. & Kim, B. Kosterlitz-Thouless transition of magnetic dipoles on the two-dimensional plane. *Phys. Rev. B.* **83,** 184409 (2011).

79. Prakash, S. & Henley, C. Ordering due to disorder in dipolar magnets on two-dimensional lattices. *Phys. Rev. B.* **42,** 6574 (1990).

80. Schildknecht, D., Heyderman, L. J. & Derlet, P. M. Phase diagram of dipolar-coupled XY moments on disordered square lattices. *Phys. Rev. B.* **98,** 064420 (2018).

81. Kosterlitz, J. M. & Thouless, D. Ordering, metastability and phase transitions in two-dimensional systems. *J. Phys. C: Solid State Phys.* **6,** 1187 (1973).

82. Berenzinskii, B. Destruction of long-range order in onedimensional and two-dimensional systems possessing a continuous symmetry group. II. Quantum systems. *Sov. Phys. JETP* **34,** 610 (1972).

83. Leo, N., Holenstein, S., Schildknecht, D., Sendetskyi, O., Luetkens, H., Derlet, P., Scagnoli, V., Lançon, D., Mardegan, J., Prokscha, T., Suter, A., Salman, Z., Lee, S. & Heyderman, L. Collective magnetism in an artificial 2D XY spin system. *Nat. Commun.* **9,** 2850 (2018).

84. Arnalds, U. B., Ahlberg, M., Brewer, M. S., Kapaklis, V., Papaioannou, E., Karimipour, M., Korelis, P., Stein, A., Ólafsson, S., Hase, T. P. A. & Hjörvarsson, B. Thermal transitions in nanopatterned XY-magnets. *Appl. Phys. Lett.* **105,** 042409 (2014).

85. Ewerlin, M., Demirbas, D., Brüssing, F., Petracic, O., Ünal, A. A., Valencia, S., Kronast, F. & Zabel, H. Magnetic Dipole and Higher Pole Interaction on a Square Lattice. *Phys. Rev. Lett* **110,** 177209 (2013).

86. Vedmedenko, E. Y., Mikuszeit, N., Oepen, H. P. & Wiesendanger, R. Multipolar Ordering and Magnetization Reversal in Two-Dimensional Nanomagnet Arrays. *Phys. Rev. Lett* **95,** 207202 (2005).

87. Morgan, J., Stein, A., Langridge, S. & Marrows, C. Thermal ground-state ordering and elementary excitations in artificial magnetic square ice. *Nat. Phys.* **7,** 75 (2011).

88. Farhan, A., Saccone, M., Petersen, C. F., Dhuey, S., Chopdekar, R. V., Huang, Y.-L., Kent, N., Chen, Z., Alava, M. J., Lippert, T., Scholl, A. & van Dijken, S. Real-space observation of emergent magnetic monopoles and associated Dirac strings in artificial kagome spin ice. *Nat. Phys.* **7,** 75 (2011).

89. Zhou, D., Wang, F., Li, B., Lou, X. & Han, Y. Glassy Spin Dynamics in Geometrically Frustrated Buckled Colloidal Crystals. *Phys. Rev. X* **7,** 021030 (2017).

90. De'Bell, K., MacIsaac, A., Booth, I. & Whitehead, J. Dipolar-induced planar anisotropy in ultrathin magnetic films. *Phys. Rev. B.* **55,** 15108 (1997).

91. Odenbach, S. Ferrofluids and their applications. *MRS Bull.* **38,** 921 (2013).

92. Rosenzweig, R. *Magnetic Fluids* (Courier Corporation, 2013).

93. Wang, W., Timonen, J., Carlson, A., Drotlef, D.-M., Zhang, C., Kolle, S., Grinthal, A., Wong, T. S., Hatton, B., Kang, S., Kennedy, S., Chi, J., Blough, R., Sitti, M., Mahadevan, L. & Aizenberg, J. Multifunctional ferrofluid-infused surfaces with reconfigurable multiscale topography. *Nature* **559,** 78 (2018).

94. Meng, L., Kim, H.-H., Kim, H., Muhammed, M. & Kim, D. K. Iron oxide-based nanomagnets in nanomedicine:fabrication and applications. *Nano. Rev.* **1,** 4833 (2010).

95. Leggett, A. Superfluid 3He A is a liquid ferromagnet. *Nature.* **270,** 585 (1977).

96. Luo, W., Nagel, S. R., Rosenbaum, T. F. & Rosensweig, R. E. Dipole interactions with random anisotropy in a frozen ferrofluid. *Phys. Rev. Lett.* **67,** 144 (1991).

97. Goya, G. F., Berquó, T. S., Fonseca, F. C. & Morales, M. P. Static and dynamic magnetic properties of spherical magnetite nanoparticles. *Journal of Applied Physics* **94,** 3520 (2003).

98. Iida, H., Takayanagi, K., Nakanishi, T. & Osaka, T. Synthesis of Fe3O4 nanoparticles with various sizes and magnetic properties by controlled hydrolysis. *Journal of Colloid and Interface Science* **314,** 274 (2007).

99. Huang, C., Sun, Z., Cui, M., Liu, F., Helms, B. A. & Russell, T. P. Structured Liquids with pH-Triggered Reconfigurability. *Advanced Materials* **28,** 6612 (2016).

100. Cui, M., Emrick, T. & Russell, T. Stabilizing Liquid Drops in Nonequilibrium Shapes by the Interfacial Jamming of Nanoparticles. *Science* **342,** 460 (2013).

101. Zhang, Z., Jiang, Y., Huang, C., Chai, Y., Goldfine, E., Liu, F., Feng, W., Forth, J., Williams, T. E., Ashby, P. D., Russell, T. P. & Helms, B. A. Guiding kinetic trajectories between jammed and unjammed states in 2D colloidal nanocrystal-polymer assemblies with zwitterionic ligands. *Science Advances* **4** (2018).

102. Stoner, E. & Woohlfarth, E. A Mechanism of Hysteresis in Heterogeneous Alloys. *Philos. Trans. Roy. Soc. London* **A240,** 599 (1947).

103. Puntes, V., Gorostiza, P., Aruguete, D., Bastús, N. & Alivisatos, A. Collective behaviour in two-dimensional cobalt nanoparticle assemblies observed by magnetic force microscopy. *Nat. Mat.* **3,** 263 (2004).

104. Nagaosa, N. & Tokura, Y. Topological properties and dynamics of magnetic skyrmions. *Nat. Nano.* **8,** 899 (2013).

105. Finazzi, M., Savoini, M., Khorsand, A. R., Tsukamoto, A., Itoh, A., Duò, L., Kirilyuk, A., Rasing, T. & Ezawa, M. Laser-Induced Magnetic Nanostructures with Tunable Topological Properties. *Phys. Rev. Lett.* **110,** 177205 (2013).

106. Yu, X. Z., Shibata, K., Koshibae, W., Tokunaga, Y., Kaneko, Y., Nagai, T., Kimoto, K., Taguchi, Y., Nagaosa, N. & Tokura, Y. Thermally activated helicity reversals of skyrmions. *Phys. Rev. B* **93,** 134417 (2016).

107. Yu, X., Mostovoy, M., Tokunaga, Y., Zhang, W., Kimoto, K., Matsui, Y., Kaneko, Y., Nagaosa, N. & Tokura, Y. Magnetic stripes and skyrmions with helicity reversals. *Proc. Natl Acad. Sci. USA* **109,** 8856 (2012).

108. Miguel, J., Peters, J., Toulemonde, O., Dhesi, S., Brookes, N. & Goedkoop, J. X-ray resonant magnetic scattering study of magnetic stripe domains in a-GdFe thin films. *Phys. Rev. B* **74,** 094437 (2012).

109. Craik, D. & Cooper, P. Criteria for uniaxial magnetostatic behaviour in thin platelets. *Phys. Lett. A* **41,** 255 (1972).

110. Stavrou, E. & Roll, E. Magnetic anisotropy in Gd/(FeCo) and Gd/Fe multilayers for high density magneto-optical recording. *J. Appl. Phys.* **49,** 5971 (1999).

111. Stavrou, E., Sbiaa, R., Suzuki, T., Knappmann, S. & Roll, K. Magnetic anisotropy and spin reorientation effects in Gd/Fe and Gd/(FeCo) multilayers for high density magneto-optical recording. *J. Appl. Phys.* **87,** 6899 (2000).

112. Muller, M. Domain Formation in a Ferromagnetic Plate. *J. Appl. Phys.* **38,** 2413 (1967).

113. M.Hehn, Padovani, S., Ounadjela, K. & Bucher, J. P. Nanoscale magnetic domain structures in epitaxial cobalt films. *Phys. Rev. B.*. **54,** 3428 (1996).

114. Donnet, D., Krishnan, K. & Yajima, Y. Domain structures in epitaxially grown cobalt thin films. *Phys. Rev. B.*. **28,** 1942 (1996).

115. Saito, N., Fujiwara, H. & Sugita, Y. A New Type of Magnetic Domain Structure in Negative Magnetostriction Ni-Fe Films. *J. Phys. Soc. Jpn* **19,** 1116 (1964).

116. Shanavas, K. V., Popović, Z. S. & Satpathy, S. Theoretical model for Rashba spin-orbit interaction in d electrons. *Phys. Rev. B.* **90,** 165108 (2014).

117. Porter, N., Gartside, J. & Marrows, C. Near room-temperature formation of a skyrmion crystal in thin-films of the helimagnet FeGe. *Nature Materials* **10,** 106 (2011).

118. Yang, H., Thiaville, A., Rohart, S., Fert, A. & Chshiev, M. Anatomy of Dzyaloshinskii-Moriya Interaction at Co/Pt Interfaces. *Phys. Rev. Lett.* **115,** 267210 (2015).

119. Soumyanarayanan, A., Masapogu, R., Oyarce, A., K.C. Tan, A., Im, M.-Y., Petrović, A., Ho, P., Khoo, K. H., Tran, M., Gan, C., Ernult, F. & Panagopoulos, C. Tunable room-temperature magnetic skyrmions in Ir/Fe/Co/Pt multilayers. *Nature Materials* **16,** 898 (2017).

120. Schütz, G., Goering, E. & Stoll, H. in *Handbook of Magnetism and Advanced Magnetic Materials* (eds Kronmüller, H. & Parkin, S.) (Wiley-Interscience, 2007).

121. Gilbert, D. A., Maranville, B. B., Balk, A. L., Kirby, B. J., Fischer, P., Pierce, D. T., Unguris, J., Borchers, J. A. & Liu, K. Realization of ground-state artificial skyrmion lattices at room temperature. *Nat. Comm.* **6,** 8462 (2015).

122. Sun, Z., Schnabel, A., Burghoff, M. & Li, L. Calculation of an optimized design of magnetic shields with integrated demagnetization coils. *AIP Advances* **6,** 075220 (2016).

123. Lemesh, I., Buttner, F. & Beach, G. S. D. Accurate model of the stripe domain phase of perpendicularly magnetized multilayers. *Phys. Rev. B* **95,** 174423 (2017).

124. Buttner, F., Lemesh, I. & Beach, G. Theory of isolated magnetic skyrmions: From fundamentals to room temperature applications. *Sci. Reports* **8,** 4464 (2018).

125. Zhang, S., Kronast, F., van der Laan, G. & Hesjedal, T. Real-Space Observation of Skyrmionium in a Ferromagnet-Magnetic Topological Insulator Heterostructure. *Nano Letters* **18,** 1057 (2018).

126. Fowlkes, J. D., Winkler, R., Lewis, B. B., Fernández-Pacheco, A., Skoric, L., Sanz-Hernández, D., Stanford, M. G., Mutunga, E., Rack, P. D. & Plank, H. High-Fidelity 3D-Nanoprinting via Focused Electron Beams: Computer-Aided Design (3BID). *ACS Applied Nano Materials* **1,** 1028 (2018).

127. May, A., Hunt, M., Berg, A., Hejazi, A. & Ladak, S. Realisation of a Frustrated 3D Magnetic Nanowire Lattice. *Communication Physics* **2,** 13 (2019).

128. Donnelly, C., Finizio, S., Gliga, S., Holler, M., Hrabec, A., Odstrcil, M., Mayr, S., Scagnoli, V., Heyderman, L., Guizar-Sicairos, M. & Raabe, J. Time-resolved imaging of three-dimensional nanoscale magnetization dynamics. *Nature Nanotechnology* **15,** 356 (2020).

129. Liu, Y., Hou, W., Han, X. & Zang, J. Three-Dimensional Dynamics of a Magnetic Hopfion Driven by Spin Transfer Torque. *Phys. Rev. Lett.* **124,** 127204 (2020).

130. Bourianoff, G., Pinna, D., Sitte, M. & Everschor-Sitte, K. Potential implementation of reservoir computing models based on magnetic skyrmions. *AIP Advances* **8,** 055602 (2018).

131. Wang, X. S., Qaiumzadeh, A. & Brataas, A. Current-Driven Dynamics of Magnetic Hopfions. *Phys. Rev. Lett.* **123,** 147203 (2019).